Fluoroscopy Based Needle-Positioning System for Percutaneous Nephrolithotomy Procedures

by

Jean-Pierre Conradie

Thesis presented at the University of Stellenbosch in partial fulfillment of the requirements for the degree of

Master of Science in Mechatronic Engineering

Department of Mechanical & Mechatronic Engineering
Stellenbosch University

Project Supervisors:

Prof. Cornie Scheffer

Dr. Kristiaan Schreve

December 2008

Declaration

By submitting this thesis electronically, I declare that the entirety of the work contained therein is my own, original work, that I am the owner of the copyright thereof (unless to the extent explicitly otherwise stated) and that I have not previously in its entirety or in part submitted it for obtaining any qualification.

Date: December 2008

ABSTRACT

Fluoroscopy Based Needle-Positioning System for Percutaneous Nephrolithotomy Procedures

J-P Conradie
Department of Mechanical & Mechatronic Engineering
Stellenbosch University
Private Bag X1, 7602 Matieland, South Africa
Thesis: MScEng (Mech)
December 2008

A fluoroscopy-guided needle-positioning system is designed and tested as a first prototype for aiding urologists in gaining fast, accurate and repeatable kidney calyx access during a PCNL procedure while also reducing radiation exposure of the people involved. Image guidance is realized by modelling the fluoroscopic system as an adapted pinhole camera model and utilizing stereo vision principles on a stereo image pair. Calibration, distortion correction and image processing algorithms are implemented on images of a designed calibration object. Thereafter the resulting variables are used in the targeting of the calyx with the aid of a graphical user interface. The required relative translation and rotation of the needle from its current position to the target is calculated and the system is adjusted accordingly. Using digital cameras, needle placement accuracies of 2.5 mm is achieved within the calibrated volume in a simulated environment. Similar results are achieved in the surgery room environment using the fluoroscopic system. Successful needle access in two porcine kidney calyxes concluded the testing.

UITTREKSEL

Fluoroskopie-Gebaseerde Naald-Posisioneringstelsel vir Perkutane Nefrolitotomie Prosedures

J-P Conradie
Departement Meganiese & Megatroniese Ingenieurswese
Universiteit van Stellenbosch
Privaatsak X1, 7602 Matieland, Suid-Afrika
Tesis:MScIng (Meg)
Desember 2008

‘n Naald-posisioneringstelsel is ontwerp en getoets as ‘n eerste prototipe vir gebruik deur ‘n uroloog tydens ‘n PKNL-prosedure om vinnige, akkurate en herhaalbare nierkelk toegang moontlik te maak. Die stelsel verminder radiasieblootstelling van die personeel en patiënt. Beeldnavigasie is bewerkstellig deur ‘n fluoroskopie sisteem te modelleer as ‘n aangepasde “pinhole”-kameramodel en gebruik te maak van stereovisie beginsels op ‘n stereobeeld paar. Kalibrasie, distorsiekorreksie en beeldprosesseringsfunksies is toegepas op beelde van ‘n kalibrasievoorwerp waarna ‘n gebruikersintervlak geïmplimenteer is om die nierkelk te teiken. Die nodige verplasing en rotasie van die naald vanaf sy beginposisie na sy teikenposisie is bepaal en daarvolgens verstel. Met die gebruik van digitale kameras is ‘n naaldposisioneringsakkuraatheid van 2.5 mm behaal binne die gekalibreerde volume in ‘n gesimuleerde omgewing. Soortgelyke resultate is verkry in die teater met die gebruik van die fluoroskopie stelsel. Suksesvolle naaldtoegang in twee varknierkelke het die toetse afgesluit.

DEDICATIONS

To Marlize

ACKNOWLEDGEMENTS

The author would like to thank the following people for their contribution towards this project:

- Dr. Kristiaan Schreve, my co-supervisor, for his guidance and help throughout the project.
- Prof. Cornie Scheffer, my supervisor, for his steady hand, calm nature and wisdom without which I would have not reached this point.
- Dr. Amir Zarrabi of Tygerberg Hospital's Nephrology Department for all his inputs and guidance.
- Prof. Ben Herbst and Dr. Karin Hunter of the Applied Mathematics Department for their ideas and assistance in understanding basic principles of computer vision.
- Ferdie Zietsman, Cobus Zietsman and Anton van den Berg of the Mechanical & Mechatronic Departments Workshop for the manufacturing of the project parts.
- Malcolm April, Elsabe du Toit and Dr. Groenewald from the Radiation Oncology Unit (X-block) at Tygerberg Hospital for their assistance and the use of the BV Pulsera system.
- Willie van der Merwe for all his input and help with the setup of the *Python* programming environment.

CONTENTS

LIST OF FIGURES

LIST OF TABLES

GLOSSARY & NOMENCLATURE

Asymptomatic - having no symptoms of illness or disease

Idiopathic – arising from an unknown cause

Nephrolithotomy – surgical removal of a stone from the kidney

Percutaneous – through the unbroken skin

CCD - charge coupled device

CCAP - calyx-center-to-access-point-vector

CMM - coordinate measuring machine

CT - computed tomography

CV - calyx-vector

DLT - direct linear transform method

ESWL - extracorporeal shock wave lithotripsy

FI - fluoroscopic imaging

GCS - gantry coordinate system

GUI - graphical user interface

II - image intensifier

MRI - magnetic resonance imaging

NV - needle-vector

PAKY - percutaneous access to the kidney

PCNL - percutaneous nephrolithotomy

PKNL – perkutane nefrolitotomie

SVD - singular value decomposition

TRUS - transrectal ultrasonography

US - ultrasound

WCS - world coordinate system

XRT - x-ray tank

CHAPTER 1

1. INTRODUCTION

In this chapter, percutaneous nephrolithotomy and the current problem regarding needle access, is stated. Thereafter the project objectives and motivation are discussed.

1.1 Background

Percutaneous nephrolithotomy (PCNL), a kidney stone removal technique, is performed in clinical institutions under fluoroscopic guidance and is widely seen as the best technique for treating large, staghorn and other complex renal stones. The technique is based on gaining kidney access using a needle through which a guidewire is inserted and anchored inside the kidney structure. The tract is then dilated creating a passage through which the stone removal equipment can reach the stone. Current strategies used in PCNL to gain access to a predefined kidney calyx often result in renal tissue damage and hemorrhage due to multiple unsuccessful needle insertion attempts. Current systems developed for the improvement of this problem are based on expensive imaging systems or other surgical tool navigation equipment.

1.2 Objectives

It is the main objective of this project to develop a system capable of aiding a surgeon during the access step of a PCNL procedure to accurately place an access needle inside a predefined calyx. As kidney calyx size is typically larger than 10 mm in diameter, a system with a needle placement accuracy of 3 mm or better is deemed adequate. The system must be an affordable alternative to other systems and must use standard fluoroscopic imaging equipment readily available in the surgery room.

The success of implementing stereo vision theory on stereo images obtained by the fluoroscopic system was investigated and the accuracy was compared to normal stereo vision applications. An attempt was made at designing a system capable of accurately moving and orientating a needle for precision needle insertion. Compensation of needle deflection and kidney movement during insertion was not part of the project goals.

1.3 Motivation

There is currently no cost-effective technique available in the clinical environment that guarantees accurate needle placement inside a predefined kidney calyx. Insertion strategies commonly used in combination with a fluoroscopic

imaging system such as “Triangulation” and “Keyhole Surgery” are mainly dependent on the experience of the surgeon. With each failed needle insertion attempt, the renal capsule, interlobular arteries and veins, as well as other internal kidney structures, are damaged. This can result in excessive hemorrhage, forcing the surgeon to abort the entire procedure due to the risk for the patient. Radiation exposure of the patient and surgery team is increased with increased fluoroscopy system use. In some cases, continuous fluoroscopic imaging is used, resulting in high radiation doses to all involved. Access problems increase theatre time as well as patient expenses, and decrease surgery staff availability. The need for a cost effective and time efficient system aiding the surgeon in accurate targeting of a specified calyx at the first attempt is apparent. This project proposes a possible solution to this problem by using a fluoroscopy system and image guided needle-positioning system for accurate positioning.

1.4 Thesis Overview

Chapter 2 presents background on kidney stones and the current treatment techniques. Relevant needle-positioning systems developed during the last decade are discussed. Chapter 3 discusses the theory implemented to mathematically describe cameras and use them for relative positioning. It also depicts the image processing techniques and the reasons for their use in the project. This leads to Chapter 4, which elaborates on the specifications of the needed system and describes the methodology used in the design of all components utilized in the project. This includes the calibration object and needle-positioning system. Chapter 5 covers the mathematical computations implemented to rotate and translate the needle for accurate targeting. Also described are the objects targeted, their configuration and the methods used. Implementation of the described work is shown in Chapter 6. The two testing environments are also described. Visual distortion correction, calibration and triangulation results are presented and illustrated where possible. The user interface and implementation steps are also described. Chapter 7 describes the experiments and reports on the results obtained. The final chapter presents the conclusions and recommendations of the project. The shortcomings of the designed system are also commented on.

CHAPTER 2

2. LITERATURE REVIEW AND RATIONALE

This chapter starts with an introduction to the relevant information regarding kidney stones (renal calculi), the anatomy of the kidney, their internal position, as well as kidney stone location. Relevant background information on current stone removal techniques is given. PCNL, the most important of these techniques with respect to this project, is elaborated on. Other techniques involving the placement and guidance of needles using medical imaging systems are discussed.

2.1 Renal Calculi: A Background

Renal calculi, commonly known as kidney stones, are solid pieces of material that form in the kidney from depositing substances in the urine. Some are as small as a grain of sand whereas others fill the entire renal pelvis reaching sizes of 4 cm to 5 cm in diameter. Kidney stones are often asymptomatic depending on its position and size. The first symptom of a kidney stone is usually extreme pain in the back and side, in the area of the kidney, or in the lower abdomen [1]. Pain may later spread to the groin area. In some cases nausea and vomiting occur with traces of blood in the urine also a common occurrence. Predominantly, these composites are small enough to leave the body through the urinary tract without causing much pain. In bigger calculus cases the passage of urine flow through the ureter, bladder or urethra can be blocked due to a lodged calculus, causing the described symptoms. Examples of kidney stone shapes and sizes are shown in Figure 2-1(a) and (b).

Renal calculi are one of the most common disorders of the urinary tract. Prevalence has increased over the past three decades, possibly due to increased animal and dietary intake. In the United States 5.2% of adults (6.3% male and 4.1% female), aged 20-74, self-reported having renal calculi [2]. The incidence rate in the US in 2002 was over 1 million [3].

Various reasons for the development of renal calculi have been described. Kidney calculi develop as a result of a complicated interaction of biological events that are most likely triggered by genetic susceptibility coupled with dietary factors. The key process in the development of renal calculi is *supersaturation.* This involves the precipitation and crystallization of salts (calcium oxalate, uric acid, cystine, or xanthine) due to very high salt concentrations carried in the urine or major changes in the acidity of the urine. Deficiencies in calculus-forming prohibiting-factors in the urine such as magnesium, citrate, various proteins and enzymes also play a vital role in calculus formation.

(a) Kidney stone shape examples
[www.billybarton.com]

(b) Kidney stone size variation
[www.urinarystones.info]

Figure 2-1: Kidney stone examples

In a similar way a deficiency of factors preventing calculi from binding to the kidney tubules increase the chances of calculus formation. Specific calculus types such as calcium, uric acid, struvite and other calculi such as cystine and xanthine calculi form due to a number of reasons. This can include genetic abnormalities, kidney structure abnormalities, bacterial or nanobacterial infection, certain illnesses such as a blood disease and metabolic abnormalities or combinations of the above. Some calculus cases are *idiopathic* [4].

Humans have been aware of renal calculi for thousands of years, and have attempted to treat them for almost as long. The oldest renal calculus was discovered in Egypt around 1900 and carbon dated to 4900 BC. The earliest written records describing surgical renal calculi removal date to before the time of *Hippocrates* who lived from 460 to 370 BC [5]. Various advances have been made in this field since those early times of medicine. In the subsequent text the relevant anatomy of the kidney and its relative orientation to other organs and obstructing structures inside the body are discussed in order to better understand the techniques used in treating renal calculi.

2.2 Renal Macro-and Microstructure

In a normal human two kidneys are located retroperitoneal on either side of the vertebral column between the last thoracic and third lumbar vertebrae, where they are protected by the lower rib cage [6]. The left kidney is often situated slightly higher than the right kidney. Other organs adjacent to the kidneys are the spleen, colon, pancreas and liver. The upper pole of each kidney is in close vicinity to the diaphragm that divides the ventral body cavity into the thoracic and abdominopelvic cavity. The internal positions of the kidneys are shown in Figure 2-2 which depicts a cutaway anterior representation of the position of the two kidneys, as well as other internal structures.

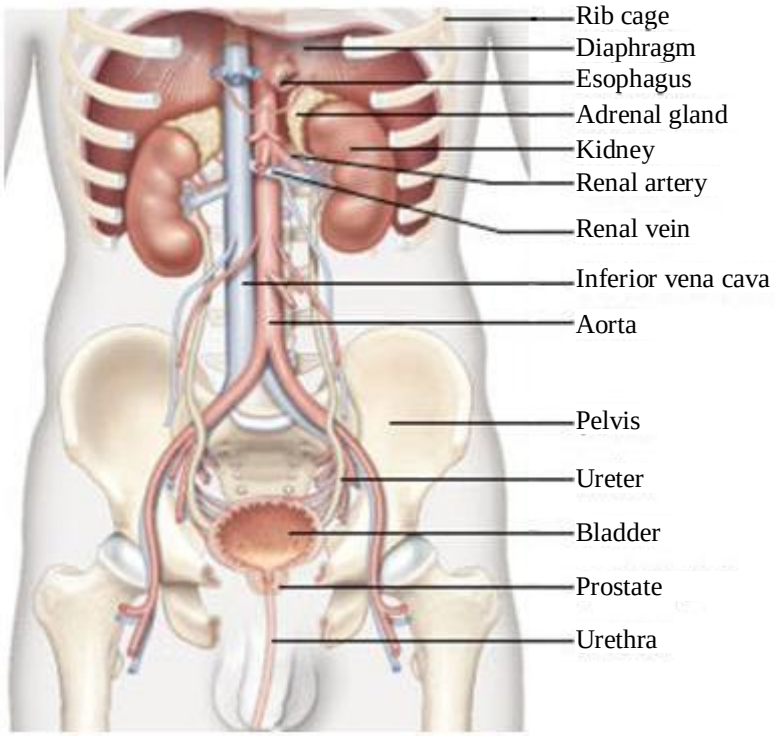

Figure 2-2: Kidney internal position and structures [Encyclopedia Britannica 2003]

The basic kidney structure is shown in Figure 2-3. The point of entry of the renal artery and nerve, as well as the exit for the renal vein and ureter, is seen at the indentation, also known as the hilus. A capsule, known as the renal or fibrous capsule, covers the surface of the kidney and lines the internal cavity, or renal sinus. The kidney is divided into an outer renal cortex and an inner renal medulla. The medulla contains six to eighteen canonical renal pyramids whose tips, or papillae, project into the renal sinus. Renal columns extend from the cortex inward toward the renal sinus between adjacent renal pyramids. The minor calyces, either posterior or anterior in alignment, merge to form the major calyces, which combine to form the renal pelvis. The renal pelvis is connected to the bladder by the ureter.

Kidney stones can form in any of the abovementioned cavities inside the kidney of which the calices are the most common. This is shown in Figure 2-4(a). Figure 2-4(b) depicts an x-ray image of a patient with a staghorn calculus (branched calculus commonly composed of struvite), filling the entire renal pelvis. The insertion of a needle in a specified calyx for safe removal of these stones is the final aim of this project.

2.3 Stone Removal Techniques

The three most commonly utilized stone removal techniques are open surgery, extracorporeal shockwave lithotripsy (ESWL) and PCNL. This section gives a

general overview of open surgery and ESWL and describes the PCNL procedure in detail. Emphasis is placed on the indications for each procedure, the imaging systems used during each routine, and the strategies used to gain kidney access during the PCNL procedure.

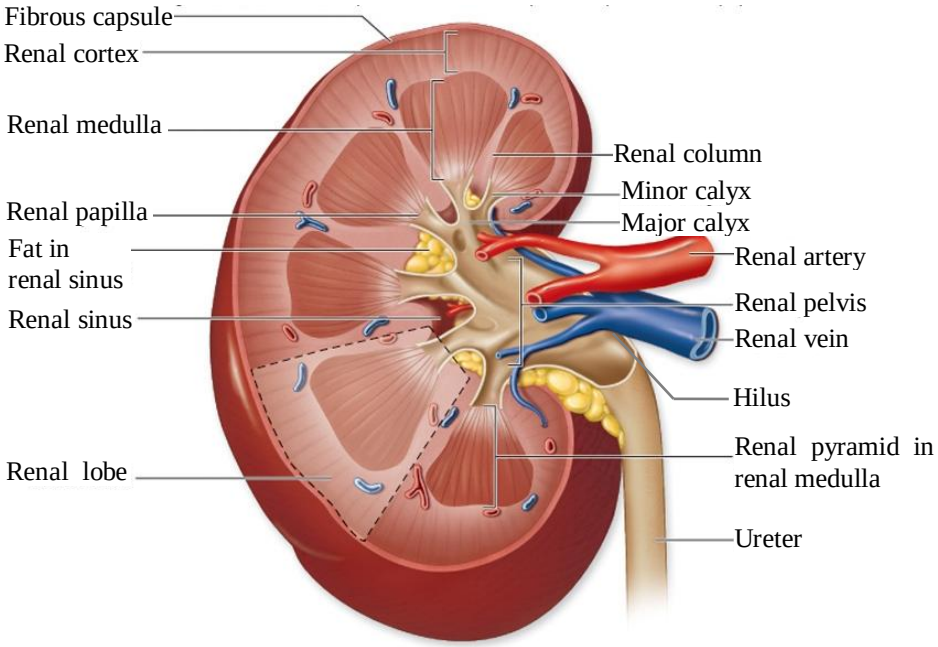

Figure 2-3: Internal kidney structure [www.academic.kellogg.cc.mi.us]

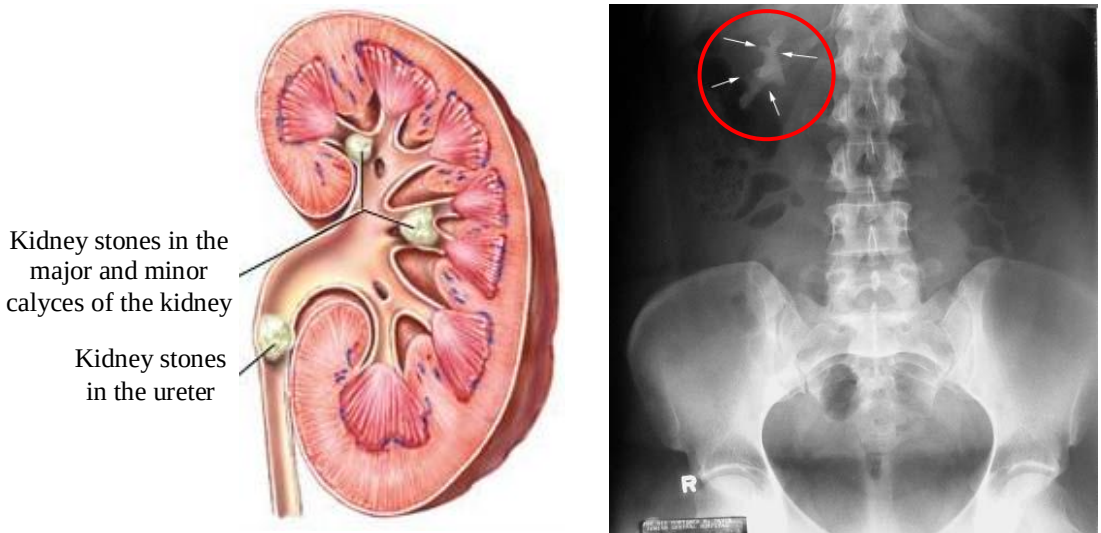

(a) Calyx formation positions [www.nytimes.com]

(b) X-ray of a staghorn calculus

Figure 2-4: Stone positions

2.3.1 Open Surgery

For years open surgical techniques for removal of calculi were used extensively in clinical environments. This changed during the last three decades with the introduction of minimally invasive ESWL and PCNL techniques in the 1980's [7]. With the introduction of the new techniques, the indications for open stone surgery was narrowed significantly, and for the most part open surgery has become a second or third line treatment option performed frequently to treat patients who had failed one or a combination of the newer modalities [8]. It has been determined by Paik and Resnick that a complex stone burden represents the most frequent indication for an open stone procedure [8]. Complex stones are defined as stones that occupy the renal pelvis with extensions into the calyces as well as complete staghorn calculi.

Open surgery is performed by making an incision in the patient's back or abdomen on the side of the vertebrae column where the infected kidney is situated. An incision is made along the long axis of the kidney, thus allowing the kidney to be opened like a book. After all stone fragments are removed, the kidney is sewn back together [9]. This technique is usually accompanied with longer recovery and hospitalization periods compared to the less invasive techniques. Up to two weeks in hospital is common. The imaging modalities used prior or after an open surgery usually consist of fluoroscopic or ultrasound (US) imaging to verify stone-free status.

2.3.2 Extracorporeal Shock Wave Lithotripsy (ESWL)

As mentioned in the previous section, ESWL has replaced open surgery in most institutions. ESWL was developed in the early 1980's. During ESWL the lithotripter attempts to break up the calculus with an externally applied, focused, high-intensity acoustic pulse. A fluoroscopic or US imaging device is used to locate and pinpoint the stone so the pulses are focused on the calculus. The frequency and power level of the pulses are increased as the treatment progresses to accustom the patient to the sensation. The pulses created by the lithotripter result in direct shearing forces fragmenting the stone into smaller pieces. These fragments are small enough to leave the body through the ureter.

Stone size is one of the most important factors that must be considered when deciding on ESWL [10]. It is used extensively for stones smaller than 2 cm in diameter. Contraindications in patients include staghorn or complex stones, larger stones, multiple and struvite stones, lower pole stones and where renal infection is suspected [7]. Morbid obesity can make ESWL practically impossible if the maximum skin-to-stone-distance is exceeded.

Even though this technique is the least invasive of the stone removal techniques, it is not without risks. The shock waves can cause capillary damage and renal parenchymal or subcapsular hemorrhage which can lead to long term consequences such as renal failure and hypertension [11]. Re-infection of the kidney is another risk as the fragments need to leave the body through the urinary tract. ESWL is commonly utilized in combination with PCNL in a technique

called “sandwich therapy” where ESWL is performed in between two PCNL procedures.

2.3.3 Percutaneous Nephrolithotomy (PCNL)

Percutaneous nephrostomy was first introduced by Goodwin *et al.* in 1955. In this procedure a tract leading from the patient’s back to the kidney for the drainage of suppuration and urine was established [12]. It was not until 1976 when the first percutaneous nephrostomy, for the specific purpose of removing a kidney calculus, was performed by Fernstrom and Johansson [13]. Initially PCNL was used for high-risk patients. Advances in surgical technique and technology over the past thirty years have allowed urologists to remove stones percutaneously with increasing efficiency. As the percutaneous route to stone removal is superior to the open approach in terms of morbidity, convalescence, and cost, PCNL has replaced open surgical removal of large or complex calculi at most institutions. In the following sections, the PCNL procedure, imaging modalities used, indications and contraindications for the procedure, needle access locations, complications, and the different access techniques, are described.

2.3.3.1 PCNL Procedure

The general procedural steps during PCNL using a fluoroscopic imaging system, as described by Lingeman *et al.,* are given below [14]. Surgeons deviate from these steps depending on the imaging system and available equipment. A standard PCNL procedure can be divided into two sections: (a) obtainment of kidney access and (b) removal of the calculus.

The patient is first anesthetized and an antibiotic administered. This reduces inflammation and aids in minimizing bleeding during the procedure. This also facilitates optimal visualization as well as reducing the risk of post-surgery septic events [10]. A ureteral catheter is placed after which the patient is positioned on the bed in the prone position. The successful use of the supine position during PCNL has also been described and the use of either position depends on the surgeon [15]. Radiographic contrast medium is injected through the catheter delineating the intra-renal system on the fluoroscopic images. An access site for needle insertion is selected by the surgeon, taking into account calculus position, type, size, kidney location and structure, ease of access by the nephroscope, and other organ and skeletal structure positions. The placement of the needle is shown in Figure 2-5(a).

The selection of the access site will be described in more detail in section 2.3.3.5. Patient respiration is paused in full expiration prior to needle insertion to prevent movement of the kidney and adjacent organs and stop the diaphragm as far away from the puncture site as possible. An 18G or 20G trocar needle is inserted into the target calyx by the surgeon with the aid of a guidance technique. Different guidance techniques will be covered in section 2.3.3.6.

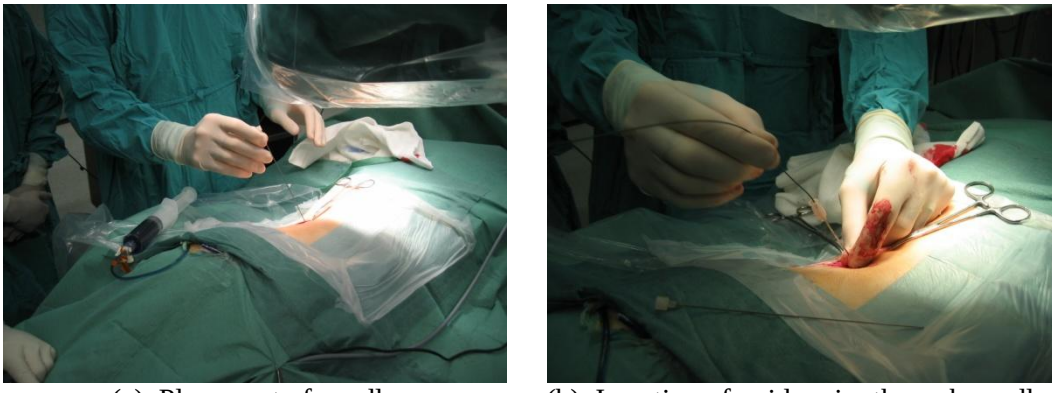

(a) Placement of needle (b) Insertion of guide-wire through needle

Figure 2-5: Needle and guide-wire insertion

A glidewire is inserted down the needle and is preferably navigated down the ureter into the bladder where it is coiled. This is depicted in Figure 2-5(b). If this is not possible the glidewire is coiled in the renal pelvis. A fascial dilator is passed into the calyx, followed by an angiographic catheter helping to direct the wire down the ureter. Once the glidewire is positioned in the ureter, it is replaced by a stiffer working wire. A second wire is placed for safety reasons before tract dilation can commence.

A small incision of 1 cm to 2 cm is made at the access location before a dilator is inserted and the tract is dilated. Alken-, sequential Amplatz- or telescopic dilators can be used. Balloon dilators, seen as the golden standard [7], have shown to cause significantly less bleeding and hemorrhage than sequential dilators. An Amplatz working sheath is advanced over the tract, creating an open low pressure system, thereby decreasing the absorption of irrigant into the circulation. It also improves insertion and removal of the nephroscope and has the ability to basket larger stone fragments. The utilization of the balloon-type dilator and Amplatz working sheath is shown in Figure 2-6(a) and Figure 2-6(b).

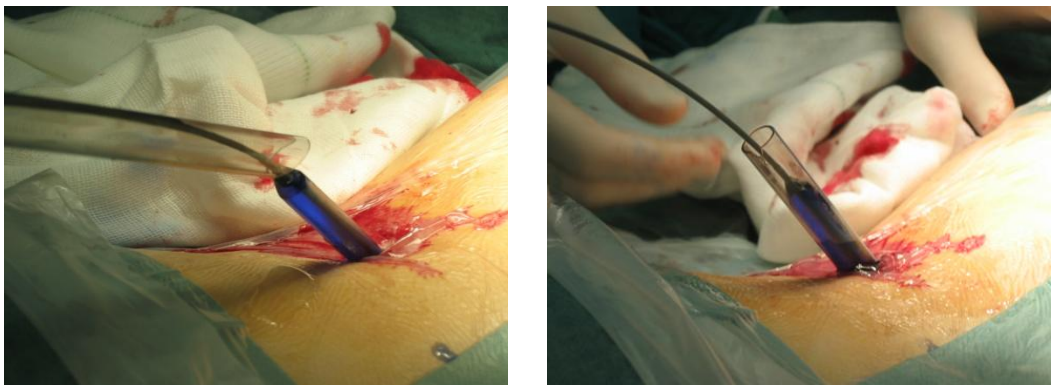

(a) Inserted balloon-type dilator (b) Inserted Amplatz working sheath

Figure 2-6: Creating an access tract

With the working tract constructed, stone removal can be performed under imaging from the nephroscope. Three types of lithotripters are commonly used to

break the stone into smaller fragments; pneumatic, ultrasound or laser. Larger stone fragments are removed using baskets while the smaller fragments are drawn into the suction tube that forms part of the lithotripter. Figure 2-7(a)-(b) depicts the created working tract on a fluoroscopy system screen and the inserted lithotripter respectively.

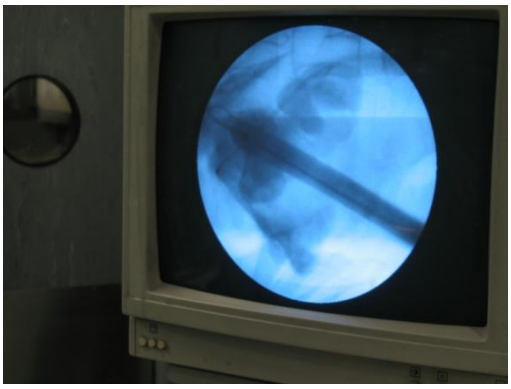

(a) Fluoroscopic image of kidney showing working tract

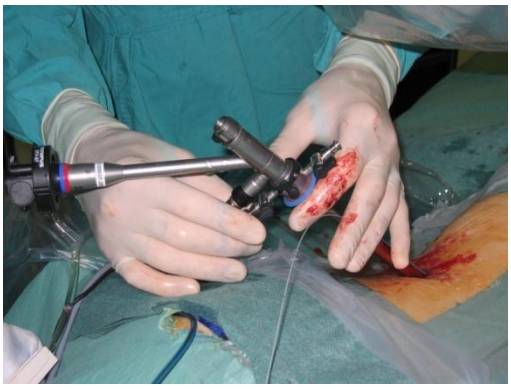

(b) Lithotripter inserted through Amplatz sheath

Figure 2-7: Tool access during PCNL

Attention can now be directed to types of surgical imaging used, the specific techniques used to guide the access needle to the chosen target, indications and contraindications of PCNL, and the issues surrounding access.

2.3.3.2 Imaging

Imaging of the kidney during PCNL is most commonly performed using fluoroscopic imaging. Other imaging modalities include US, magnetic resonance imaging (MRI) and the use of computed tomography (CT) guidance [16]. Initial percutaneous access using fluoroscopic guidance is more challenging than ultrasound because surrounding structures cannot be as easily visualized. Shown in Figure 2-8 is a fluoroscopic view of a contrast-filled kidney imaged during an observed PCNL procedure. Clearly visible in the image is the spinal column, ribs, catheter and some distinguishable parts of the internal kidney structure. Determining the orientation of the calyces from the image is difficult, making precision needle insertion with current techniques impossible.

US give a real-time representation of the kidney, as well as the surrounding structures, making the avoidance of the bowel and solid organs possible during needle insertion. Another advantage is that it is radiation free and usable on expectant mothers. The main disadvantage of US is the limited visualization of intrarenal guidewire manipulation and small stone fragments which may have migrated during PCNL. It is also problematic gaining access to undilated collecting systems using US [17]. MRI has assumed a very limited role in the diagnosis and management of renal calculi because of unreliable identification of stones in the collecting system or ureter [18].

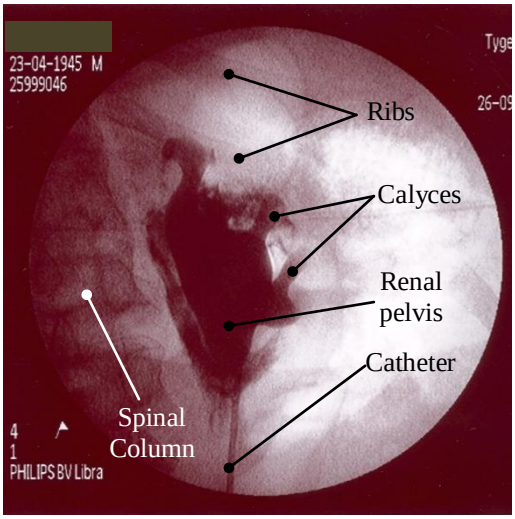

Figure 2-8: Typical view of the kidney during fluoroscopic imaging

CT guidance is often used in special situations, such as patients with splenic enlargement, retrorenal colon or abnormal body morphology such as extreme morbid obesity [16]. The main disadvantages of CT are availability and the high operating cost. Even though fluoroscopy units have the disadvantage of exposing the patient and surgery team to radiation, it is used in most cases due to its availability and functionality.

2.3.3.3 Urologist or Radiologist

Access to the infected kidney is obtained in a one or two-stage procedure. The two-stage option consists of two separate procedures usually performed by two separate individuals; (a) kidney access is obtained by an interventional radiologist prior to the stone removal procedure after which (b) stone removal is performed by an urologist or endourologist through the access tract obtained by the radiologist. During the one-stage procedure access to the kidney and stone removal is performed in one procedure by the urologist. Multiple papers have been published on the debate whether radiologists are still needed for gaining kidney access [19, 20, 21].

Despite the fact that all studies showed that urologist-access compared favorably to that of radiologist obtained access, only 27 % of urologists trained in percutaneous access [14] and 11% of urologists performing PCNL, attained their own access during PCNL [20]. Better equipment and skills of radiologists, as well as the fact that access takes extra time during PCNL, were cited as the main reasons for urologists not performing the procedure themselves. Performing a single stage procedure has the advantages that the procedure success is no longer dependant on another physician, multiple tracts can be inserted during the procedure when and if the need arises, and procedural time and theatre cost is reduced.

2.3.3.4 Indications and Contraindications

The most important indications for a PCNL procedure, as identified by Ramakumar, are stone size and composition, the position of the stone inside the kidney, the existence of obstructions distal to the stone site, the certainty for the final result, the failure or contraindication of ESWL, and the presence of renal anatomic variation [22]. Very large stones, defined as stones greater than 2 cm, complex stones and partial or complete staghorn stones, are usually removed using PCNL. Due to the infectious composition of struvite stones, ESWL is contraindicated for its removal. PCNL is utilized as all stone fragments are mechanically removed from the kidney and does not rely on natural processes for fragment removal. Lower calyceal stones are easily treated with PCNL. In the case of retrocolon (where the colon is situated behind the kidney) PCNL is a high risk procedure due to the risk of rupturing the colon. Certain patient groups such as children, morbidly obese patients, and patients with previous renal surgery, solitary kidney or a history of renal failures, require specific consideration before PCNL is performed. PCNL provides a relatively safe way to provide very high stone free-rates for the situations described.

2.3.3.5 Access Location and Complications

Once indications for a PCNL procedure have been verified, a puncture or needle access site need to be identified by the surgeon, taking into account the abovementioned characteristics. This step is crucial for the success of the procedure.

A posterior calyx is the preferred site of entry as access through a posterior calyx traverses the avascular field (known as the bloodless line of Brödel) due to the orientation of the kidney. A subcostal approach, which is a needle insertion into the calyx from below the 12^{th} rib, is implemented in the majority of cases as chances of splenic, pleural or hepatic injury, is reduced. In the case of staghorn, complex renal and proximal ureteral calculi, a supracostal approach is normally adopted. Access above the 11^{th} rib is associated with much higher intrathoracic complications and is usually avoided if possible [7]. A supracostal approach is usually warranted with an upper pole stone burden.

Depending on supra-, inter- or subcostal access, needle alignment extents in the medial and lateral directions change. A puncture too close to the rib may injure intercostal nerves and vessels resulting in post-operative pain. A more medial access point is usually uncomfortable to the patient and often results in excessive bleeding due to the renal parenchyma being traversed too medially. A too lateral puncture on the other hand, may rupture the colon [23]. No fixed system or standard exists for determining the best access site and site selection depends solely on the surgeon’s judgment and experience.

The most common complication during a PCNL procedure is excessive hemorrhage and renal damage. Blood loss requiring transfusion during the PCNL procedure is one of the major complications and necessitates blood transfusion. Transfusions were necessary in 10.2% of patients in a large study by Muslumanoglu *et al.* [24]. Bleeding was mainly caused by multiple unsuccessful

needle punctures and manipulation of rigid instruments inside the kidney during the procedure. The reason for multiple needle punctures is the lack of accuracy obtained by the current needle guidance techniques. Hemorrhage caused by the instruments is amplified when sub-optimal access into the collecting system is obtained. Current access procedures can take between 10 and 40 minutes with an average length of approximately 20 minutes [25, 26].

The two basic guidance techniques utilizing a fluoroscope are explained after which the related work, as well as current progress in the field of needle guidance, is covered in section 2.4.

2.3.3.6 Current Access Techniques

Kidney access is commonly obtained using retrograde (from inside the body outwards) or one of two antegrade (from outside the body inwards) bi-planar fluoroscopy needle guidance techniques. The two antegrade techniques are known as “triangulation” and “keyhole” respectively. Retrograde access involves the placement of a ureteral catheter followed by the passage of a sharp wire through the catheter out of the desired calyx and out of the body, thus supplying a direct path into the kidney. Retrograde access offers no advantage over antegrade access, which enables more accurate and controlled creation of the tract [14]. The two antegrade techniques consist of several specific steps involving the fluoroscopy system being rotated to different positions relative to the needle and target. These two techniques are explained in order to better understand the uncertainty with which the surgeon currently inserts the access needle.

(1**) Keyhole**

First, a ureteral catheter is placed and the patient is positioned in the prone position. The C-arm fluoroscopy system (section 4.3) is positioned at 30° and the access needle is positioned so the targeted calyx, needle tip and needle hub are in line with the image intensifier, giving a bull’s-eye effect on the monitor. What the surgeon sees on the monitor is a view down the needle into the targeted calyx. Keeping this trajectory, the needle is advanced while continuous fluoroscopic monitoring is performed to ensure that the needle maintains the proper alignment. This is illustrated in Figure 2-9(a)-(b).

Needle depth is obtained by rotating the fluoroscopic system to a vertical orientation relative to the needle. When the needle is aligned with the targeted calyx, the urologist or radiologist should be able to aspirate urine from the collecting system, confirming proper needle positioning.

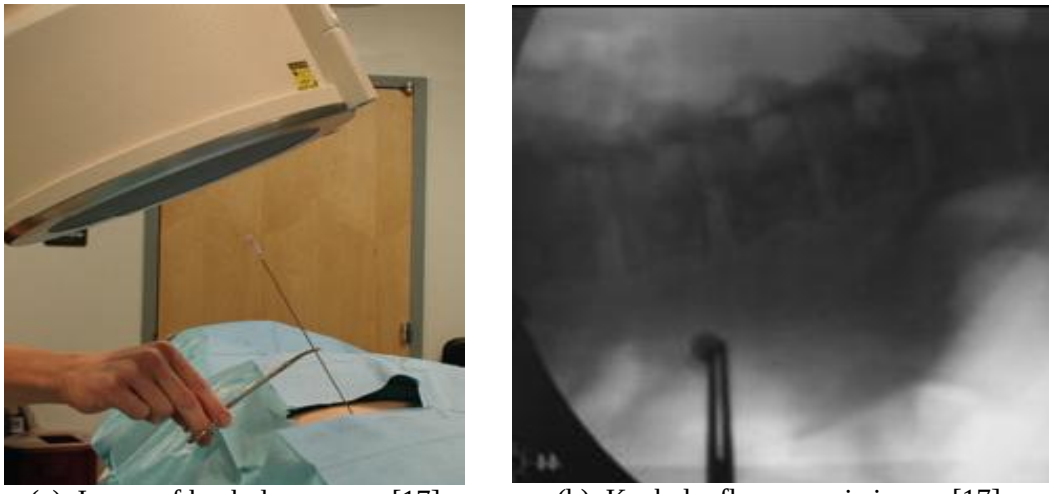

(a) Image of keyhole surgery [17] (b) Keyhole fluoroscopic image [17]

Figure 2-9: Keyhole surgery

(2) Triangulation

The preferred point of entry into the collecting system is along the axis of the calyx, through the papilla. This reduces the force experienced inside the kidney due to rigid instruments such as a nephroscope during navigation to the infected area, reducing renal trauma and bleeding. Unlike the "keyhole" technique, "triangulation" allows for needle alignment down the axis of the calyx.

After the targeted calyx is identified, orientation of the line of puncture is performed using a triangulation technique which is implemented in the following manner: the C-arm is moved back and forth between two positions. One position is parallel and one position is oblique to the line of puncture. With the C-arm oriented parallel to the line of puncture, needle adjustments are made in the mediolateral direction. The C-arm is rotated to the oblique position and needle adjustments are made in the cranio/caudal orientation while keeping the mediolateral orientation of the needle unchanged. After the proper orientation of the line of puncture is obtained, the needle is advanced toward the desired calyx with the C-arm in the oblique position to gauge the depth of puncture.

Conclusion

Despite the fact that the details of these techniques are meticulously described, gaining "correct access", defined as a pre-identified area of a pre-identified calyx, is usually the most difficult part of PCNL. It often results in multiple needle punctures and repeated radiological screening [25]. The end-result is not always "correct access" and urologists often end up accepting sub-optimal positions of access, as this is all that can be obtained. The implications of this are increased duration of the procedure, increased radiation exposure to the patient and surgery team, and decreased stone-free rates. Various researchers have developed techniques and devices attempting to overcome these problems.

2.4 Robotic Surgery & Needle Guidance

Several methods and techniques are found in the literature describing the positioning of an object during a medical procedure. CT, US, MRI or fluoroscopic imaging (FI) is used to plan and predict possible needle insertion paths. Some of these techniques, such as CT and MRI, are overly expensive and can only be implemented in highly equipped facilities. Techniques also exist that are used for keeping the object at the correct position and alignment during insertion. Rigid aligning and laser guided methods are the most common.

Initial applications of robots in urologic surgery have demonstrated their potential in aiding surgeons. The chief advantages of robotic manipulation of surgical tools as described by Stoianovici *et al.* are accurate registration of medical images, consistent movement free of fatigue or tremor, the ability to work in environments unfriendly to surgeons, and the ability to position instruments quickly and accurately [27]. Surgical robots can be divided into two categories: *surgeon driven systems* and *image-guided systems*. Surgeon driven systems rely directly on the surgeon's movement and simulate that movement by robotic means. Image-guided systems use a target specified by the surgeon to manipulate instruments in such a way as to reach the specified target. As the system developed in this project fall in the latter category, the focus will be on current image-guided systems applied in urology.

In 1994 Potamianos *et al.* investigated a robotic system to assist the urologist in obtaining intraoperative percutaneous renal access. The system utilized a passive manipulator mounted on the operating table, guided by a C-arm fluoroscopic unit. Registration between the manipulator and C-arm coordinate systems was completed by a personal computer that also displayed the access needle's trajectory on each fluoroscopic image. The surgeon could then manipulate the robotic arm until the needle's anticipated trajectory aligned with the target calyx. Experiments evaluated system performance with a targeting accuracy of less than 1.5 mm. In-vitro and in-vivo tests were not performed [28, 29]. The system developed by Bzostek *et al.* differed mainly from Potamianos' design in that it used an active robot to manipulate the needle and used bi-planar instead of C-arm fluoroscopy. This system achieved in-vitro accuracy results of 0.5 mm. Ex-vivo tests on porcine kidneys resulted in an 83% insertion success rate. In-vivo tests on cadaveric porcine and live percutaneous renal access resulted in a 50% success rate with needle deflection, bowing, and rib interference stated as the main problems [30]. This system consisted of a three degree of freedom robot with a needle injector end-effector. Calibration and distortion correction was done after which robot to image-space registration was completed [31].

Another image-guided robotic system that has been evaluated clinically was developed by Rovetta *et al.* This system used external video cameras and TRUS (transrectal ultrasonography) for robot registration. Accuracies of 1-2 mm were achieved in animal models [32]. Stoianovici *et al.* developed a manual system that mimicked and improved on the standard technique used by the urologist during a percutaneous procedure. Similar to the manual surgical technique explained in section 2.3.3.6 as "key-hole surgery", the skin insertion site, target calyx and

needle was superimposed as a single point in a C-arm fluoroscopic image. This system is shown in Figure 2-10. The needle was held by a novel mechanism driven by a joystick controlled variable speed DC motor enabling automatic needle insertion. The device was locked so the C-arm could be rotated freely to the lateral view. The advantages of this system were that it did not require computer-based vision or a fully actuated robotic system. Accuracies obtained were claimed to be better than that of the standard procedure [33].

Another needle guidance application was that of Radecka, who used CT-guidance and a needle alignment device to position the access needle inside a specified calyx. Bio-modeling for pre-surgery planning was performed prior to the access procedure. In fifteen of the seventeen patients, needle placement was performed successfully with the first attempt [34]. The needle alignment device and its exploded view are shown in Figure 2-11(a)-(b).

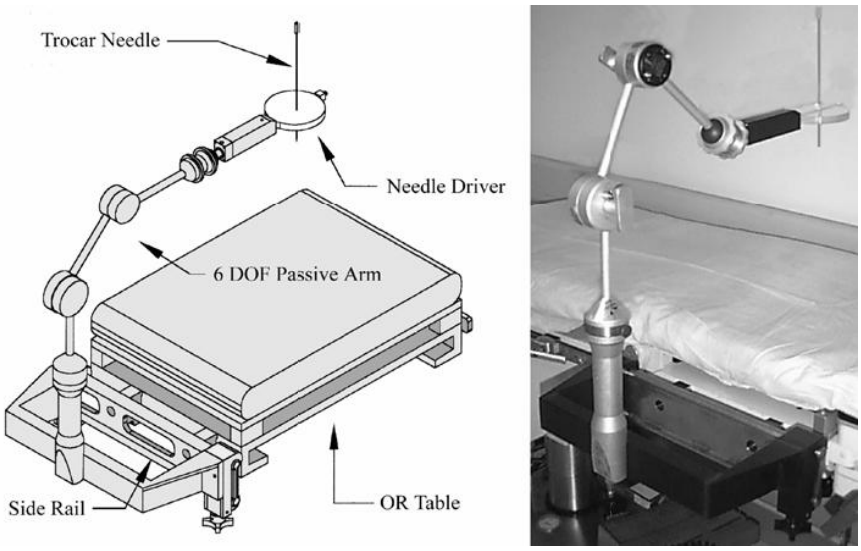

Figure 2-10: System by Stoianovici *et al.*[33]

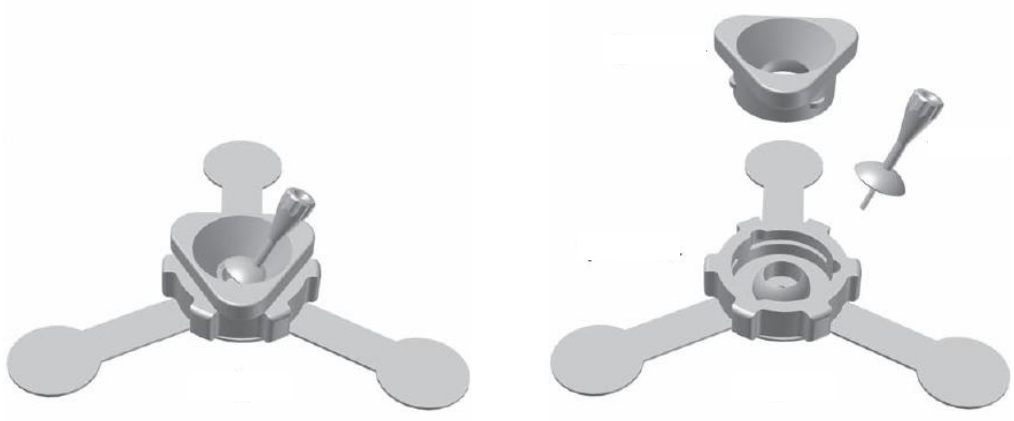

(a) Assembled view (b) Exploded view

Figure 2-11: Needle-guide by Radecka [34]

Cadeddu and associates improved on Stoianovici's original design. A mechanical system for percutaneous access called PAKY (Percutaneous Access to the Kidney), which is a mechanical stereotactic frame and actuated needle system that can be used as a platform for needle placement, was developed. Superimposed fluoroscopic images of the target, access point and needle were used to align the needle by adjusting the orientation of the C-arm imaging system. Clinical percutaneous access was attained in each of the nine evaluated cases [35]. This system is shown in Figure 2-12.

A pending US patent, depicted in Figure 2-13, is that of the Robopsy™ system, a teleoperated, patient-mounted, disposable needle guidance and insertion system. This system's function is the assistance of radiologists in performing minimally invasive percutaneous biopsies under CT guidance.

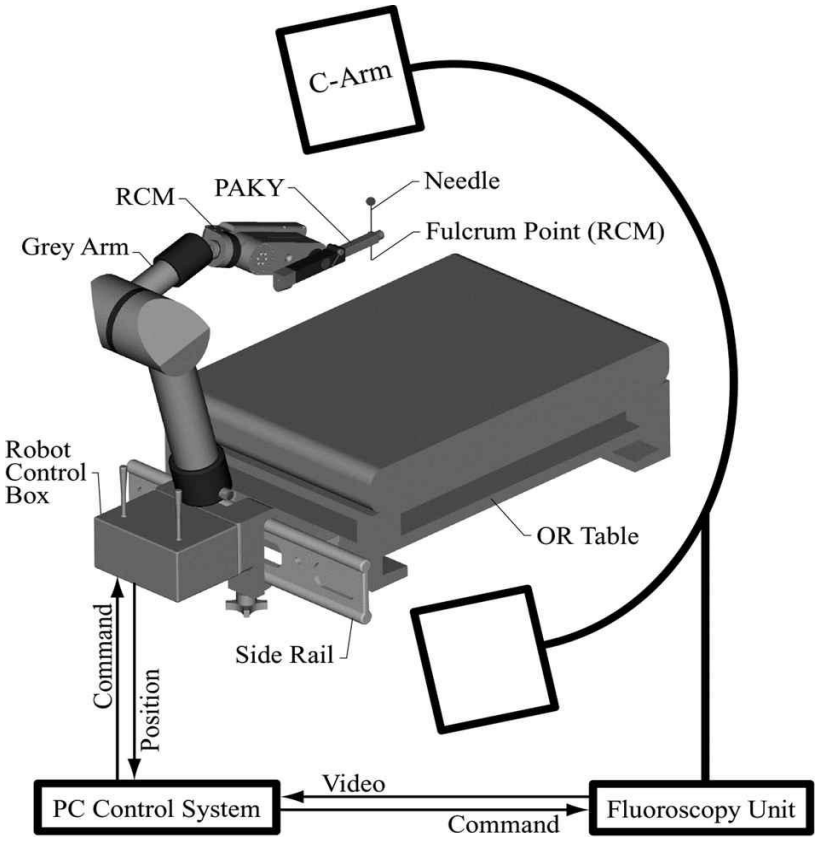

Figure 2-12: Device by Cadeddu *et al.* [35]

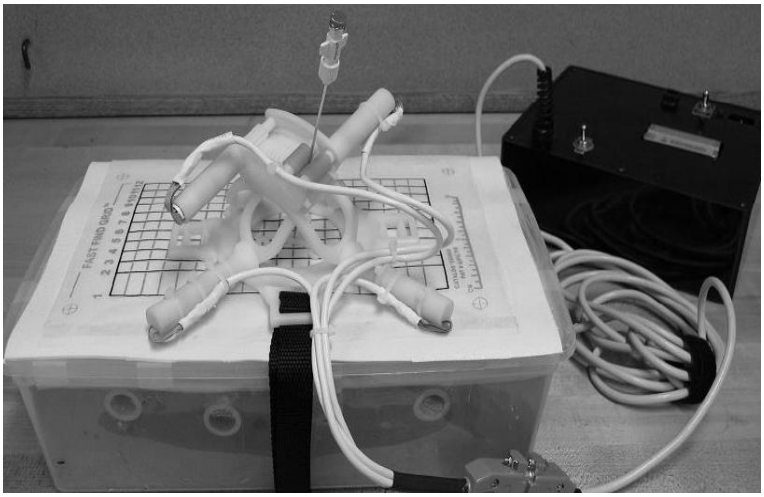

Figure 2-13: ROBOPSY™ system [36]

This system enables radiologists to automatically adjust needle alignment and insert the needle without removing the patient from the CT scanner. No automatic needle positioning calculations are done. The needle is adjusted remotely by the surgeon under continuous CT guidance to confirm when correct angular alteration has been completed. Testing of this system is still ongoing [36].

Vaird *et al.* developed a MRI needle guidance technique where the target point inside the body and the access point on the skin are defined on MRI images, thus defining the required needle trajectory. 3D imaging is used for target visualization, insertion planning and validation of the roadmap. Monochromic CCD (charge coupled device) cameras sensitive to infrared radiation are used in a stereovision setup to determine needle orientation. Current needle orientation relative to the planned needle orientation is then monitored in near real-time during insertion, thus aiding the surgeon in accurate needle placement. Obtained accuracy was 3 mm [37].

Navab *et al.* presented an approach for fluoroscopy image-based guidance of a surgical tool towards multiple targets from fixed or variable entry points. The method is based on visual servoing and required no prior calibration or registration. At least 12 images are required for each targeting sequence [38]. A US Patent by Geiger and Navab describes a method by which a biopsy needle is aligned with a target using needle markers from two fluoroscopic images taken in orthogonal C-arm positions. Needle alignment angles are calculated by a computer system in a two-step procedure, where the first alignment angle is computed and set with the C-arm in position 1, and the second alignment angle is computed and set with the C-arm in position 2 [39].

Another US Patent by Peter and associates describes a system for defining the location of a medical instrument relative to features of a medical workspace including a patient's body region. Pairs of two-dimensional images, obtained by two video cameras making images of the workspace along different sightlines which intersect, are used. A calibration structure is used to define a three dimensional coordinate framework. Appropriate image pairs are used to locate

and track any other feature such as a medical instrument in the workspace with the cameras fixed in their positions relative to the workspace [40].

An additional US Patent by Regn describes CT apparatus equipped with a laser device marking a guide path on a patient for a medical instrument to be used in a medical procedure such as needle puncturing. The CT apparatus produces a planning image and a guide path is identified within the planning image. A computer, using the planning image, and the path identified, automatically adjusts the position of a light source. If necessary a table, on which a patient is supported, is positioned so that a beam from the light source is positioned to coincide with the guide path identified on the image. During insertion the needle is kept in this line of light by the surgeon, thus targeting the defined position [41].

The main problems incurred by most of the mentioned techniques are needle deflection due to tissue resistance and target movement. Techniques that take these factors into account are currently being researched. It was not within the scope of this project to take these factors into account, but to verify whether accurate and operationally viable targeting results could be obtained by implementing stereo vision theory on fluoroscopic images.

2.5 Rationale

Despite the number of apparent solutions described, none of the techniques are currently used in practice, mainly due to their high cost. In developing countries, general use of CT and MRI in hospitals are rare and only used for high risk cases or in certain departments where their use is essential. Fluoroscopy, and in particular C-arm fluoroscopy, is the most commonly used imaging system in the clinical setting that also supplies good quality images.

The targeting technique proposed in this project entails the use of stereo vision techniques on fluoroscopy images to align the insertion needle with a specified calyx. Different from most guidance techniques in the literature, the technique proposed also helps guide the needle to the correct insertion depth with minimal radiation exposure to the patient and surgery team. As cost was identified as the common restriction for implementation of most new systems, an attempt at a low cost system was made. The proposed technique differs from techniques used by Stoianovici in that needle alignment is performed in one adjustment after imaging by the C-arm. In the following chapters the system developed in this project is elaborated on.

CHAPTER 3

3. VISION THEORY, STEREO VISION AND IMAGE PROCESSING

An important outcome of the project was the accuracy-comparison between a standard stereo vision setup with digital cameras and a C-arm fluoroscopy system setup. This was required to substantiate the assumption that a fluoroscopy system, even though quite different in physical appearance and image capturing method, can be described by the defined camera model used in the project. This was realized by implementing the same vision theory on both these setups.

The camera model, as well as the theory regarding lens distortion, calibration and triangulation, will be addressed. Image processing techniques used will also be elaborated on. The theory described is primarily contained in detail in the book *Multiple View Geometry in Computer Vision* by Hartley and Zisserman [42].

3.1 Computer Vision Theory

In this section the concept of the *camera projection matrix* and the information contained within it is explained. The method of calculation and the implementation of the camera matrix in calibrating a camera and finally reconstructing 3D points from a pair of 2D images will be shown.

3.1.1 The Camera Projection Matrix

Simply stated, the mathematical relationship between points in a 2D image and the corresponding points of a 3D object is described by the *camera projection matrix* ($\boldsymbol{P}$) which can mathematically be described as:

$$\boldsymbol{x} = \boldsymbol{P}\boldsymbol{X} \tag{1}$$

where $\boldsymbol{x}$ is a homogeneous 3-vector $(x, y, 1)^T$ which is the pixel in the 2D image, $\boldsymbol{P}$ is the 3 x 4 camera projection matrix and $\boldsymbol{X}$ is a world coordinate in 3D represented by a homogeneous 4-vector $(X,Y,Z,1)^T$. For homogeneous coordinates an extra value ("1" in the case of finite points and lines) is added to the end of the coordinate vector. This notation allows for points and lines at infinity to be represented. The camera projection matrix $\boldsymbol{P}$ contains two pieces of invaluable information; (a) The intrinsic or internal parameters ($\boldsymbol{K}$) of the camera and (b) the extrinsic or external parameters of the camera which include the camera rotation ($\boldsymbol{R}$) and translation matrix ($\boldsymbol{t}$), as well as the position of the camera center ($\boldsymbol{C}$). These matrices and their origin will be explained in the subsequent sections.

Determining the Camera Projection Matrix

The simplest transformation, the 2D homography as described by Hartley and Zisserman, is stated as follows: "Given a set of points $\boldsymbol{x_i}$ in $\boldsymbol{P^2}$ (the 2D projection plane) and a corresponding set of points $\boldsymbol{x'_i}$ likewise in $\boldsymbol{P^2}$, compute the projective transformation that takes each $\boldsymbol{x_i}$ to $\boldsymbol{x'_i}$". The 3D to 2D case will be considered hereafter.

2D to 2D Case

Considering a set of point correspondences $\boldsymbol{x_i} \leftrightarrow \boldsymbol{x_i'}$ between two images, the problem is to compute a 3 x 3 matrix $\boldsymbol{H}$ such that $\boldsymbol{x_i H} = \boldsymbol{x_i'}$ for each $\boldsymbol{i}$. There will be a minimum number of point correspondences needed to compute $\boldsymbol{H}$. The matrix $\boldsymbol{H}$ contains nine entries, but is defined only up to scale. The number of degrees of freedom in a 2D projective transformation is eight. Each point-to-point correspondence also accounts for two constraints, since for each $\boldsymbol{x_i}$ in the first image the two degrees of freedom of the point in the second image must correspond to the mapped point $\boldsymbol{x_i H}$. A 2D point has two degrees of freedom corresponding to the x and y components, each of which may be specified separately. Alternatively, the point is specified as a homogenous 3-vector, which also has two degrees of freedom since scale is arbitrary. It is thus necessary to specify four point correspondences in order to constrain $\boldsymbol{H}$ fully for the 2D to 2D case.

The Direct Linear Transform Method (DLT)

The Direct Linear Transformation, or DLT, is the simplest linear algorithm for computing $\boldsymbol{H}$ from four 2D to 2D homogeneous point correspondences. The DLT method is also utilized in other algorithms used in this thesis. Prior to using the DLT method, an important step called data normalization, is performed which entails translation and scaling of image coordinates. Apart from improving accuracy results, data normalization also makes the algorithm incorporating the normalization step invariant with respect to arbitrary choices of scale and coordinate origin. The normalization method, in short, comprises the following three steps:

1. The specified points are translated so that their centroids are situated at the origin
2. The specified points are scaled so that the average distance from the origin is $\sqrt{2}$, meaning that the average point is at $(1,1,1)^T$
3. The transformation is applied to the two images separately

$\boldsymbol{x_i H} = \boldsymbol{x_i'}$ can be expressed in terms of the *vector cross product* as $\boldsymbol{x'_i} \times H\boldsymbol{x_i} = \boldsymbol{0}$. Now writing the j[th] row of the H-matrix as $\boldsymbol{h^{jT}}$, then

$$H\boldsymbol{x_i} = \begin{pmatrix} \boldsymbol{h}^{1T}\boldsymbol{x_i} \\ \boldsymbol{h}^{2T}\boldsymbol{x_i} \\ \boldsymbol{h}^{3T}\boldsymbol{x_i} \end{pmatrix} \tag{2}$$

The vector cross product, where $\boldsymbol{x'}_i = (x'_i, y'_i, w'_i)^T$ with $w_i, w'_i = 1$ (homogenous coordinates), can now be shown to be

$$\boldsymbol{x_i} \times H\boldsymbol{x_i} = \begin{pmatrix} y'_i\boldsymbol{h}^{3T}\boldsymbol{x_i} - w'_i\boldsymbol{h}^{2T}\boldsymbol{x_i} \\ w'_i\boldsymbol{h}^{1T}\boldsymbol{x_i} - x'_i\boldsymbol{h}^{3T}\boldsymbol{x_i} \\ x'_i\boldsymbol{h}^{2T}\boldsymbol{x_i} - y'_i\boldsymbol{h}^{1T}\boldsymbol{x_i} \end{pmatrix} \tag{3}$$

Substituting $\boldsymbol{h}^{jT}\boldsymbol{x}_i = \boldsymbol{x}_i^T\boldsymbol{h}^j$ in *equation 3* for j-values 1, 2 and 3 produces the following:

$$\begin{bmatrix} \boldsymbol{0}^T & -w'_i\boldsymbol{x}_i^T & y'_i\boldsymbol{x}_i^T \\ w'_i\boldsymbol{x}_i^T & \boldsymbol{0}^T & -x'_i\boldsymbol{x}_i^T \\ -y'_i\boldsymbol{x}_i^T & x'_i\boldsymbol{x}_i^T & \boldsymbol{0}^T \end{bmatrix} \begin{pmatrix} \boldsymbol{h}^1 \\ \boldsymbol{h}^2 \\ \boldsymbol{h}^3 \end{pmatrix} = \boldsymbol{0} \tag{4}$$

Now since the above equation is of the form $A_i\boldsymbol{h} = \boldsymbol{0}$, $\boldsymbol{h}$ is a 9-vector made up of h_i with $i = 1, 2, \ldots, 9$ and A_i a 3×9 matrix as shown in *equation 5*:

$$A = \begin{bmatrix} \boldsymbol{0}^T & -w'_i\boldsymbol{x}_i^T & y'_i\boldsymbol{x}_i^T \\ w'_i\boldsymbol{x}_i^T & \boldsymbol{0}^T & -x'_i\boldsymbol{x}_i^T \\ -y'_i\boldsymbol{x}_i^T & x'_i\boldsymbol{x}_i^T & \boldsymbol{0}^T \end{bmatrix}, \quad \boldsymbol{h} = \begin{pmatrix} \boldsymbol{h}^1 \\ \boldsymbol{h}^2 \\ \boldsymbol{h}^3 \end{pmatrix}, \quad H = \begin{bmatrix} h_1 & h_2 & h_3 \\ h_4 & h_5 & h_6 \\ h_7 & h_8 & h_9 \end{bmatrix} \tag{5}$$

Equation 5 can be simplified to

$$\begin{bmatrix} \boldsymbol{0}^T & -w'_i\boldsymbol{x}_i^T & y'_i\boldsymbol{x}_i^T \\ w'_i\boldsymbol{x}_i^T & \boldsymbol{0}^T & -x'_i\boldsymbol{x}_i^T \end{bmatrix} \begin{pmatrix} \boldsymbol{h}^1 \\ \boldsymbol{h}^2 \\ \boldsymbol{h}^3 \end{pmatrix} = \boldsymbol{0} \tag{6}$$

as only two of the three equations in $\boldsymbol{A}$ are linearly independent. The third row is the sum of the first two equations with a scaling factor. If we have the minimum of four corresponding points we obtain the equation $A\boldsymbol{h} = \boldsymbol{0}$ by stacking each A_i to form $\boldsymbol{A}$. The matrix $\boldsymbol{A}$ has rank 8, and thus has a 1-dimensional null-space which provides a non-zero solution for $\boldsymbol{h}$. The solution can only be determined up to a non-zero scale factor, but $\boldsymbol{H}$ is normally only determined up to scale. The solution $\boldsymbol{h}$ gives the required $\boldsymbol{H}$ with a scale for the vector chosen. In practice the measurements of image points are not exact due to noise. If more than four point correspondences are given with the presence of noise, the system is over-determined and the solution will not be exact. By minimising some cost function it was attempted to find the 'best' possible approximation for the vector $\boldsymbol{h}$. The singular value decomposition (SVD) is a matrix decomposition technique commonly used for the solution of over-determined systems of equations. The

solution is the unit singular vector corresponding to the smallest singular value of A. The explanation of the SVD is covered in *Appendix A*.

3D to 2D Case

For finding the transformation of 3D to 2D points, the same theory is applicable. Normalization is again a prerequisite. The only difference compared to the 2D to 2D case is that the points are scaled so that the distance from the origin is equal to $\sqrt{3}$, or on average $(1,1,1,1)^T$. Again we need to find a camera matrix $\boldsymbol{P}$, now a 3×4 matrix such that $\boldsymbol{x_i} = \boldsymbol{P}\boldsymbol{X_i}$ for all i where $\boldsymbol{x_i}$ is the 2D image coordinates and $\boldsymbol{X_i}$ are the 3D coordinates. The difference is the dimension of the $\boldsymbol{P}$-matrix which in this case is a 3×4 and not a 3×3 matrix. Similar to the 2D to 2D case, the relationship between $\boldsymbol{X}$ and $\boldsymbol{x}$ is

$$\begin{bmatrix} \boldsymbol{0}^T & -w_i\boldsymbol{X}_i^T & y_i\boldsymbol{X}_i^T \\ w_i\boldsymbol{X}_i^T & \boldsymbol{0}^T & -x_i\boldsymbol{X}_i^T \\ -y_i\boldsymbol{X}_i^T & x_i\boldsymbol{X}_i^T & \boldsymbol{0}^T \end{bmatrix} \begin{pmatrix} \boldsymbol{P}^1 \\ \boldsymbol{P}^2 \\ \boldsymbol{P}^3 \end{pmatrix} = \boldsymbol{0} \tag{7}$$

where the 4-vector $\boldsymbol{P}^{iT}$ is the i^{th} row of matrix $\boldsymbol{P}$. For the same reasons as explained in the 2D to 2D case, the last row of the *A*-matrix can be left out leaving only

$$\begin{bmatrix} \boldsymbol{0}^T & -w_i\boldsymbol{X}_i^T & y_i\boldsymbol{X}_i^T \\ w_i\boldsymbol{X}_i^T & \boldsymbol{0}^T & -x_i\boldsymbol{X}_i^T \end{bmatrix} \begin{pmatrix} \boldsymbol{P}^1 \\ \boldsymbol{P}^2 \\ \boldsymbol{P}^3 \end{pmatrix} = \boldsymbol{0} \tag{8}$$

The A-matrix is of the form $2n \times 12$, where n is the number of point correspondences. $\boldsymbol{P}$ can now be calculated by solving $A\boldsymbol{p} = \boldsymbol{0}$ where $\boldsymbol{p}$ is the vector containing the entries of matrix $\boldsymbol{P}$. The minimum number of point correspondences needed for this case is $5\frac{1}{2}\ (\cong 6)$points as the matrix $\boldsymbol{P}$ has 11 degrees of freedom and two equations are obtained per point pair. Similar to the 2D case, the $\boldsymbol{P}$-matrix is calculated implementing the SVD.

3.1.2 The Camera Model

As mentioned in the previous section, the camera matrix provides information regarding the intrinsic as well as extrinsic parameters of a camera. In this section the basic pinhole camera model, used as the starting point for developing most camera models, will be explained. The CCD camera model used in this project, is a camera model with additions to the normal pinhole model. Explanations contained in this section are described in detail by Hartley and Zisserman [42]. Lens distortion plays an important role in the accuracy of 3D point reconstruction and needs to be taken into account in the model. The final camera model used will thus have to consider distortion in the model.

3.1.2.1 Basic Pinhole Camera Model

The basic pinhole camera is the simplest of the camera models and is used commonly as first assumption when applying camera calibration methods. In this model, illustrated in Figure 3-1, a point in space with coordinates $\boldsymbol{X} = (X, Y, Z)^T$ is mapped to a point on the *image plane* at $\boldsymbol{x}$ (distance *f*), where the line joining the point $\boldsymbol{X}$ to the center of the projection meets the *image plane*. We can see that the point $(X, Y, Z)^T$ can be mapped to $(fX/Z, fY/Z, f)^T$ on the *image plane*. Some definitions: the line from the *camera center (C)*, which is the center of projection, perpendicular to the image plane, is called the *principle axis*. The point on the image plane is called the *principle point (p)*.

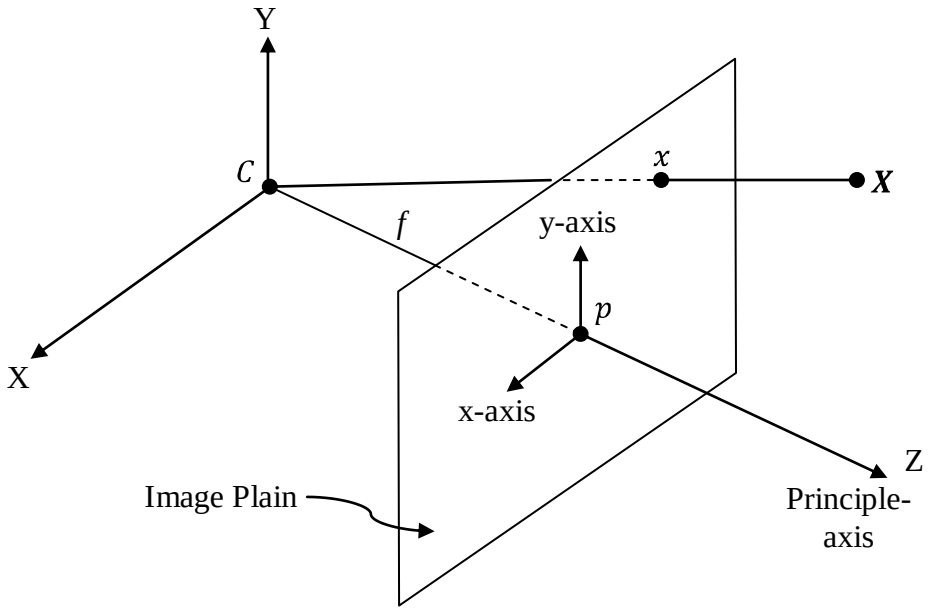

Figure 3-1: Basic pinhole camera model

Central projection is represented using homogenous vectors. World and image coordinates can be related by a linear mapping written as:

$$\begin{pmatrix} X \\ Y \\ Z \\ 1 \end{pmatrix} \rightarrow \begin{pmatrix} fX \\ fY \\ Z \end{pmatrix} = \begin{bmatrix} f & & & 0 \\ & f & & 0 \\ & & 1 & 0 \end{bmatrix} \begin{pmatrix} X \\ Y \\ Z \\ 1 \end{pmatrix} \tag{9}$$

Writing *equation 9* compactly where the world point $\boldsymbol{X}$ is $(X, Y, Z, 1)^T$ and the image point $\boldsymbol{x}$ is $(X, Y, 1)^T$ the following equation results:

$$\boldsymbol{x} = \boldsymbol{P}\boldsymbol{X} \tag{10}$$

where $\boldsymbol{P}$ is the camera projection matrix. If the principle point is not at the center of the image, this is taken into account by placing the principle point coordinates $(p_x, p_y)^T$ in the $\boldsymbol{P}$-matrix as shown in *equation 11*:

$$\begin{pmatrix} X \\ Y \\ Z \\ 1 \end{pmatrix} \rightarrow \begin{pmatrix} fX + Zp_x \\ fY + Zp_y \\ Z \end{pmatrix} = \begin{bmatrix} f & & p_x & 0 \\ & f & p_y & 0 \\ & & 1 & 0 \end{bmatrix} \begin{pmatrix} X \\ Y \\ Z \\ 1 \end{pmatrix} \tag{11}$$

The matrix $\boldsymbol{K}$, called the *camera calibration matrix,* is the matrix containing the intrinsic parameters of the camera.

$$K = \begin{bmatrix} f & & p_x \\ & f & p_y \\ & & 1 \end{bmatrix} \tag{12}$$

Writing *equation 12* in concise form results in

$$\boldsymbol{x} = K[I|\boldsymbol{0}]\boldsymbol{X_{cam}} \tag{13}$$

where $(X, Y, Z, 1)^T$ is written as $\boldsymbol{X_{cam}}$ to show that it is assumed to be located at the origin of the Euclidian coordinate system with the principle axis pointing down the z-axis. The world and camera coordinate frames are related by a translation and rotation, which was earlier noted to be the extrinsic parameters of the camera. 3D points are usually described in the world coordinate system, and are then translated to the camera coordinate system. It is no different in this project. If a 3D point is known in the world coordinate frame, it can be written in the camera coordinate frame as

$$\boldsymbol{x} = KR[I| - \tilde{C}]\boldsymbol{X} \tag{14}$$

where $\boldsymbol{R}$ and $\boldsymbol{C}$ are the parameters related to the camera rotation and center respectively.

3.1.2.2 CCD Camera Model

In CCD cameras, of which the BV Pulsera Fluoroscope used in this project is a good example, it cannot be assumed that pixel height and width are equal. Unequal scaling factors need to be implemented in the x and y directions respectively. This is achieved by introducing an extra factor to the calibration matrix as shown in *equation 15*:

$$K = \begin{bmatrix} \alpha_x & & p_x \\ & \alpha_y & p_y \\ & & 1 \end{bmatrix} \tag{15}$$

where $\alpha_x = fm_x$ and $\alpha_y = fm_y$ and m_x and m_y are the number of pixels per unit distance in image coordinates in the x and y directions respectively. Similarly x_0 and y_0 is the principle point in terms of pixel dimensions with $x_0 = m_x p_x$ and $y_0 = m_y p_y$. Another parameter, called the *skew* parameter (s) negates skewing of the pixel elements in the CCD array if the x-and y-axes are not perpendicular. This parameter is usually zero in normal circumstances. The effect of the skew parameter and shift of the principle point on the camera model is shown in *equation 16*:

$$K = \begin{bmatrix} \alpha_x & s & x_o \\ & \alpha_y & y_0 \\ & & 1 \end{bmatrix} \tag{16}$$

3.1.2.3 Lens Distortion Model

The current camera matrix describes the linear relation between a set of world coordinates and their corresponding image coordinates, but effects such as lens distortion have not been taken into account. The DLT method described ignores the nonlinear effects of lens-distortion.

Two types of distortion, called radial and tangential distortion respectively, can be present. Tangential distortion is caused mainly by imperfect lens component centring. Radial distortion is the result of the concave shape of the lens. The effect of radial distortion is normally much greater than that of tangential distortion and in many distortion models tangential distortion is ignored. In this project tangential distortion is accounted for by allowing the center point of the radial distortion to drift freely on the image plane, separately from the principle point. Two types of radial distortion, termed pincushion and fishbowl distortion, can be encountered. Pincushion distortion causes straight edges of a rectangle symmetrically positioned around the radial center to curve inwards. For fishbowl distortion, the straight lines curve away from the radial center. In this project large pincushion distortion was encountered as shown in Figure 3-2 with the inserted dotted lines emphasizing the bending effect visible on the sides of the square object. The method used to compensate for distortion will be explained in section 3.1.3.

3.1.3 Camera Calibration

The distortion model implemented in this project was introduced by Ma *et al.* [43] and describes the radial distortion in the form of a polynomial expansion as a function of the distance from the radial center. Ma *et al.*'s model will be briefly outlined.

In order to change a distorted coordinate $(\boldsymbol{x_d})$ to an undistorted coordinate $(\boldsymbol{x_u})$, a distance in the x and y directions need to be added. These distances are specified by the correction function $(f(r))$ which is dependant on the Euclidian distance (r) between the distorted coordinate $(\boldsymbol{x_d})$ and center of

radial distortion ($\boldsymbol{c}$). The correction function implemented describes the assumed radial distortion of the lens. This is seen in *equation 17*:

$$f(r) = 1 + k_1 r + k_2 r^3 \tag{17}$$

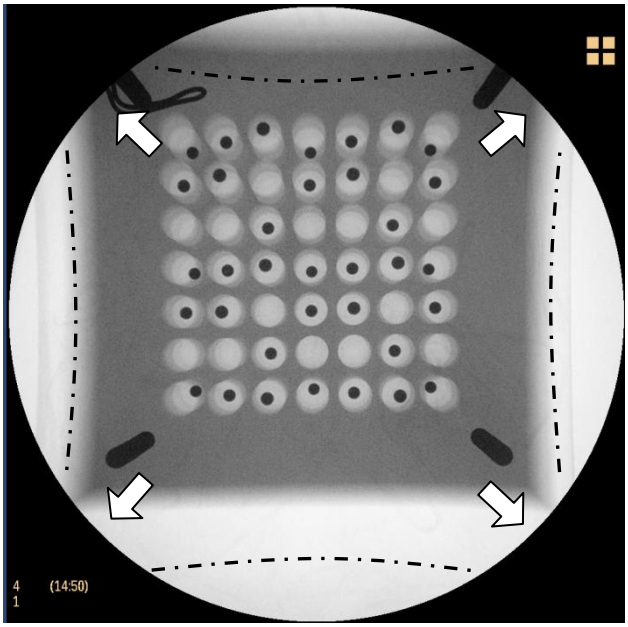

Figure 3-2: Pincushion distortion of BV Pulsera fluoroscopy system

where k_1 and k_2 are the distortion correction parameters to be optimized. The relation between distorted and undistorted coordinates can be shown mathematically by *equation 18*:

$$\boldsymbol{x_u} = \boldsymbol{c} + f(r)(\boldsymbol{x_d} - \boldsymbol{c}) \tag{18}$$

With an initial camera projection matrix and the world-coordinates available, it is evident that the error to be minimized is the difference between the calibration object coordinates initially extracted from the image and the back-projected world coordinates on the image plane. This was implemented by Van der Merwe [44]. The minimization of the back-projection error function will now be explained briefly.

In the case where perfect calibration and coordinate extraction is achieved, the back-projected coordinates should fall exactly on the originally extracted image coordinates. This is rarely the case. The Euclidian distances between the projected and extracted coordinates are called the back-projection errors which are used as the output to be minimized. There are various ways in which the error-set can be used to calculate an output for minimization. Van der Merwe used the sum of the mean and standard deviation of the error-set as minimization output. The parameters to be refined by the minimization function included the camera matrix as well as the distortion coefficients of the distortion model. The optimization

function *fmin* using the Nelder-Mead simplex algorithm, a built in function of the *SciPy* module's optimization package in *Python*, was implemented. The steps of the error minimization are described:

1) A copy of original image coordinates is made.
2) The new image coordinates are calculated using current distortion coefficients.
3) The known coordinates and new image coordinates are used to determine the camera matrix with the method described in section 3.1.1.
4) Using the new camera matrix and corrected image coordinates the image coordinates are projected.
5) The Euclidian distance between the projected and corrected image coordinate are calculated.
6) The sum of the mean and standard deviation of the error-set of Euclidean distances are calculated. If these values converge, the function returns the optimized distortion coefficient and camera matrix values.

Results after implementation of this function will be shown in section 6.3. The parameters for the distortion coefficients, as well as the camera matrices, can now be used in reconstruction of 3D points from a stereo image pair. The implemented stereo vision theory and the method of point reconstruction will be explained in the next section.

3.2 Stereo Vision

In this section the basic stereo vision principles are explained to better understand the reconstruction of 3D coordinates from 2D images. Epipolar geometry, as well as the fundamental matrix, will be covered. Triangulation is also briefly discussed.

3.2.1 Epipolar Geometry

Simply stated, epipolar geometry is the intrinsic projective geometry between two views of the same object or scene. This geometry depends only on the cameras internal parameters and the relative orientations thereof. Epipolar geometry is in most cases motivated by considering the search for corresponding points in a stereo image pair. It is no different in this project. Using the notation from Hartley and Zisserman, points with an apostrophe ($'$) corresponds with the second image and points without to the first image [42].

When a point $\boldsymbol{X}$ is imaged in two views, with $\boldsymbol{x}$ in the first view and $\boldsymbol{x}'$ in the second, the geometry can be visualized as shown in Figure 3-3. This represents a typical stereo vision setup. C and C' refer to the center points of the two respective cameras. The line connecting the two camera centers is called the *baseline*. The baseline intersects the first and second image plane at two points; $\boldsymbol{e}$ and $\boldsymbol{e}'$ for the two image planes respectively. These intersecting points are called the *epipoles*. As shown in Figure 3-3, the point $\boldsymbol{X}$, $\boldsymbol{x}$, $\boldsymbol{x}'$, C and C' are coplanar

which means that a plane can be fitted through the points. This plane is depicted in Figure 3-3 by $\boldsymbol{\pi}$.

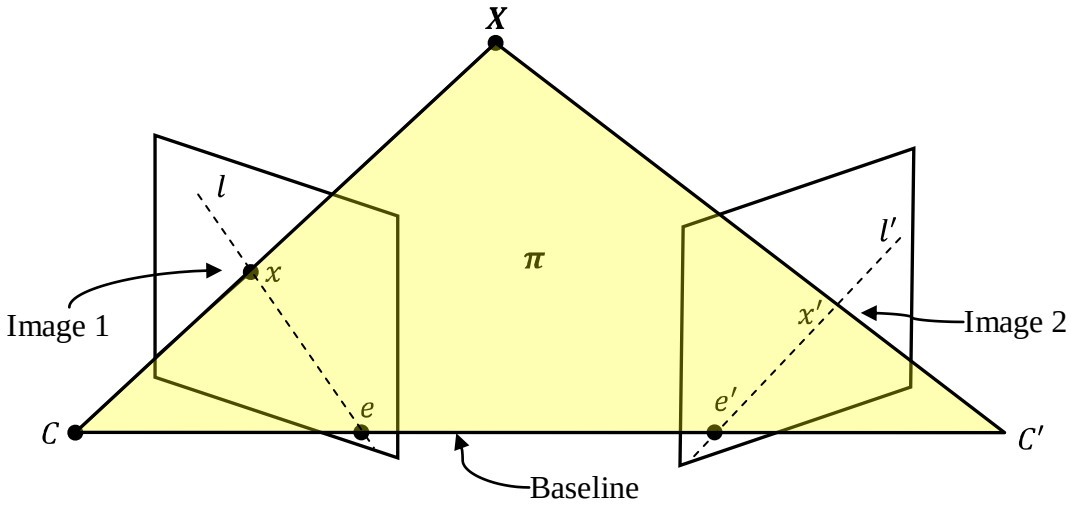

Figure 3-3: Epipolar geometry

This property that the back-projected rays from the two points on the image plane to the 3D point all lie in the plane $\boldsymbol{\pi}$, introduces a method by which a point correspondence search can be aided.

The plane $\boldsymbol{\pi}$ can be defined by the baseline and the ray defined by $\boldsymbol{x}$. From the above explanation, it is known that the corresponding point $\boldsymbol{x}'$ lies in the plane $\boldsymbol{\pi}$. This means that $\boldsymbol{x}'$ lies somewhere on the intersecting line of the plane $\boldsymbol{\pi}$ and the second image plane. This line is denoted as $\boldsymbol{l}'$, and is in effect the view of the ray of $\boldsymbol{x}$ back-projected onto the second image plane. The line $\boldsymbol{l}'$ is called the epiline of $\boldsymbol{x}'$. In the same manner an epiline $\boldsymbol{l}$ of $\boldsymbol{x}$ is shown on the first image plane. The epiline thus allows the search for point correspondences to be narrowed only to a line on an image. As the project entailed the reconstruction of corresponding points chosen by the surgeon on an image pair, a method was needed to improve point selection accuracy. This was provided by the characteristics of epipolar geometry. A matrix, called the *fundamental matrix*, was crucial in its application.

3.2.2 Fundamental Matrix

The fundamental matrix describes the relationship between two cameras and is the basis on which stereo vision is built. The fundamental matrix is the unique 3 × 3 homogeneous matrix of rank 2 that satisfies the following:

$$\boldsymbol{xF} = \boldsymbol{x}' \tag{19}$$

and

$$\boldsymbol{x}'^{T}\boldsymbol{F} = \boldsymbol{x} \tag{20}$$

for all corresponding points $\boldsymbol{x} \leftrightarrow \boldsymbol{x}'$. It is thus a compact algebraic representation of the epipolar geometry of two images. As explained in the description of epipolar geometry, this characteristic is of great importance as the search for the point correspondence of a point chosen in the first image is narrowed to a line, the epiline, crossing the second image. This characteristic is used in the subsequent implementation as will be shown in section 6.4.

Different methods exist to compute the fundamental matrix. The best solution depends on the information available. As the camera matrices of the stereo setup have been obtained (P and P') a method using these two pieces of information was implemented. This method, by Xu and Zhang [45], is outlined as described by Singels [46].

With the two camera matrices known, the ray back-projected from $\boldsymbol{x}$ by P is obtained by solving $P\boldsymbol{X} = \boldsymbol{x}$. The one-parameter family of solutions is then given by

$$\boldsymbol{X}(\lambda) = P^{+}\boldsymbol{x} + \lambda\widetilde{\boldsymbol{C}} \tag{21}$$

where P^{+} is the pseudo-inverse of P, i.e. $PP^{+} = I$ where I is the identity matrix, and $\widetilde{\boldsymbol{C}}$ is the camera center. Two points of interest on the ray are $P^{+}\boldsymbol{x}$ (at $\lambda = 0$) and the camera center $\widetilde{\boldsymbol{C}}$ (at $\lambda = \infty$). These two points are imaged by the second camera P' as $P'P^{+}\boldsymbol{x}$ and $P'\widetilde{\boldsymbol{C}}$ respectively. The epipolar line is the line joining these two projected points, namely

$$\boldsymbol{l}' = \left(P'\widetilde{\boldsymbol{C}}\right) \times (P'P^{+}\boldsymbol{x}) \tag{22}$$

The point $P'\widetilde{\boldsymbol{C}}$ is the epipole in the second image and is denoted by $\boldsymbol{e}'$. Thus

$$\boldsymbol{l}' = [\boldsymbol{e}']_{\times}(P'P^{+})\boldsymbol{x} = F\boldsymbol{x} \tag{23}$$

where F is the matrix

$$F = [e']_{\times}P'P^{+} \tag{24}$$

The matrix F computed by this method must satisfy the condition that for any pair of corresponding points $\boldsymbol{x} \leftrightarrow \boldsymbol{x}'$ in the two images, *equation 25* is satisfied

$$\boldsymbol{x}'F\boldsymbol{x} = 0 \tag{25}$$

3.2.3 Triangulation

Triangulation is the process of reconstructing a point in 3D by two rays that intersect at that point. In the case of perfect calibration and point extraction, the rays from the image pair will intersect. This is not the case in practice due to the inaccuracies of calibration. Linear and non-linear techniques are described to solve this problem. The DLT method used in obtaining the camera projection

matrix is again used during the process of triangulation. The triangulation method implemented is described by Hartley and Zisserman [42].

3.3 Image Processing

From the discussion on stereo vision in the previous sections, it is apparent that corresponding points in the stereo image pair had to be identified and chosen as accurately as possible. The main functions of the implemented image processing techniques were the automatic identification and sorting of the artifact-center pixel coordinates created by the navigation markers. This included the calibration and navigation marker centers in the stereo image pair of the calibration object, and needle-positioning system, respectively. The corresponding marker centers of the calibration object were used as inputs for the calibration function explained in section 3.1.3.

The calibration object, which will be described in section 4.4, creates 35 spherical artifacts on the fluoroscopy stereo image pair whereas the needle-positioning system, described in section 4.5, creates seven artifacts. The methods and techniques used to identify marker correspondences and their centers included noise/artifact reduction, edge detection, contour detection, ellipse fitting, and artifact size filtering. These techniques and the built-in functions of the image processing module used in the Python environment will be discussed. Implementation of the functions will be illustrated in section 6.2.

3.3.1 Noise and Artifact Reduction

A simple noise reduction technique was implemented to provide the capability of reducing possible noise and other artifacts present in the images at the two different camera positions. Using the *Blend* function from the *Python Imaging Library* module, the average of two images taken at the first position was determined, and a new image with reduced artifact intensity was created. The same was done with the images acquired at the second position. The subsequent image processing techniques were implemented on the averaged image of each respective camera position. With a high quality fluoroscopy system such as the BV Pulsera, one image per camera position was sufficient. Noise reduction would however be a crucial step during the procedure when using fluoroscopic systems of lower quality.

3.3.2 Edge Detection

The *cvCanny* algorithm for edge detection as supplied in the *OpenCV* software package from Intel [http://www.intel.com/technology/computing/opencv/], was implemented on a grayscale image to detect edges in the averaged images. As images taken by the fluoroscopy system were automatically contrast-adjusted by the system, choosing threshold parameters for the algorithm were not problematic and automatic threshold adjustment was redundant. The images generated after implementation of this algorithm were used in the contour detection algorithm.

3.3.3 Contour Detection

With the edges showing on the generated images from the *Canny* edge detection algorithm, the contour detection algorithm, *cvFindContours*, from the *OpenCV Library*, was used to identify and draw the closed contours found in each image. This enabled the next algorithm, which approximates and fits an ellipse through every closed contour, to function properly.

3.3.4 Ellipse Fitting and Artifact Size Filtering

The function *cvFitEllipse2* from the *OpenCV Library* calculates an ellipse that best describes a set of closed 2D points in the least-squares sense. The x- and y-coordinates of each ellipse was determined by the function, thus supplying the required marker centers. Artifacts other than the spheres were picked up during edge detection, resulting in faulty ellipse fitting. The fact that the size and relative orientation of the markers were known simplified this problem. The size of the fitted ellipses, in their two axes, was used to filter out the ellipses that did not conform to the prescribed size and shape. This left the centers of ellipses fitted on the calibration markers to be sorted and assigned to their known 3D coordinates. The sorting process will be elaborated on in section 6.2.

CHAPTER 4

4. SYSTEM DESIGN

This chapter gives an overview of the system as well as its main specifications and requirements. The imaging system used, the designed calibration object, and needle-positioning system is described.

4.1 System Overview and Working Principle

The system designed consists of four main components: the imaging system, the calibration object, the needle-positioning system and the user interface and software. Two main processes can be distinguished in the implementation of the system: *calibration* (including distortion correction) and *targeting*.

During the *calibration* process a stereo image pair of the calibration object is acquired and used to calibrate the imaging system in the two positions. This is done with the aid of the user interface, calibration software and distortion correction algorithms. This process is shown diagrammatically in Figure 4-1 where calibration object images are acquired by the C-arm in position 1 and position 2 and these images are exported to the PC with the installed software.

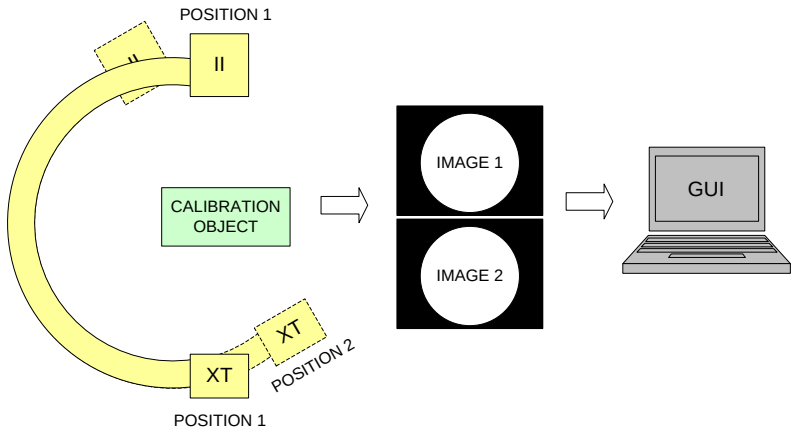

Figure 4-1: System design: Calibration

During the *targeting* process, stereo images of the target and needle-positioning system are acquired from the same relative positions used during calibration. The relative orientation of the needle to that of the target is computed by utilizing the user interface and targeting software. The translational and rotational needle adjustment for accurate targeting is determined. Hereafter the needle-positioning system is manually adjusted to these specifications and the

needle is inserted through the needle guide to the specified depth. This process is shown diagrammatically in Figure 4-2.

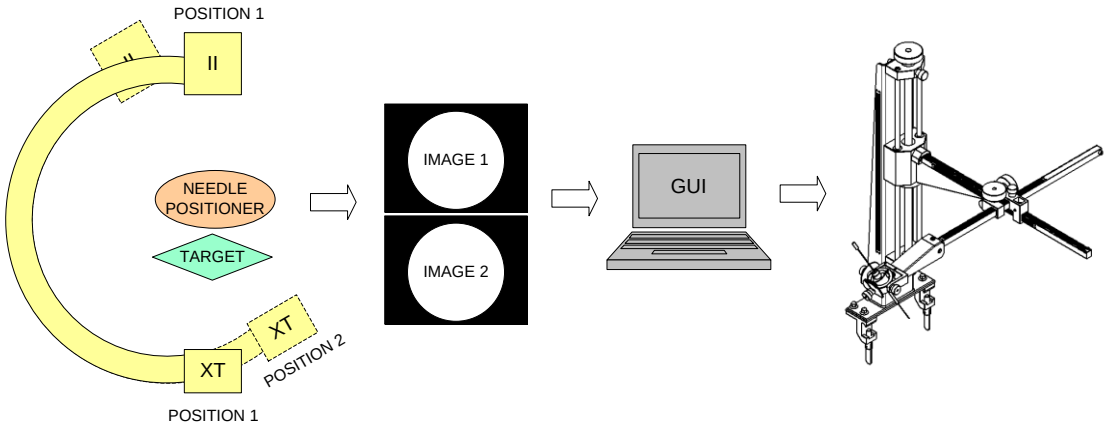

Figure 4-2: System design: Targeting

4.2 Specifications of System

The following *general specifications and outcomes* were defined for the system and implementation thereof:

- Rapid and reproducible, requiring one attempt at kidney access only.
- Performed by urologists in the theatre environment.
- Cost effective and implementable in the South African medical environment.
- Safe for the patient and operator.

The following *system specific specifications* were defined:

- Implementable on left and right infected kidneys.
- Designed as to not interfere with the C-arm used to acquire the photos.
- Designed to prevent occlusion of the x-ray image by the mechanical components.
- Mechanically stable.
- Easily attachable and removable to and from the surgery room bed.
- Needle positioner requires 5 degrees of freedom for needle placement.
- Require an adequate movement range making insertion possible in obese as well as underweight patients.
- Movement restricted to allowed access orientations only.
- Manually adjustable by the surgeon.
- Accuracy of the system required to be better than 3 mm as the average diluted kidney calyx radius was estimated to be larger than 5 mm.

4.3 Imaging System

The specific fluoroscopy system used in this project is a *BV Pulsera C-arm system* from *Philips Medical*, shown in Figure 4-3(a). Shown in Figure 4-3(b) are the degrees of freedom of the system.

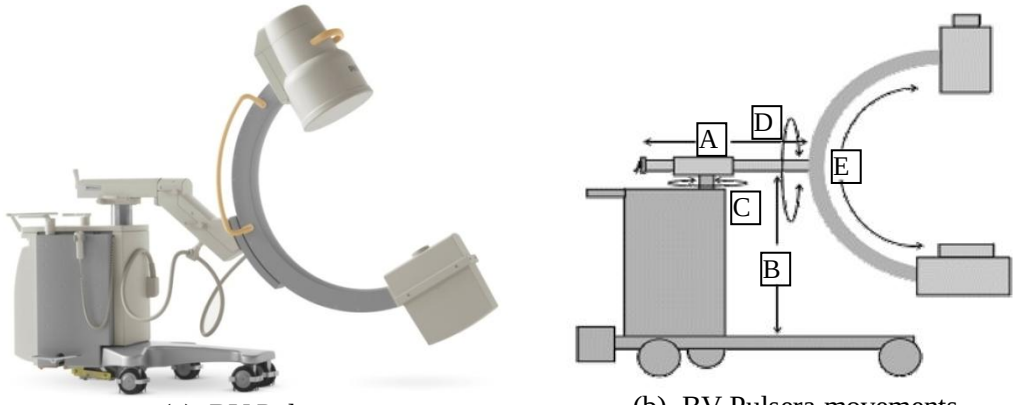

(a) BV Pulsera (b) BV Pulsera movements

Figure 4-3: BV Pulsera C-arm system (Philips Medical) [tdtonline.org]

The C-arm system lends itself to a stereo vision setup due its large range of possible movements. Longitudinal (A), vertical (B), wig-wag or side-to-side (C), rotational (D), and angular movement (E) is possible by the arc housing the X-ray Tank (XRT) on the one end and the Image Intensifier (II) on the other. Only accurate and repeatable angular movement was of importance. The first stereo image was taken with the C-arm in the 0° position from now on called "position 1" and the second image with the C-arm orientated away from the surgeon by 20°; from now on called "position 2". This is illustrated in Figure 4-4.

Higher accuracy coordinate reconstruction is possible with a larger angle between the stereo pair. The optimal position would be with the two cameras in orthogonal positions. Constraints regarding the implementation environment forced the author to use as small an angle as possible. Factors preventing the use of the optimum orthogonal camera positions were the occlusion of the kidney by the ribs and other organs as well as interference of the C-arm by the bed. A 20° angular orientation adjustment was implemented. The effectiveness of such a small angle had to be verified by testing. The Pulsera delivers a 23 cm diameter nominal field size and delivers images in digital format with a 1280 x 1024 pixel resolution. The angular adjustment and nominal field size of the imaging system are the limiting factors in the size of the calibration object as will be illustrated in the next section.

4.4 Calibration Object

The function of the calibration object has been discussed. In most stereo vision setups, 2D calibration objects are used for their ease of manufacture and low cost.

An important advantage of 3D calibration objects opposed to 2D objects is that 3D objects can be measured accurately by means of touch probe system as was the case in this project.

As a fluoroscopy imaging system has the advantage of being able to see "through" solid radiolucent materials, a 3D calibration object was used to calibrate the C-arm. 3D calibration objects have been implemented in the calibration of fluoroscopy systems by Mitchske, using a helical marker-configuration, and Navab, using a cubical marker-configuration respectively [47, 48]. The main features to be taken into account when designing a 3D calibration object for use in a fluoroscopic stereo vision setup are object materials, marker grid size, marker shape, size and spacing. With images taken from two positions and the markers in different planes, marker occlusion by adjacent markers was one of the main problems. As mentioned in the previous section, a 20° orientation adjustment was selected for the stereo setup. The effect of this decision on calibration object size is illustrated in Figure 4-4. The hatched area shown in Figure 4-4 represents the area in which the calibration object must fit if the whole object is required to show in both C-arm images.

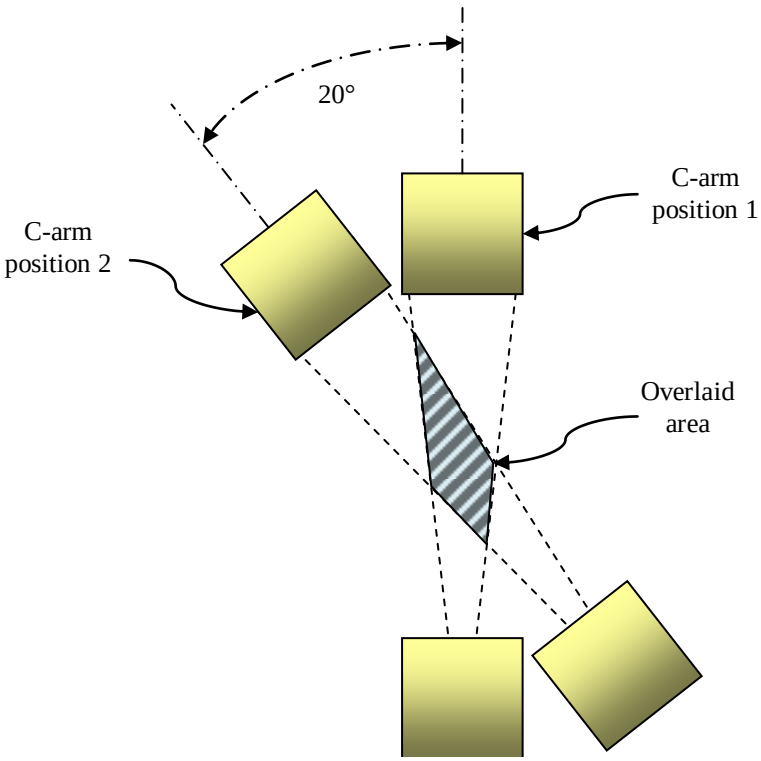

Figure 4-4: C-arm orientation versus calibration object size

With an increase in rotation angle, the shape and size of the overlying area changes. Targeting accuracy depends heavily on the area percentage of the calibration images used during the calibration procedure. As large a calibration grid as possible still registering all the markers on the stereo image pair was needed. The calibration object used in this project consisted of three dowel-

stacked 120 mm x 120 mm x 30 mm Perspex blocks each containing a number of metallic spherical markers of 4 mm diameter. 35 markers were spaced throughout the calibration volume in specified depth holes. The marker-configuration consisted of nine markers in level 1, sixteen markers in level 2 and ten markers in level 3, forming seven distinct lines when seen from above. The marker-configuration is shown in Figure 4-5.

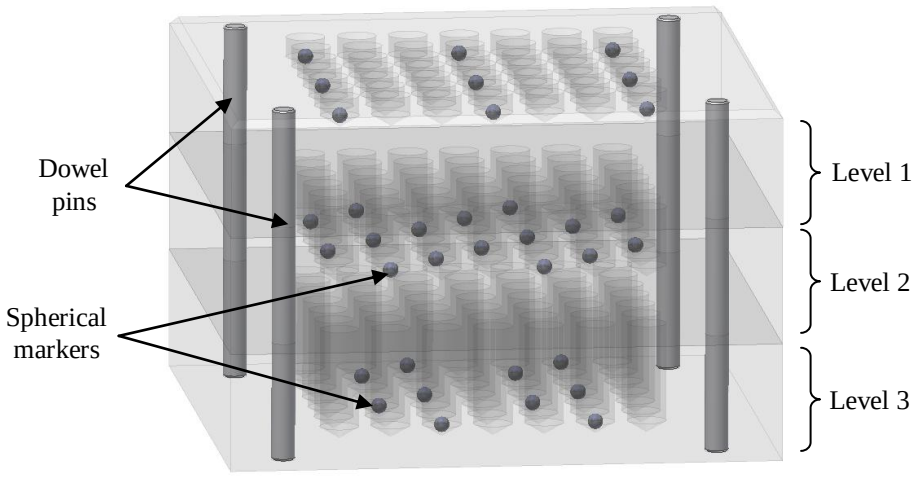

Figure 4-5: 3D calibration object

Measurement of marker center positions were performed on a Mitutoyo Bright 710 coordinate measuring machine (CMM) with a reported volumetric accuracy of 6 μm. The measurement process was performed on a level by level basis. Level 3 was firmly fixed to the measurement table with the dowel pins inserted. The CMM's coordinate system was reset and a new coordinate system was specified by defining one of the corner markers as the origin. All other markers were defined relative to the new origin. After measurement of all markers in level 3, the second level was inserted on the dowel pins. The same procedure was repeated for level 2 and level 1. The configuration used supplied an accurate calibrated volume of 80 x 80 x 80 mm.

4.5 Needle-positioning System

A mechanism was needed by which a needle could accurately be transported and guided for introduction into a patient during a PCNL procedure. This system had to refrain from interfering with the imaging system, surgery bed, patient or surgeon during the procedure but at the same time provide the necessary information with respect to needle orientation and position needed by the targeting algorithms.

The developed needle-positioning system is discussed in two sub sections: (a) the *gantry system*, responsible for the translational movement and (b) the *needle-alignment mechanism*, responsible for needle angular orientation. The complete needle-positioning system is shown in Figure 4-6. The technical drawings of the designed parts are included on the accompanying CD. The main assembly

drawings are shown in *Appendix B*. As one of the requirements of the system was its economic feasibility, a manual system was developed with no motorized parts, encoders or any other electronic components. The developed system is manually adjusted by the surgeon. Other requirements of the system were repeatability, ease of use and a targeting accuracy adequate to successfully target a 10 mm diameter target.

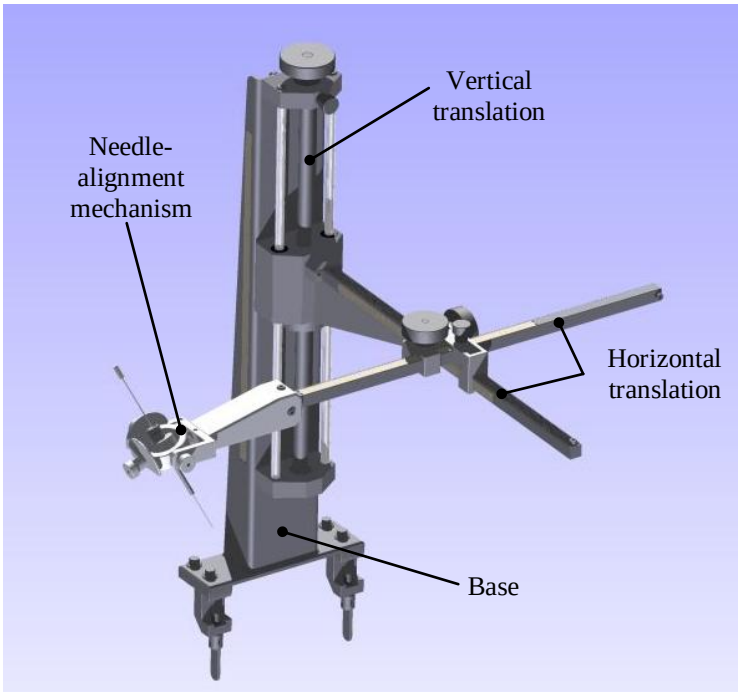

Figure 4-6: Needle-positioning system

4.5.1 Gantry System Design

The gantry system is responsible for accurate and controlled needle movement in the horizontal and vertical planes. Three types of positioning systems were investigated: (1) *perpendicular axes*, (2) *robotic arm* and (3) *hybrid systems*.

Perpendicular axes translation configurations are frequently seen in high precision positioning devices such as micromanipulators. The main advantage of this configuration is the independent movement of each axis, simplifying positioning. A more complicated form of positioning is the robotic arm. In this format, the different axes are interdependent, leading to more complicated positioning algorithms. This configuration however allows angular orientation of the end-effector without additional joints. A further advantage of the latter to the fixed axes system is a potentially more compact design, as its axes need not be in full extension unless the movement requires it. Another alternative is a combination of the abovementioned positioning systems. In studies done by Stoianovici, Potamianos and Cadeddu a robotic arm system was used for needle manipulation [27, 31].

Factors influencing the selection of the gantry concept were complexity, cost and space restrictions. As a first iteration for a proof-of-concept design a hybrid system concept was selected due to its simple nature compared to the robotic arm design. In order to keep the effect of the designed system on the surgery environment as small as possible, the configuration of the three axes was carefully chosen. The movement configuration shown in simplified form in Figure 4-7 had the least effect on the movements of the surgeon, did not interfere with the imaging system and provided a solid base for the needle-alignment mechanism.

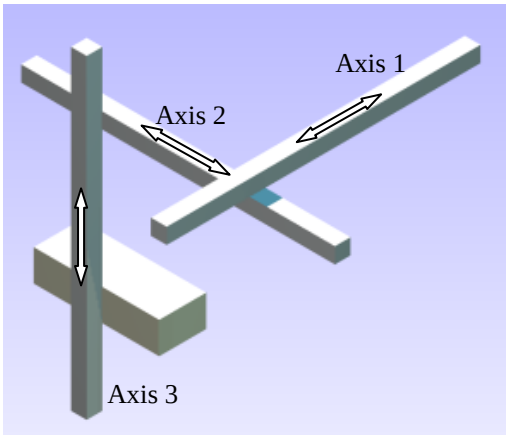

Figure 4-7: Gantry axes configuration

The next design choice was that of the concept for axes translation. Options investigated included (1) *linear guides*, (2) a *rack and pinion mechanism*, (3) *screw drives* and (4) *linear slides*. Important factors taken into consideration included weight, cost, control, accuracy and ease of use.

Vertical Translation

From Figure 4-7 it is evident that the vertical axis carries the combined weight of the other two axes as well as the end-effector. A safe mechanism strong enough to carry the weight, while still providing easy adjustment, was needed. A precision ball screw assembly, consisting of a 16 mm diameter precision rolled ball screw shaft and accompanying sealed linear ball screw nut (Bosch Rexroth AG) was used in combination with a sturdy stainless steel base. The mechanism is self-locking, minimizing the hazard of unplanned needle movement. High precision guide shafts with closed type super linear bushings (Bosch Rexroth AG) were used to ensure that the resultant moment caused by the weight of the horizontal axes did not influence the functioning of the ball screw nut and precision linear movement or have a detrimental effect on accuracy. A machined aluminum part, from now called the "*main block*", which serves as fixing point for the horizontal axes, moves with the fixed ball screw nut. A single direction thrust bearing (FAG Incorporated) at the base carries the resultant load while a machined Vesconite bush ensures smooth shaft rotation. Height adjustment is done by turning a knob fixed to the ball screw shaft. A securing knob was added as extra safety measure. Figure 4-8 shows the vertical axis assembly as well as the

translation brought about by the turning of the knob. The adjustment resolution per rotation of the knob is 2 mm. A vertical translation range of 400 mm is possible, which is more than adequate to accommodate very slim and obese patients. Also visible in Figure 4-8 is the base that is fixed to the steel protrusions of the bed via two clamps.

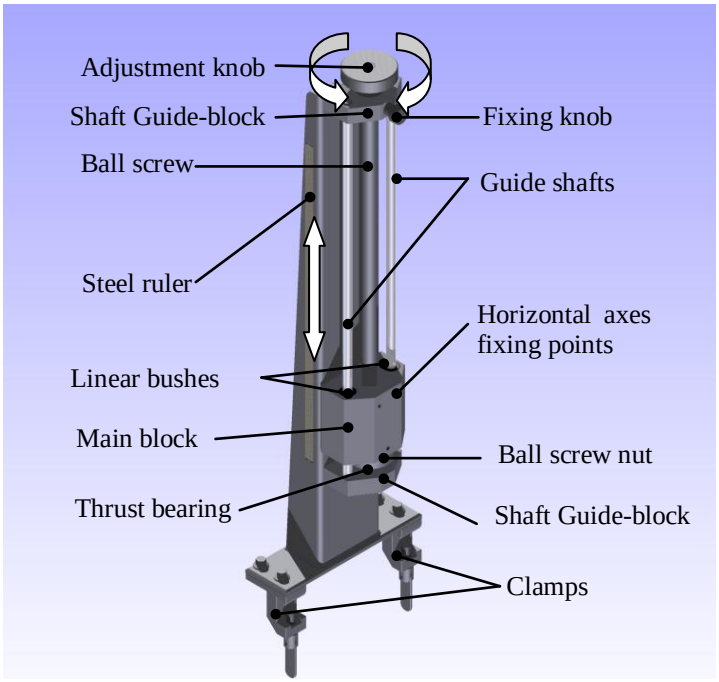

Figure 4-8: Vertical axis assembly

Horizontal Translation

Large moments are created when the gantry systems x-and y-axes are translated to their extents. Despite its weight, a rack and pinion option provided flexibility to the design and simplified addition of components such as fixing knobs. In order to minimize the bending and torsion forces on the y-axis, a web and 'moment counter' was added to the design as shown in Figure 4-9(a). The 'moment counter', a small aluminum part that is fastened to the main block, fits tightly over the rack preventing twisting of the rack itself. An aluminium guide-block, also housing the adjustment and fixing knobs, was designed to ensure high precision linear movement of the two rack and pinion configurations. The configuration used resulted in an adjustment resolution per rotation of the knob of 5 mm in the y-axis and 3 mm in the x-axis direction. The horizontal plane translation system consisting of the x-and y-axes is shown in Figure 4-9(a). The guide-block is shown in Figure 4-9(b). Steel rulers set into each of the axis show their respective position to the nearest 0.5 mm. The horizontal axes cover a 450 mm x 450 mm area above the bed at the height of the vertical axis.

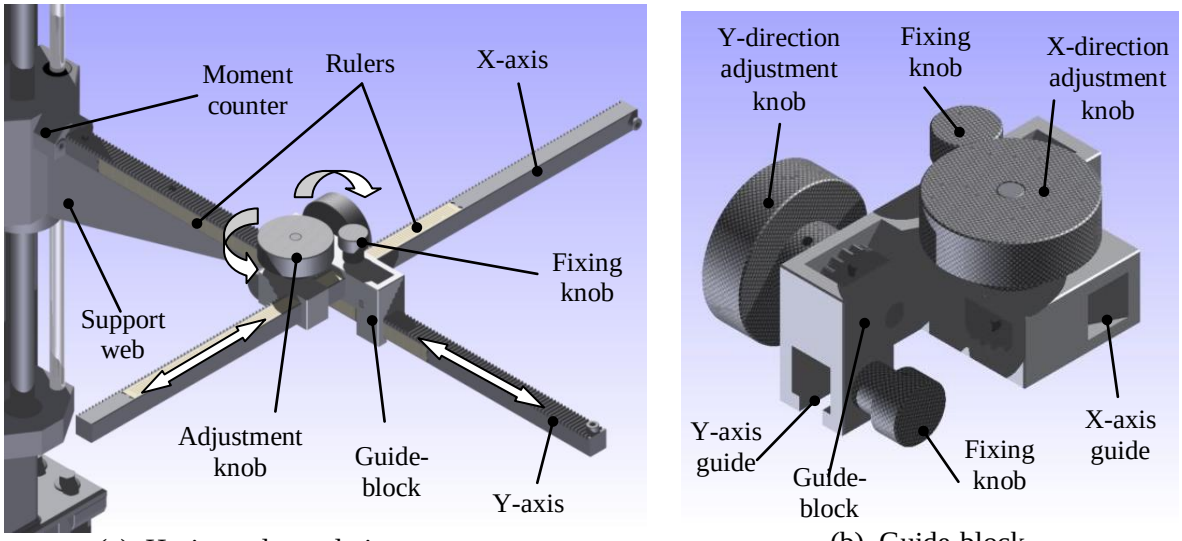

(a) Horizontal translation components (b) Guide-block

Figure 4-9: Horizontal plane system assembly

4.5.2 Needle-Alignment Mechanism Design

The function of the needle-alignment mechanism, as the name states, is the accurate alignment of the needle guide to ultimately serve as targeting platform for the surgeon during PCNL. The final design is shown in Figure 4-10 to simplify further explanations.

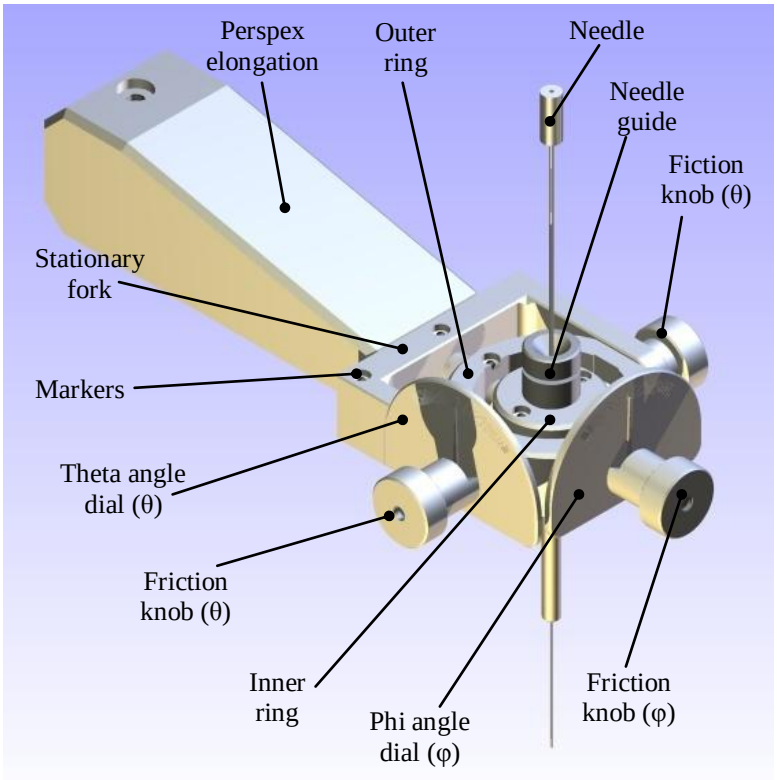

Figure 4-10: Needle-alignment mechanism

In order to align a needle with a specified vector, only two rotational degrees of freedom are required. The imaged area of the *BV Pulsera* is approximately 200 mm in diameter, leaving limited space for the aligning mechanism and target. The mechanism therefore had to be as small as possible to keep target visibility un-occluded. It must be mentioned that manual needle insertion was a specific requirement. Factors such as tissue deflection during needle progression through the tissue and obstructions such as ribs or other physiological anomalies were not addressed. Perspex, a radiolucent acrylic, was used in the manufacturing of the mechanism in its entirety.

If the robotic arm configuration was selected in the gantry system design section, the orientation of the needle could have been integrated with the translation movement. As stated, this would introduce a much higher level of complexity to the control of needle positioning. A needle-alignment mechanism that could function independent of needle translation was selected. In order to keep the point of rotation stationary for both the needle rotations, two concepts were investigated; (a) the *two-joint* and (b) *gyro-mechanism*. These two concepts are shown in their simplest form in Figure 4-11(a) and Figure 4-11(b) respectively. Also shown are their axes of rotation.

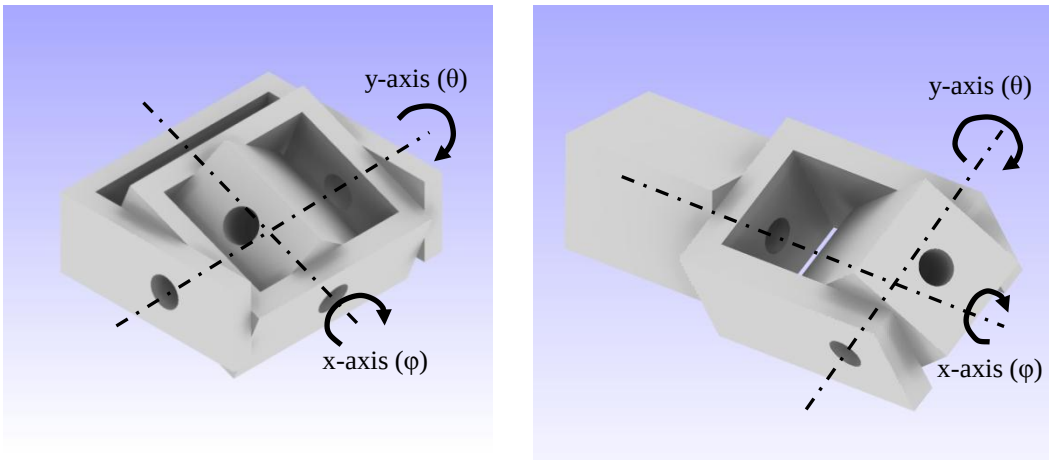

(a) Gyro-mechanism (b)Two-joint mechanism

Figure 4-11: Angular orientation mechanism concepts

Either of these concepts could have been implemented with similar results. Even though the *two-joint* mechanism consisted of fewer parts, angular adjustment and locking of the axis would be problematic. The gyro-configuration was selected as it provided better surfaces for navigation marker placement as well as space for the adjustment- and locking mechanisms. This will be clarified in the subsequent explanation of the design.

Needle Rotation

The *gyro-mechanism*, as shown in Figure 4-12(a), consists of three main components for the two axes of rotation; (1) a *fixed base*, (2) an *outside ring* for

rotation around the y-axis (θ) and (3) an *inside ring* for rotation around the x-axis (φ).

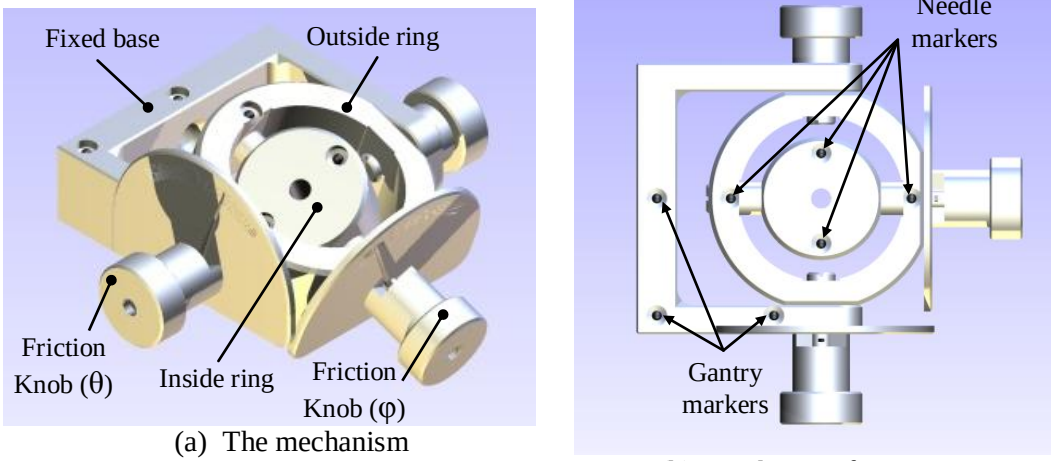

(a) The mechanism

(b) Marker-configuration

Figure 4-12: Gyro-mechanism and marker-configuration

Also shown in Figure 4-12(a) is the mechanism which utilizes friction, used to lock the needle into place once it has been set to its designated angle of rotation. As the Perspex knobs are tightened, the rings are pulled tightly against the base or outer ring. Spacers keep the components at the correct positions and prevent the dial pointers from being damaged. To display the angle of rotation to the operator around the x-and y-axes, engraved dials with pointers were used. The range of the needle rotations are ±40° around both axes resulting in the needle rotation area shown in Figure 4-13.

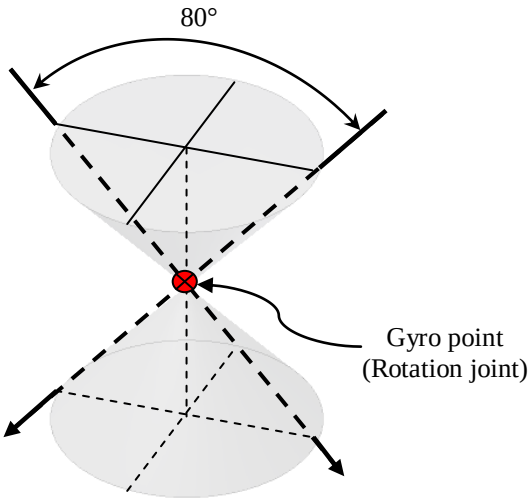

Figure 4-13: Needle movement extents

It can be recalled that navigation markers are needed for coordinate identification and ultimately needle manipulation. The placement of the markers

is important for proper imaging in order to provide the needle orientation as well as gantry translation direction information to the algorithms. Two groups of markers on the needle-alignment mechanism can be distinguished: (a) *gantry markers* and (b) *needle markers*. The *gantry markers* are represented by three 2 mm diameter markers on the fixed base of the *gyro-mechanism*. Two 2 mm diameter markers on the *outside ring* and two 2 mm diameter markers on the *inside ring* of the *gyro-mechanism* represent the *needle markers*. The marker-configuration is shown in Figure 4-12(b). The reason for the used configuration will become evident in chapter 5 where the use of each marker-set will be discussed.

Needle Holder and Guide

The mechanism used to hold the needle during the positioning and insertion procedure consists of three parts: (1) the *cap* (2) the *alignment cylinder* and (3) an *O-ring*. These three parts are shown in Figure 4-14 in exploded form. This mechanism allows the surgeon to adjust the friction by which the needle is held in position and guides the needle during the insertion procedure.

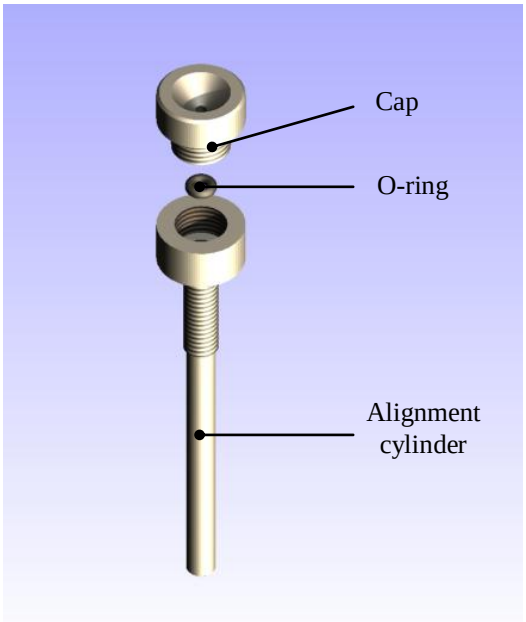

Figure 4-14: Needle holder and guide

The *cap*, fitted with a conical needle inlet aiding needle insertion, is screwed into the *alignment cylinder*. This compresses the *o-ring* with an outside diameter of 1.8 mm into a conical indentation resulting in the gripping of the needle. The assembled needle holder is screwed into the *inside ring* of the *gyro-mechanism*, fixing it in the specified target vector as shown in Figure 4-15.

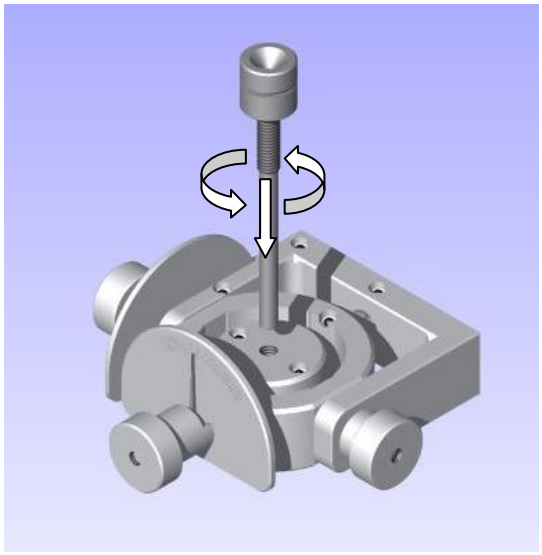

Figure 4-15: Needle holder insertion into alignment device

All parts were designed to be manufactured in-house. Perspex, stainless steel, aluminum and Vesconite were the materials used in the manufacture of the system. Machining tolerances of the parts varied according to the needs of the specific part. Tolerances of specific parts are shown on the manufacturing drawings included on the accompanying CD. Shown in Figure 4-16 is the assembled needle-positioning system with a needle inserted in the needle holder. The development cost of the complete system was estimated at R35 000. This includes material costs, labour costs and purchased parts. Assembly of the entire needle-positioning system was possible in approximately four minutes.

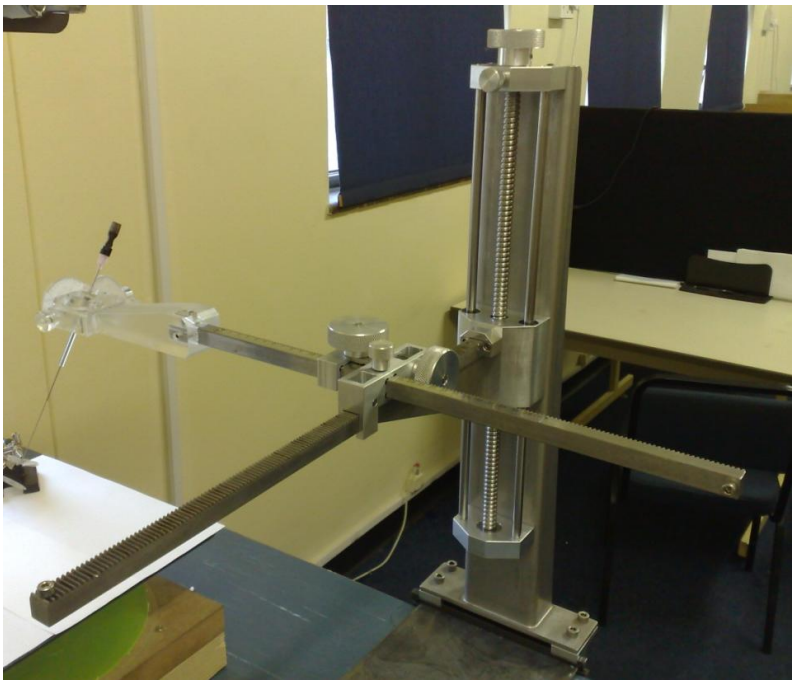

Figure 4-16: Assembled needle-positioning system with inserted needle

CHAPTER 5

5. TARGETING COMPUTATION

This chapter describes the mathematical computations implemented in determining the required needle translation and rotation for targeting. Concepts such as coordinate systems, the method of coordinate transformation and the determination of the center of movement will be discussed.

5.1 Coordinate Systems

Two axes systems or coordinate systems needs mentioning. The "*world coordinate system (WCS)*", defined during the calibration process, is dependent on the calibration object position during camera calibration. The "*gantry coordinate system (GCS)*" is defined during the navigation marker selection process.

World Coordinate System

The WCS is defined during the calibration procedure and conforms to the axes system of the calibration object. The WCS is shown in Figure 5-1 with the origin situated at the bottom left of the object. All triangulated points are reconstructed to this frame of reference.

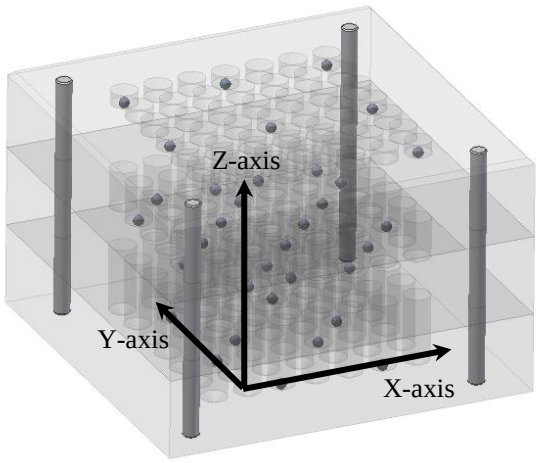

Figure 5-1: World coordinate frame (WCS)

Gantry Coordinate System

The GCS is a coordinate system that plays a vital role during accurate needle positioning. The GCS defines the axes of movement of the needle and is needed when the translation and rotation of the needle is computed. The GCS is defined by the *gantry markers* discussed in section 4.5.2 and shown in Figure 4-12(b). The

three *gantry markers* are used to define gantry origin, y-axis and x-axis by calculating the unit vectors from the origin coordinates to the other two marker coordinates. This results in the x- and y-axis shown in Figure 5-2. Each unit vector is computed by

$$\boldsymbol{u_x} = \frac{\boldsymbol{x}}{|x|} \tag{26}$$

where $\boldsymbol{u_x}$ is the unit vector of the vector $\boldsymbol{x}$ and $|x|$ is the magnitude of the vector. These unit vectors are used in transforming points from the WCS to the GCS as will be shown subsequently.

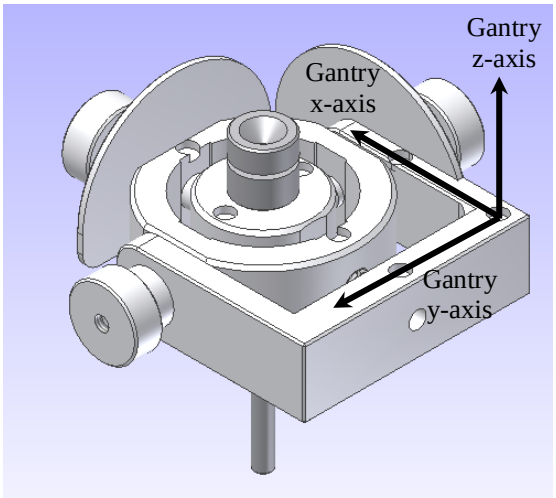

Figure 5-2: Gantry coordinate frame (GCS)

In order to find the gantry z-axis, the cross product between the gantry x and y axis is computed, resulting in a vector perpendicular to the plane formed by the x- and y-axis, i.e. the gantry z-axis, also shown in Figure 5-2. As perfect point selection is impossible, the x-and y-axis are not exactly perpendicular, resulting in a non-orthogonal coordinate system. An orthogonal system is vital for further computations. In order to correct this, the cross product of the gantry y-axis and the z-axis is computed, resulting in a perfect orthogonal x, y, z-axes system.

Transforming WCS-Coordinates to GCS-Coordinates

To make accurate translations and rotations possible, movement direction must be defined in the same coordinate system in which translation takes place. All reconstructed coordinates thus had to be transformed to the GCS before further calculations. The *dot-product* is used. This transformation of a coordinate from the WCS to the GCS is shown in *equation 27*:

$$\begin{bmatrix} \boldsymbol{u_x} \\ \boldsymbol{u_y} \\ \boldsymbol{u_z} \end{bmatrix}^T_{Gantry} (x, y, z)^T_{WCS} = (x, y, z)^T_{GCS} \tag{27}$$

where $\boldsymbol{u_x}$, $\boldsymbol{u_y}$ and $\boldsymbol{u_z}$ are 1×3 unit vectors of the gantry x-, y- and z-axis arranged in a 3×3 matrix. The coordinate to be transformed is 1×3 matrix denoted by $(x, y, z)_{WCS}$. The *dot-product* returns a 1×3 matrix denoted by $(x, y, z)_{GCS}$ which is the transformed coordinate in the GCS.

5.2 Defining Targeting Objects

Gyro-Center and Needle Orientation Determination

The four *needle markers* described in section 4.5.2 have two functions: (a) defining the needle orientation and (b) the center of rotation of the *gyro-mechanism*. The coordinates of the center of rotation of the *gyro-mechanism* are determined in a two-step procedure. The cross product between the *outside ring* marker vector and the *inside ring* marker vector is computed resulting in a orthogonal vector describing needle orientation. This is called the *needle vector*. By moving in this new vector direction for a specified distance from the coordinate halfway between the *inside ring* markers, the *gyro-center* coordinate is obtained. The plane, of which the orthogonal vector is the *needle vector*, is shown in Figure 5-3. Also shown are the vectors defined by the *outside* and *inside ring* and the defined *gyro-center*. The fixed distance to the *gyro-center* was determined by touch probe measurement on the CMM to be 8.9 mm.

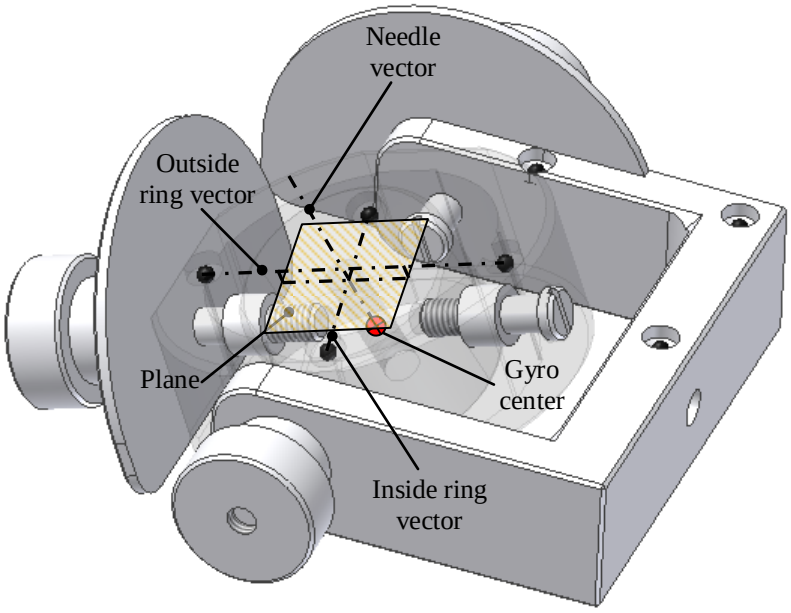

Figure 5-3: Gyro-center and needle orientation

Calyx Orientation Determination

Obtaining targeting coordinates of the kidney calyx is the most challenging of the needed targeting variables as no markers specifically provide corresponding points on the two images.

As explained in section 3.2, a means has been implemented to simplify point correspondence selection. The correspondence area of a selected point in the first image of a stereo image pair can be presented on the second image by means of a line, called the epiline. A *four*-and *two-point* selection method was implemented in finding kidney calyx orientation and spatial position. Implementation of the methods will be shown in section 6.6.

- In the *four-point* method, two points are selected at the one end of the calyx structure edge and another two on the opposite end of the calyx. Care is taken to choose distinct points in order to easily recognize the correspondences in the second image. In the *four-point* method, the calyx vector is determined by calculating the coordinate halfway between the first and second selected point-pair respectively, and subtracting these two coordinates. This vectors' unit vector defines the target kidney calyx orientation. The four chosen points at the two ends of the calyx with the determined target kidney calyx orientation vector is depicted in Figure 5-4(a) and (b).

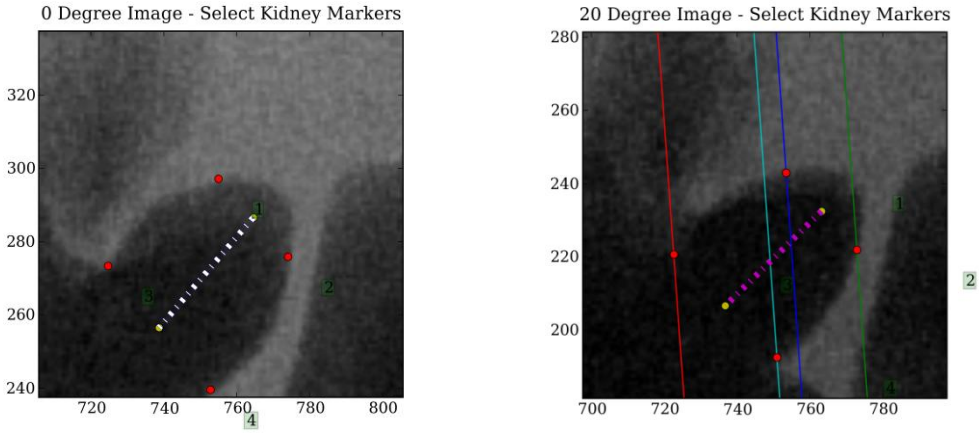

(a) 0° image (b) 20° image

Figure 5-4: Four-point selection method example

- During the *two-point* method, a point is selected centrally at the one end of the calyx structure edge and another on the opposite end of the calyx in the estimated center of the calyx. In the *two-point* selection method the vector is computed directly from the two points selected. The unit vector of this vector defines the target kidney calyx orientation for the *two-point* method. The two points chosen centrally at the two ends of the calyx with the determined target kidney calyx orientation vector is depicted in Figure 5-5(a) and (b).

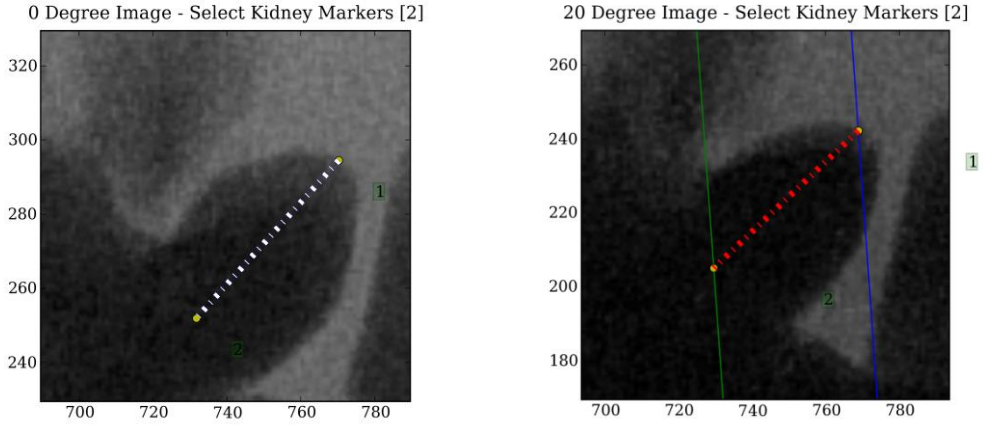

(a) 0° image (b) 20° image

Figure 5-5: Two-point selection method example

The use of the either the *four-or two* point method is dependent on whether a clear calyx structure can be identified. In cases where the structure edges are unclear, the *four-point* method is a safer choice as it reduces point selection error. In cases where a distinct edge can be identified, the *two-point* method provides good results. In both the *four*-and *two-point* selection methods the center coordinate of the obtained calyx vectors are computed. This coordinate is called the *calyx-center coordinate*. The reason for computing this coordinate is to supply information required for implementing an alternative needle insertion option. The two insertion routines will be discussed in 5.3.

Access Marker Determination

During a PCNL procedure, the surgeon marks the site of needle insertion. In this project, identification of the needle insertion site was required for implementation of a second insertion method. The difference between the first- and second insertion method will be clarified in section 5.3.

The *access marker*, or surgeon specified access point, is the most easily acquired of the needed targeting variables. It is defined in the stereo image pair by a single 1 mm diameter radiopaque marker placed on the patient at the surgeon-selected site. Determination of its 3D coordinate is done in the same manner as each of the *needle*-and *gantry markers*.

The implementation of the *access*, *gantry*, and *kidney marker* determination methods will be illustrated in section 6.5 and 6.6. The following section describes how the newly defined coordinates and vectors are used to compute the required targeting rotations and translations.

5.3 Targeting: Translation and Rotation Computation

Two insertion routines were developed utilizing the information gained in section 5.2. A representation of the targeting information and targeting routines

are shown in Figure 5-6 depicting a sectioned view of a patient in the prone position.

- *Insertion routine 1* uses the defined *calyx vector* (between yellow markers) and attempts to orientate the needle in this vector at a pre-specified distance from the calyx tip. This coordinate is called the *needle tip coordinate* (green marker). The *access marker* (blue marker) is not used in this routine. *Routine 1* resembles the "triangulation" technique described in section 2.3.3.6.
- *Insertion routine 2* uses the *access marker coordinate* (blue marker) and *calyx-center coordinate* (orange marker) to provide a new vector to which the needle is adjusted. In the case of *routine 2*, the *access marker* (blue marker) is also the *needle tip coordinate* (blue marker). *Routine 2* resembles the "keyhole" technique described in section 2.3.3.6.

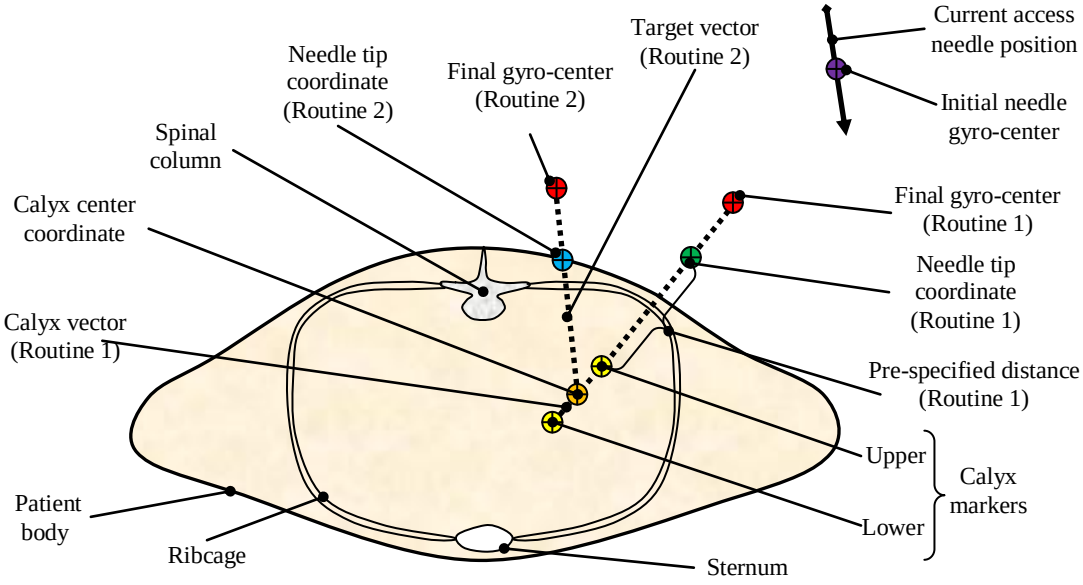

Figure 5-6: Targeting information and insertion routines

As the targeted *gyro-center coordinates* (red markers) for the two respective insertion routines are now known, the needed translation from the *initial gyro-center coordinate* (purple marker) to any of the targeted markers can be computed. The two insertion routines are similar in computation approach as will be discussed in the subsequent sections.

Translation Determination

The required translation in the gantry x-, y-, z-directions for the respective routines is the difference between the GCS-transformed coordinates of the *initial gyro-center* (purple marker) and *final gyro-centers* (red markers). This is shown mathematically by *equation 28*:

$$(x, y, z)^T_{adjust} = (x, y, z)^T_{target} - (x, y, z)^T_{initial} \quad (28)$$

Angular Adjustment Determination

The computation of the necessary needle orientation adjustment is similar to that of the translation computation. The *needle-vector* (NV), *calyx vector* (CV) and *calyx-center-to-access-point-vector* (CCAP) are transformed to the GCS system. Each vectors' respective angles with the XZ and YZ-plane in the GCS is determined. These angles, shown in Figure 5-7, are called θ and φ with respect to the YZ and XZ-planes respectively. In order to compute the required needle adjustment for *insertion routine 1*, the difference between the respective θ and φ angles of the NV and CV is determined. For *insertion routine 2*, the difference between the respective θ and φ angles of the NV and CCAP is determined. This is shown mathematically as:

Angle adjustment for Insertion Routine 1:

$$\begin{aligned} \theta_{adjust} &= \theta_{NV} - \theta_{CV} \\ \varphi_{adjust} &= \varphi_{NV} - \varphi_{CV} \end{aligned} \quad (29)$$

Angle adjustment for Insertion Routine 2:

$$\begin{aligned} \theta_{adjust} &= \theta_{NV} - \theta_{CCAP} \\ \varphi_{adjust} &= \varphi_{NV} - \varphi_{CCAP} \end{aligned} \quad (30)$$

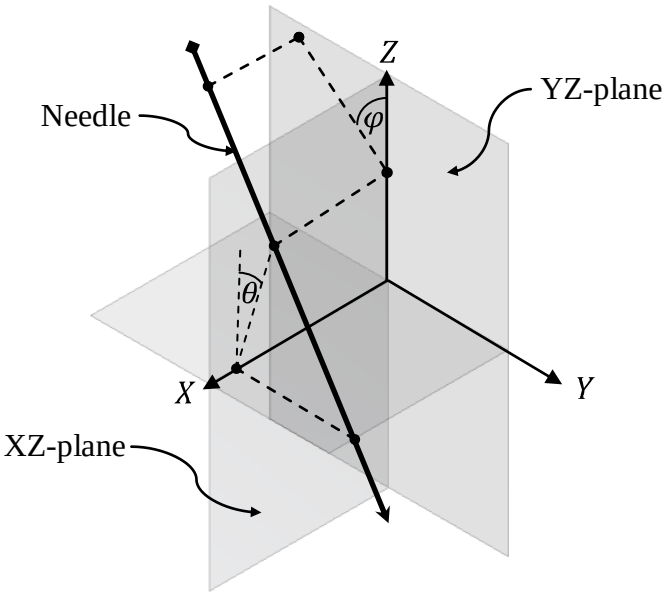

Figure 5-7: Rotation angles and planes

CHAPTER 6

6. VISION IMPLEMENTATION

The vision theory and targeting computation methods discussed in chapters 3 and 5 are implemented in two testing environments, called the *laboratory* and *surgery room* environments, respectively. The differences between and the need for testing the system in these environments will become evident in chapter 7. This chapter describes the sequence of outputs as observed by the operator when utilizing the graphical user interface (GUI) and shows the visual results of the implemented functions. It also briefly comments on alternative methods investigated in an attempt to improve point selection accuracy.

6.1 Testing Environments

6.1.1 Laboratory Environment

A procedure and environment was needed to simulate the final implementation environment of the designed system. A normal stereo vision setup was devised consisting of the following: (a) a stable camera mounting base with camera mounting positions at the same angular orientation as used by the fluoroscopy system (b) two digital cameras [Canon Powershot A620] mounted on the base at the proper positions (c) a LEGO calibration object with 35 recognizable corresponding points (d) two transparent targets with adjustable holders and (e) the needle-positioning system.

6.1.2 Surgery Room Environment

The surgery room, the final implementation environment of the designed system, consisted of the following: (a) surgery room bed used for fluoroscopy procedures (b) BV Pulsera fluoroscopy system [Phillips Medical] (c) the calibration object with radiopaque calibration markers (d) two target types and (e) the needle-positioning system.

6.2 Image Processing

The image processing techniques used to automatically identify the center of each navigation and calibration marker in the x-ray images were discussed in section 3.3. The results of the described image processing algorithms on a typical calibration object image taken by the C-arm in position 1 is shown in Figure 6-1(a) to (f) with the dots in Figure 6-1(f) representing the calculated centers. Only image averaging was implemented on the LEGO calibration object in the laboratory setup.

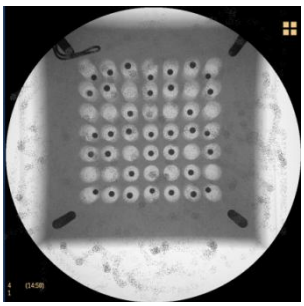

(a) Original image with noise

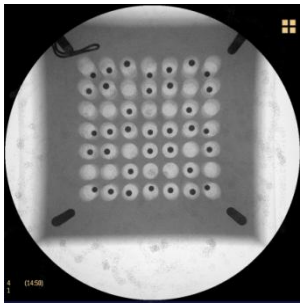

(b) Image averaging

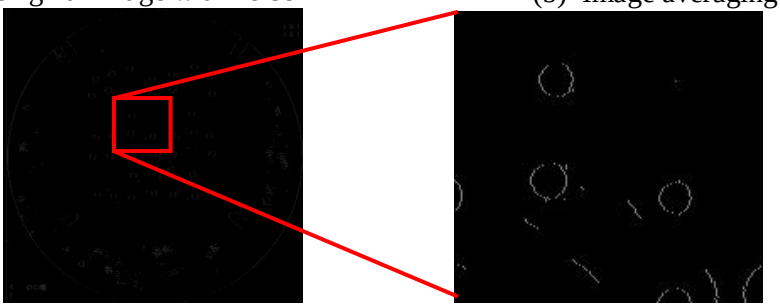

(c) Canny edge detection

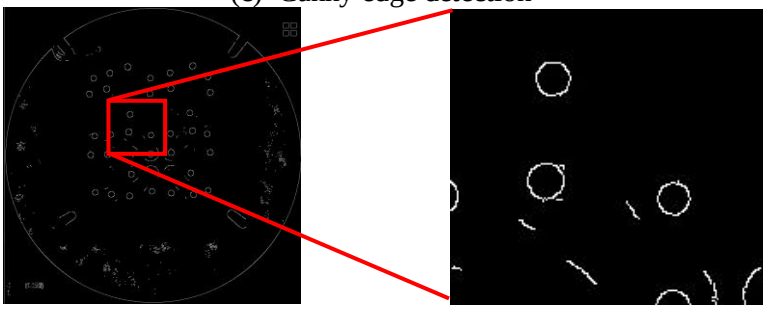

(d) Contour detection

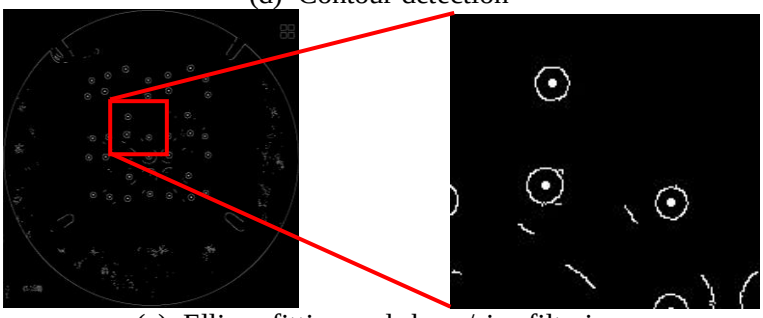

(e) Ellipse fitting and shape/size filtering

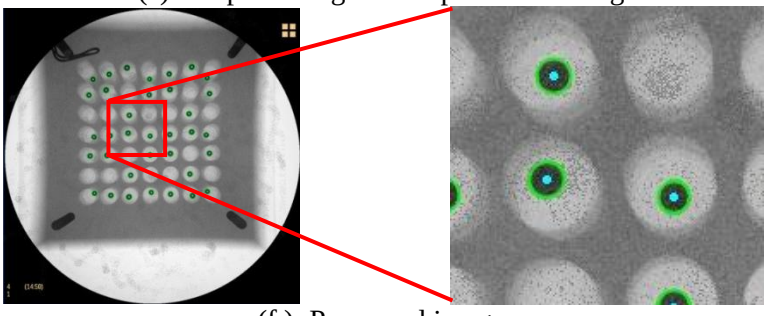

(f) Processed image

Figure 6-1: Image processing results

With the center of each calibration marker identified, 3D coordinate-assignment of each marker was possible after the completion of the automatic marker-sorting process. Marker sorting consisted of a sequence of steps implemented on the marker-center matrix of the image acquired in position 1 and position 2 respectively. The sorting algorithm follows these steps:

1. Find replicas in each center matrix by comparing the identified points' x- and y-pixel with the other points in the matrix.
2. Replace all replicas by 0's.
3. Remove all 0's from matrices.
4. Find points with a high probability of being replicas by comparing the variation in x and y-coordinates.
5. Replace all probable replicas by 0's.
6. Remove all 0's from matrices.
7. Confirm that 35 markers have been detected in image 1 and 2.
8. Sort the markers in seven sub-matrices (the seven rows of markers in the calibration object) according to their x-pixel values.
9. Sort each of the seven sub-matrices according to each y-pixel value.
10. Assign the known 3D coordinates to each 2D coordinate.

6.3 Distortion Correction, Calibration and Triangulation

With the image processing functions applied, the optimization of the calibration and distortion parameters were implemented. Triangulation was applied using all the needed parameters. The results of the implemented functions are shown below.

6.3.1 Calibration and Distortion Correction

The importance of distortion correction has been discussed in section 3.1.2. Calibration and distortion correction were performed simultaneously via optimization of the back-projection error. The main function, *GetCameraMatrix(),* to compute the camera matrix, uses the functions *MyCalcDistort()* and *DistFixMetRadii()*. These functions are responsible for calculating the distortion coefficients and rectifying the specified coordinates respectively. The written code for these functions can be viewed on the attached CD with many other functions not specifically described here. With the camera matrix and distortion correction parameters known, the 35 points used during calibration could be plotted with the corrected points in the same figure showing the correction of each point. This is illustrated in Figure 6-2(a)-(b) with (a) displaying the original and rectified points and (b) showing the shortest distance between each corresponding original and rectified point.

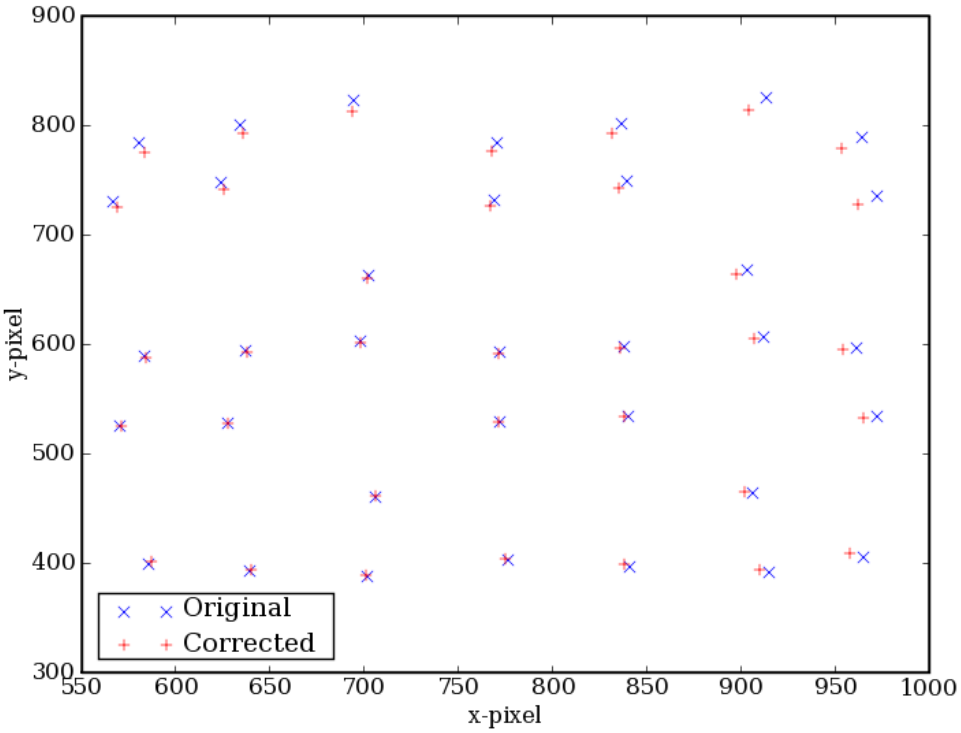

(a) Distorted versus undistorted marker positions

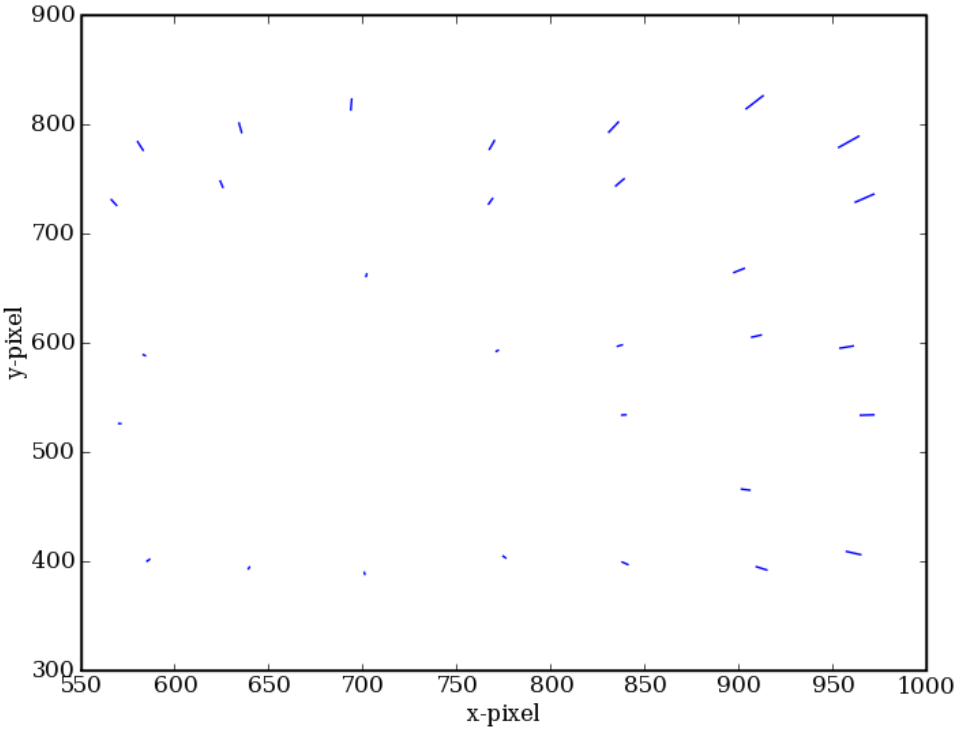

(b) Distances between distorted and undistorted positions

Figure 6-2: Undistorted and distorted marker positions and distances

By connecting the lines between the original distorted pixel coordinates and the pixel coordinates of the undistorted points as shown in Figure 6-2(b), radial distortion can easily be observed. The lines are short near the center of the image and increase as points approach the image extents. Correction distances of up to 15 pixels were observed.

6.3.2 Triangulation

With the camera projection matrices of the respective C-arm positions known, corresponding points in the stereo image pair could be reconstructed using the triangulation method described in section 3.2.3. A function of Singels [45], implementing this theory, was applied. The 35 triangulated markers of the calibration object are shown in Figure 6-3(a) illustrating the reconstruction of each marker. The reconstructed marker-configuration compares well with the actual marker-configuration shown in Figure 6-3(b).

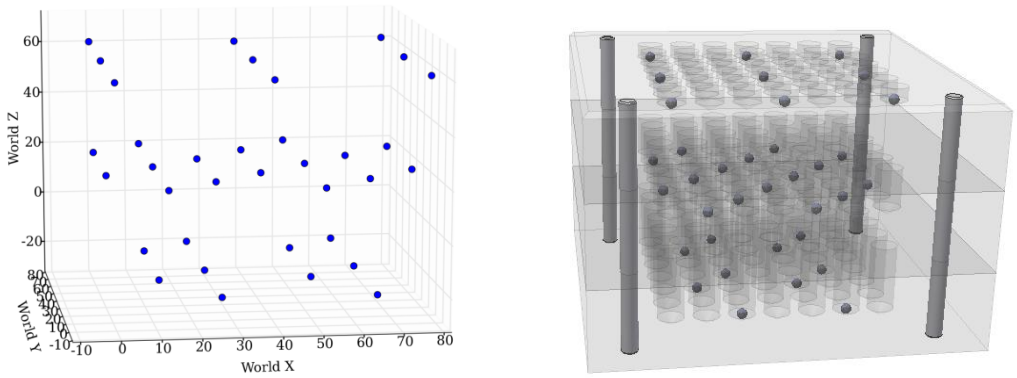

(a) Reconstructed marker-configuration (b) Actual marker-configuration

Figure 6-3: Calibration object triangulated markers

6.4 GUI Design and Operation

The control center of the described positioning system is the surgeon operated user interface. The written code for the GUI is included on the attached CD. This interface aids the surgeon in calibration of the imaging system and in defining the relative needle and kidney positions by requesting specific actions from the operator. With successful point selection the algorithms described in section 5 are implemented. The interface developed and the inputs required on each user screen will be discussed and implementation thereof will be shown in Section 6.5 and 6.6. The three main screens are the *calibration*, *point selection* and *targeting screen*.

Calibration Screen

The *calibration screen*, shown in Figure 6-4, has three sub-frames where user interaction is required. Actions on this screen results in the calibration of the image acquisition system. The two calibration images taken at each respective

position of the C-arm are specified in **1** and put through the averaging algorithm. The averaged images for the respective C-arm positions are selected and shown in **2**. With the calibration images selected, automatic calibration or manual calibration can be activated in **3**. The calibration process takes approximately 15 seconds to complete depending on the convergence of the distortion correction and calibration optimization function.

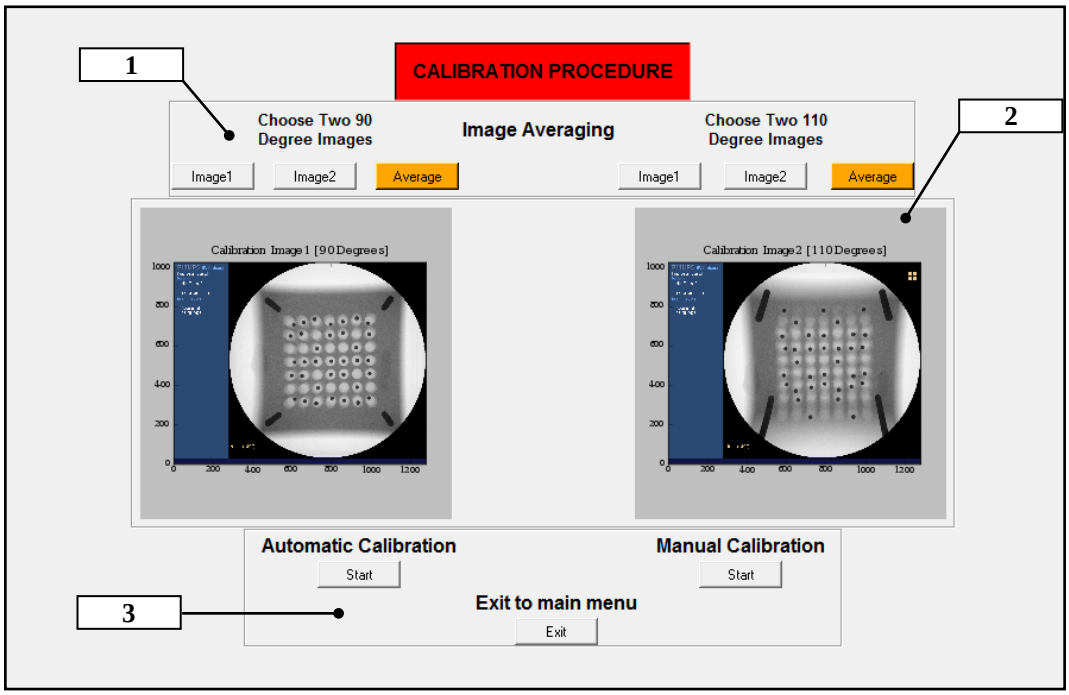

Figure 6-4: GUI calibration screen

Point Selection Screen

The *point selection screen*, shown in Figure 6-5, has four sub-frames. This screen allows the definition of all points required for targeting. The two targeting images taken at each respective position of the image acquisition system are specified in **1** after which the averaging algorithm is applied. The averaged images for the respective imaging positions are selected and shown in **2**. Sub-frame **3** is the main selection frame. Selection buttons for the *gantry*, *needle*, and *access* markers as well as the two *calyx marker* selection methods are contained in this frame. Also contained in this frame are the activation options for *automatic point selection*-and *epiline help*. These two options will be elaborated on in the next section. Sub-frame **4** allows the operator to progress to the *targeting screen* or to go back to the *calibration screen* for re-calibration. Once all needed points have been defined the *targeting screen* can be accessed.

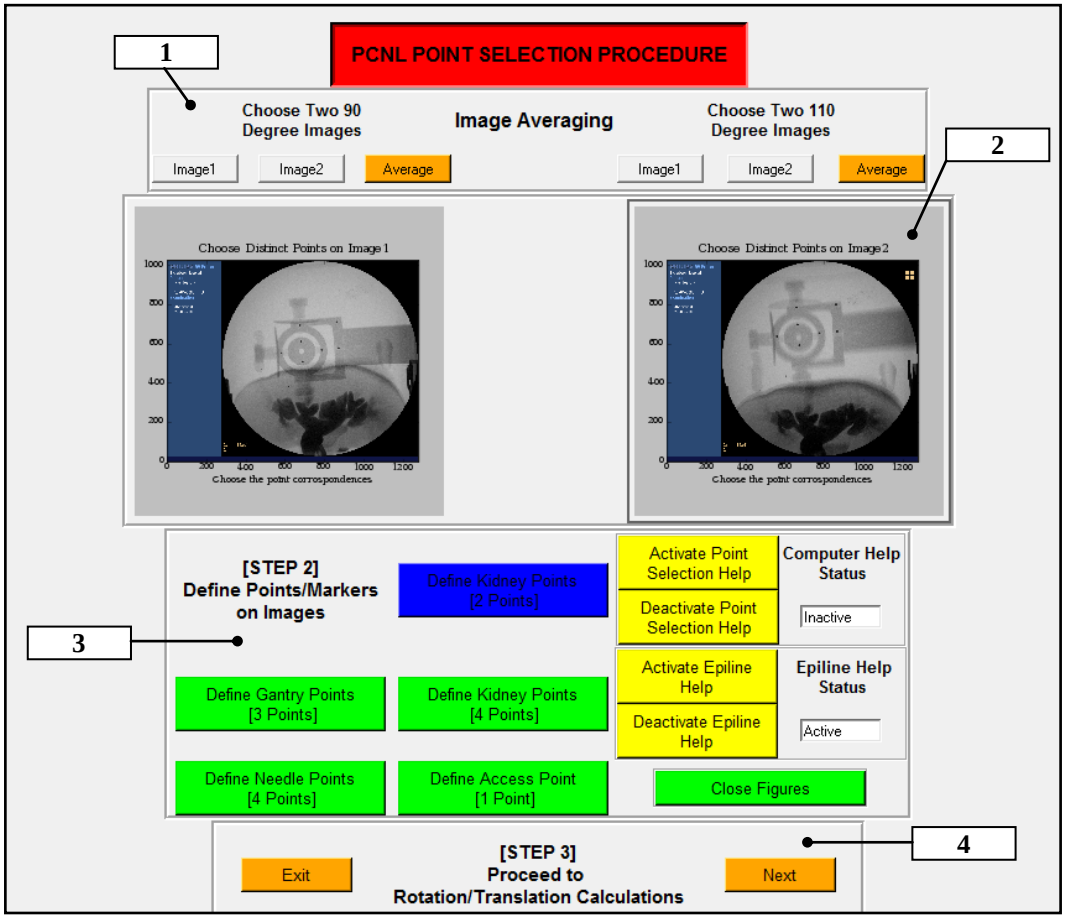

Figure 6-5: GUI point selection screen

Targeting Screen.

The *targeting screen*, shown in Figure 6-6, consists of six sub-frames and produces the final translation and rotation needed for targeting. As explained in section 5.3, two insertion routines were realized. Sub-frame **1** is associated with *insertion routine 1*. As explained, the distance between the top calyx point and skin surface is unknown in this procedure. An estimated distance is required and is defined by the surgeon in sub-frame **1** as 60 mm to 160 mm. This distance is then re-adjusted in sub-frame **4** if initial needle positioning for *insertion routine 1* was not close enough to the insertion site. In sub-frame **2**, the initial positions of the needle-positioning system is entered by the operator and the selection between the data, obtained by the *four* or *two-point* method described in section 5.2, is made. Sub-frame **3** and **5** supplies the final targeting positions and required needle depth of the positioning system for *insertion routine 1* and *insertion routine 2* respectively. Sub-frame **3** and **5** each has the option to show the calculated insertion path in a 3D figure and also displays messages aiding the surgeon. Sub-frame **6** is used to go back to the *point selection screen* if point redefinition is necessary. It is also used to exit from the program. The main steps of the targeting process are shown in process-map form in *Appendix C*.

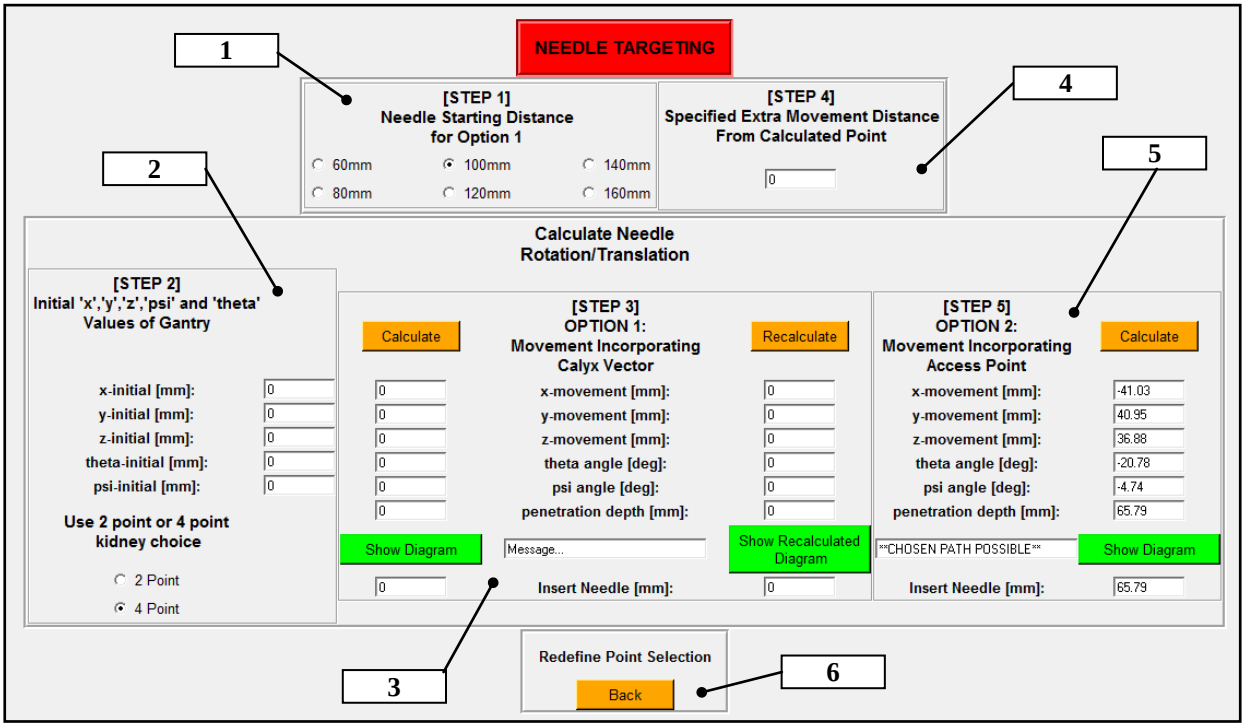

Figure 6-6: GUI targeting screen

6.5 Navigation Marker Detection and Selection

With distortion compensated for and calibration of the cameras completed, any corresponding points in a stereo image pair of an object obtained from the calibrated volume could be accurately reconstructed. Utilizing the epipolar geometry theory as explained in section 3.2.1, in conjunction with the discussed image processing techniques, selection of the navigation markers were realized. During this part of the procedure, three separate groups of navigation markers required selection. The three groups are the *gantry*, *needle* and *access markers*. The selection process of the *kidney markers* will be shown in the next section. The process of selecting a navigation marker for one corresponding point pair by using the GUI will be discussed and illustrated.

The developed GUI allows the operator to activate or deactivate the use of the "*epiline"* and *"automatic center detection" help*. The *automatic center detection help* has not been explicitly described, as it entails the same point identification techniques used during the automatic calibration process. When this function is active, an algorithm searches the two targeting images for spherical artifacts with sizes corresponding with the size of the navigation markers. When such markers are identified, their centers are determined in the same manner as that of the calibration marker centers, discussed in section 6.2, and saved to a dataset. When the operator selects the center of a navigation marker, the dataset is first checked for a coordinate that matches or closely matches the selected point. If such a point is found that is within the postulated accuracy requirements, that point replaces the point defined by the user. This applies to both of the target images. The output

of the *automatic center detection help* algorithm shown in Figure 6-7(a)-(b) is not displayed during the procedure, but merely shown for better understanding of the process. As seen in Figure 6-7(a) and Figure 6-7(b), all eight of the navigation marker centers (3 *gantry*, 4 *needle* and 1 *access marker*) are found in the two target images. The 1 mm diameter *access marker* can be seen at the bottom left of each enlarged image.

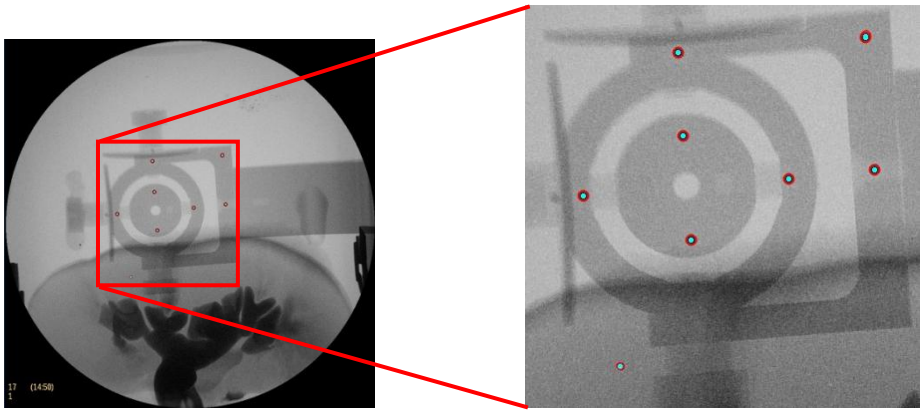

(a) 0° Target image with navigation markers

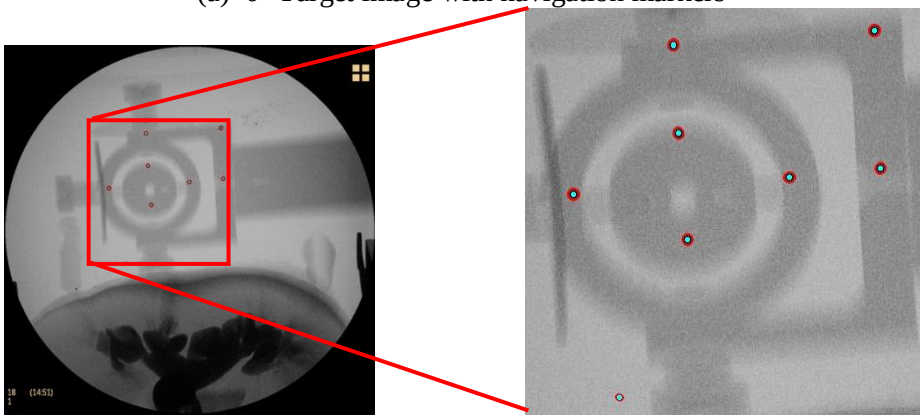

(b) 20° Target image with navigation markers

Figure 6-7: Automatic marker detection algorithm example

Three separate buttons allow the selection of a specific group of navigation markers. The shown example illustrates point selection of the *gantry markers* with *epiline help* activated and *automatic center detection help* deactivated. When the button for *gantry marker* selection is pressed, Figure 6-8(a)-(d) appears on the screen. The two original images with a zoomed window adjacent to each are shown in Figure 6-8(a)-(d). The current design still requires the surgeon to distinguish between the *needle*, *gantry* and *access marker* groups when selecting points. The configuration of the different groups are unmistakable with the *needle markers* in a diamond shape configuration and the *gantry markers* on its outside in the shape of a flipped capital "L". The *access marker* is half the size of the other navigation markers and is easily discerned.

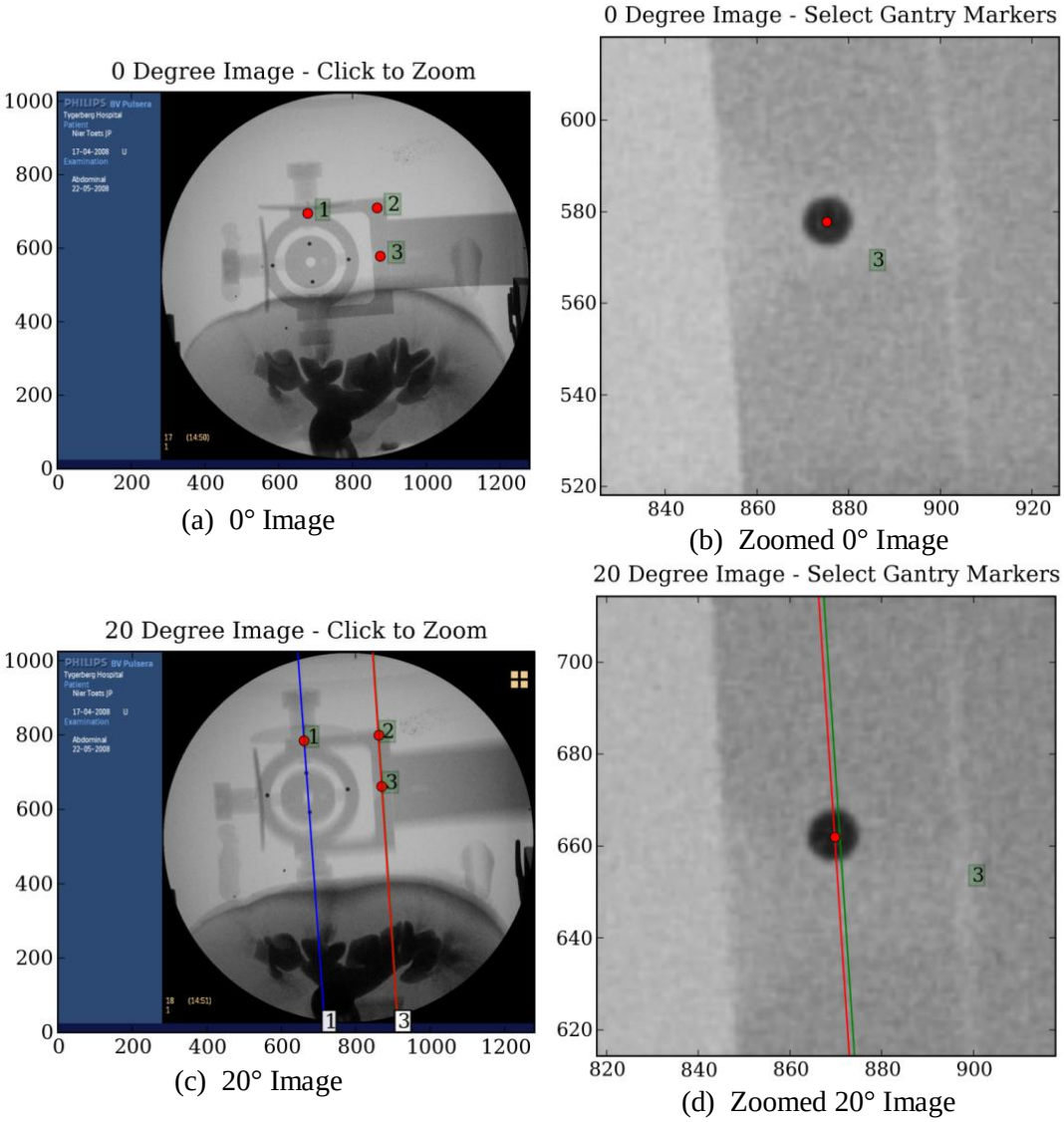

(a) 0° Image

(b) Zoomed 0° Image

(c) 20° Image

(d) Zoomed 20° Image

Figure 6-8: Navigation marker targeting sample

The identified *gantry markers* are selected on the original image *(a)* by clicking the mouse pointer in its vicinity. The adjacent zoom window *(b)* enlarges the selected part of the image, allowing the operator to better select the center of the marker. Once the marker center is selected, it is also re-plotted on the original image with the marker number for error-prevention purposes. With the selection of the point in the first stereo image, its corresponding epiline with its line number is depicted on the corresponding stereo image *(c)*, showing the line in which the point correspondence lies. The area on the line, obtaining the corresponding marker, is selected. The adjacent zoom window *(d)* enlarges this area, allowing accurate point selection. Once again the selected point is re-plotted on the original image with its marker number. With *epiline help* activated, the point selected by the operator in Figure 6-8(d) is forced onto the corresponding epiline by changing its x-pixel coordinate accordingly.

The described point selection process is applied in a similar manner in defining the *needle* and *access markers*.

6.6 Target Detection and Selection

Finding point correspondences of the kidney calyx in the stereo image pair is much more problematic than that of the navigation markers, as definite corresponding structures are not as easily discerned.

Two techniques, *shape from silhouette* and *kidney calyx modeling*, were investigated. In the case of *kidney calyx modeling*, the idea was to represent a specified calyx by a cylinder fitted through a calyx point cloud, by using the method of least-squares best-fit, as described by Forbes [49]. The point cloud had to be obtained by the arduous task of selecting a great number of points on the stereo pair of the structure. This technique showed promise on simulated data, but practical implementation in the fluoroscopic environment was impossible due to the variation of actual calyx structure to that of a cylinder and the fact that a large number of points were needed for a decent result. Describing the calyx as a spherical structure was also attempted, but showed similar results. Figure 6-9 depicts the vector (dashed line) of the cylinder fitted through a point cloud of 40 "dummy" points.

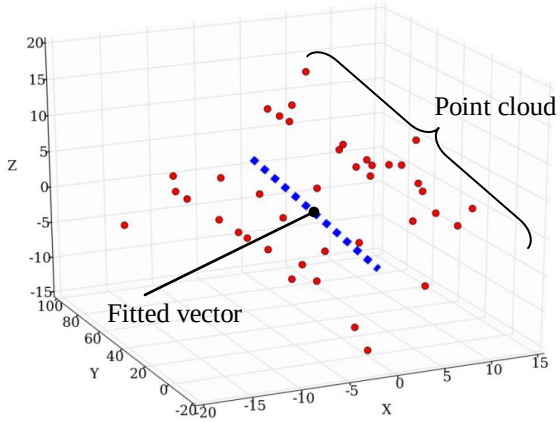

Figure 6-9: Cylinder fitting through point cloud example

The *shape from silhouette* technique uses a number of images of an object taken from various positions and reconstructs the object using only the outline of the particular object [50]. This technique was not suited for our application, as it requires a large number of control points and noiseless images from different positions to function properly. As radiation exposure minimization was one of the critical outcomes of the project, an increase in image acquisition for targeting purposes was not a viable option. Another problematic requirement of this technique is a good generic 3D model [50]. Due to the great variation in kidney structure between patients, obtaining a generic model is difficult, if not impossible.

The two methods ultimately used to select the *kidney markers* were discussed in section 5.3. Implementation of the *four-point* method is shown in Figure 6-10(a)-(d) with the dashed lines in (b) and (d) showing the projected needle vector for the respective camera orientations. The red dots define the selected points.

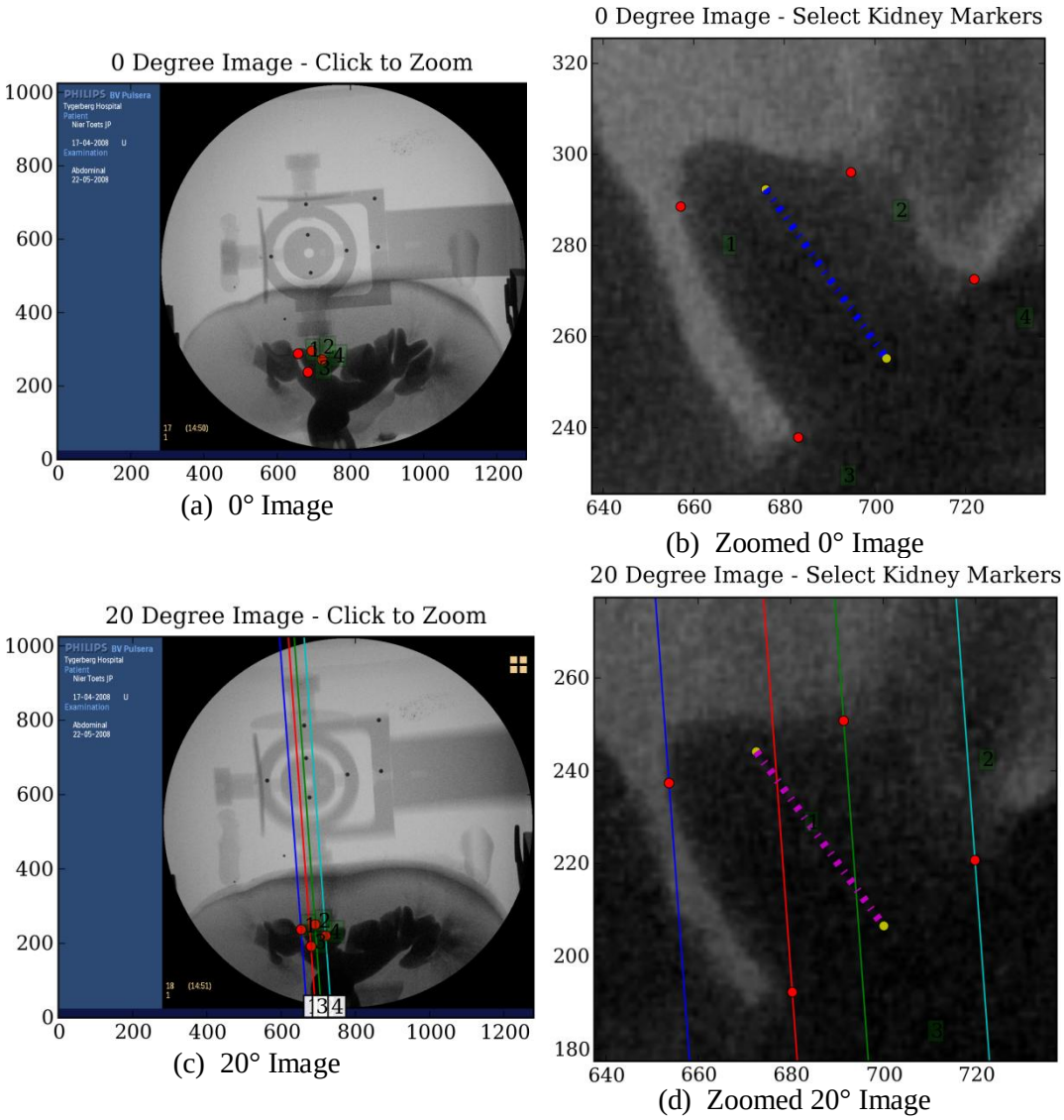

(a) 0° Image

(b) Zoomed 0° Image

(c) 20° Image

(d) Zoomed 20° Image

Figure 6-10: Kidney targeting sample

By using the *four-point* selection method, the error, as well as the probability of the selected point falling outside the structure, was reduced. The *two-point* selection method was added for use in situations where kidney structure did not give a clear shape or calyx edges were too blurry. The functionality of these techniques was verified through testing.

CHAPTER 7

7. TESTING AND RESULTS

This chapter describes the testing procedures and discusses the results obtained. The system was tested in the environments discussed in section 6.1 with each providing different information regarding the functioning of the system. The *laboratory* testing procedure provided quantitative results regarding calibration accuracy, mechanical system repeatability, and targeting accuracy, whereas *surgery room* testing provided results on calibration accuracy and system functionality. A diagram illustrating the procedural steps followed during a *surgery room* experiment is shown in Figure 7-1.

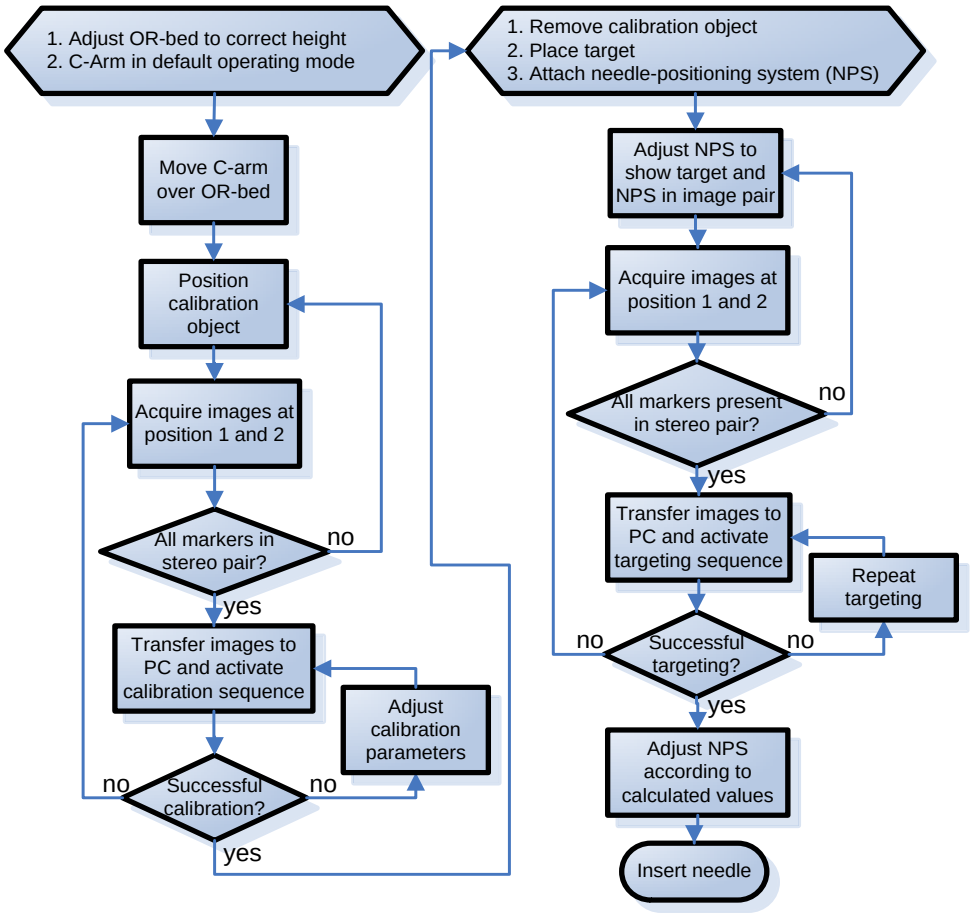

Figure 7-1: Surgery room process-map

The *laboratory* testing procedure is similar except for the imaging system and calibration object used. This will become clear in the subsequent discussion.

7.1 Laboratory Testing

Due to the time constraints on the fluoroscopic imaging system for which the positioning system was designed, a simulation of the final implementation environment was necessary. To simulate the C-arm fluoroscopy system, two digital cameras were mounted in a configuration resembling that of the C-arm. This allowed thorough testing of the system to determine mechanical design accuracy and repeatability, as tests could be repeated in a controlled environment. This setup also allowed a basis for algorithm testing during the development of the system.

7.1.1 Setup and Procedure

The needle-positioning system, described in section 4.5, was attached to the base of the digital camera support structure. This support structure was designed to position the two digital cameras at the same relative orientation as that of the two C-arm positions. The setup is shown in Figure 7-2. The main steps of the testing procedure included system calibration, implementation of the targeting algorithm, needle alignment, and needle and insertion.

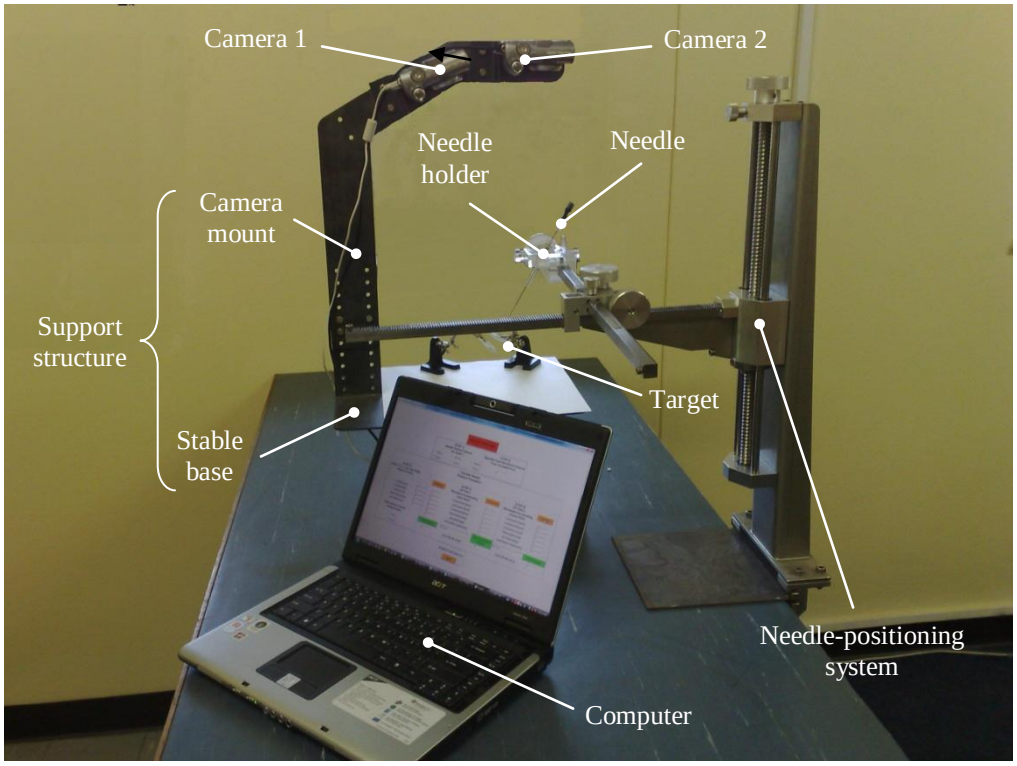

Figure 7-2: Laboratory setup

7.1.1.1 Calibration

A LEGO calibration object, shown in Figure 7-3, was used for its simple construction and high accuracy. 35 points on the object were identified as markers which served as calibration points. Care was taken during the construction of the object to prevent occlusion of markers in the 0° and 20° images.

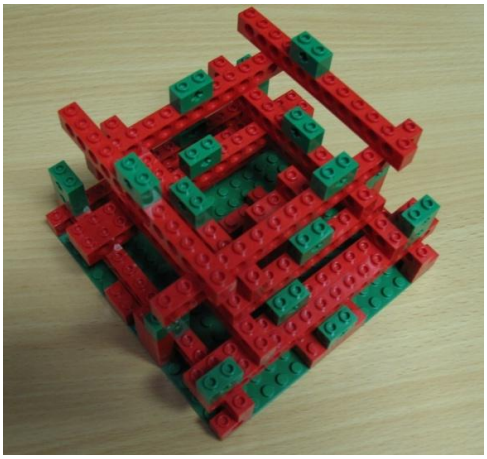

Figure 7-3: LEGO calibration object

Using *PSRemote version 1.5.1* from *Breeze Systems*, images of the placed LEGO calibration object were captured and stored. Care was taken to ensure that adjustable parameters of the two respective cameras, such as digital zoom, was kept unchanged from calibration to targeting. The calibration algorithm described in section 3.1.3 was implemented, supplying the needed parameters for point reconstruction. Selection of the 35 markers was performed manually.

7.1.1.2 Targeting

Successful targeting is dependant on corresponding markers being identifiable in the stereo image pair. Visibility of the needle and target markers in the 0° and 20° images were thus paramount. In contrast to x-ray images, normal digital camera images are unable to show features of an object when occluded by an opaque object. To solve this problem, the target was constructed from two thin transparent discs with printed 1, 2, 4, 6, 10 and 20 mm diameter concentric circles. Marks on the 10 mm diameter circles served as targeting points for the *four-point* method described in section 5.3. With this setup, targeting points could be identified regardless of target orientation. Light diffraction errors caused by the transparent material were assumed to be zero due to its negligible thickness. The two target discs, 30 mm apart, are shown in Figure 7-4(a).

With the target placed in view of the cameras, the needle-positioning system, without the needle holder, was translated and locked in a position where all navigation markers and target points were visible in the respective images. Figure 7-4(b) illustrates this for camera position 1. Using the acquired images in position 1 and position 2, the targeting procedure as described in chapter 6 was implemented, yielding the required needle translations and rotations.

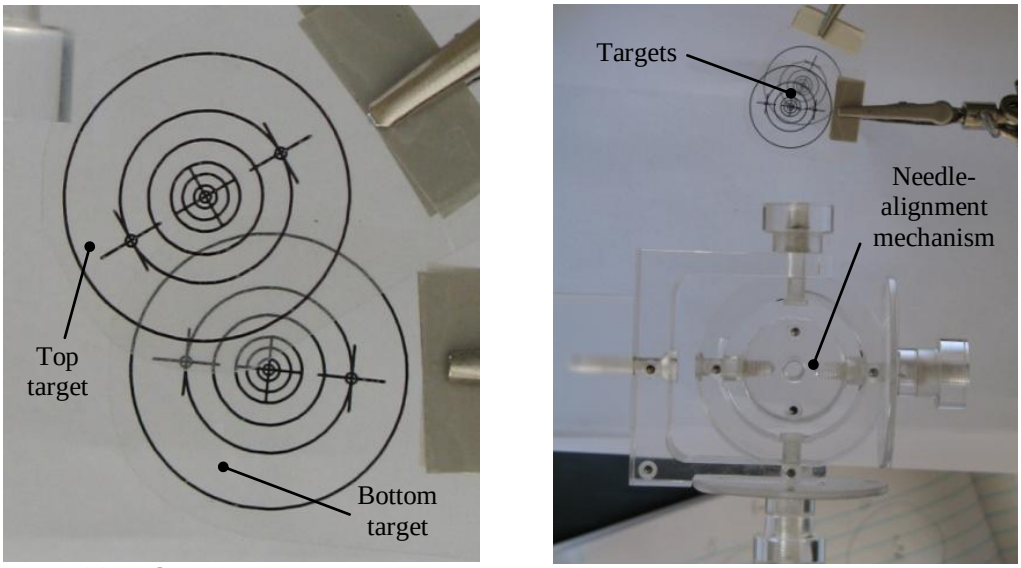

(a) Laboratory setup target (b) Targeting image of position 1

Figure 7-4: Laboratory setup targets

7.1.1.3 Needle Alignment and Insertion

With the required translations and rotations computed, needle positioning could be performed. The needle holder, with the needle inserted up to the tip of the guide, was introduced into its position on the needle positioning device. The adjustment sequence of the relative x, y translation and θ, φ rotation was irrelevant. It was however advantageous to adjust the z-translation as the final step to prevent scraping of the insertion surface during horizontal translation adjustment. With the system adjusted and locked to the specified positions, the needle was advanced through the needle guide to a pre-ticked position on the needle, specifying final needle depth. The targeting location on the top and bottom transparent targets were recorded and used in compilation of the results that follow.

7.1.2 Results

7.1.2.1 Calibration Accuracy

Calibration accuracy was estimated by comparing points on the calibration object, with known coordinates, and not used during the calibration procedure, with its triangulated results. The distance between the known and reconstructed marker coordinates subsequently gave the total estimated error caused by point selection and calibration.

Three calibration sets were tested. In each calibration set eight different points were identified and targeted. This process was repeated three times for each test set, totaling 72 targeted points. The statistical error between the known coordinates and reconstructed coordinates are shown in Table 7-1. From the three calibration sets an average bias error, determined by dividing the sum of the error

by the number of points, of just over 0.5 mm was obtained, showing fair calibration and point selection accuracy. The larger errors observed in the third calibration set was ascribed to faulty coordinate assignment of a calibration point.

Table 7-1: Calibration accuracy analysis for laboratory setup

PARAMETERS	CALIBRATION SET 1 [mm]	CALIBRATION SET 2 [mm]	CALIBRATION SET 3 [mm]
Bias Error	0.4	0.4	0.5
Standard Deviation	0.2	0.2	0.4
Range	0.7	0.6	1.3
Minimum	0.1	0.1	0.2
Maximum	0.8	0.7	1.5
Point Count	24	24	24

7.1.2.2 Mechanical Repeatability

Mechanical repeatability (i.e. adjusting the needle position with the needle-positioning system) was investigated by means of repeated targeting tests on a stationary, unchanged target. The translation and rotation steps as described were performed on 12 different targets and repeated three times per target, supplying the error produced by the combination of the angular and translational positioning. The variation in angular adjustment could also be calculated as the distance between the two transparent targets were fixed and the target points' x and y coordinates was known. Determination of the θ-angle is illustrated in Figure 7-5. The φ-angle is found in the same manner.

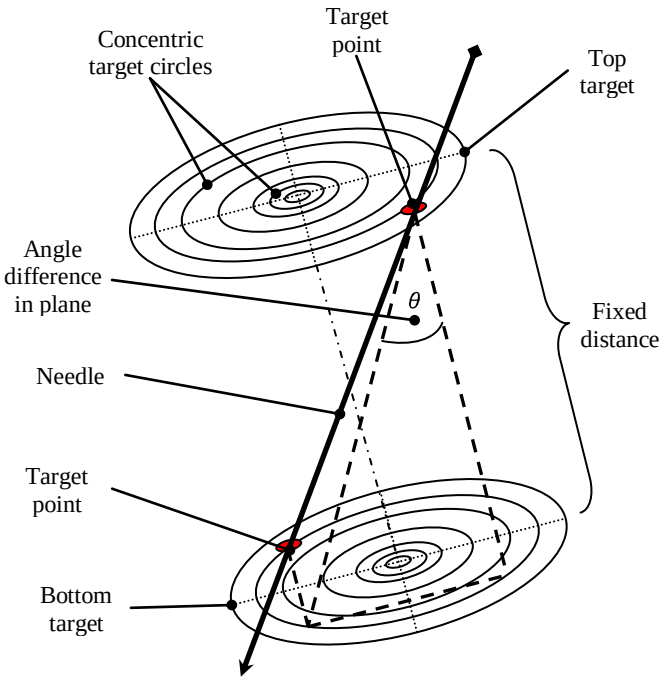

Figure 7-5: Needle angle diagram

From the 36 targeted points the alignment error could be computed. The alignment error in the θ and φ rotation directions are shown in Figure 7-6(a)-(b) and the repeatability in Table 7-2.

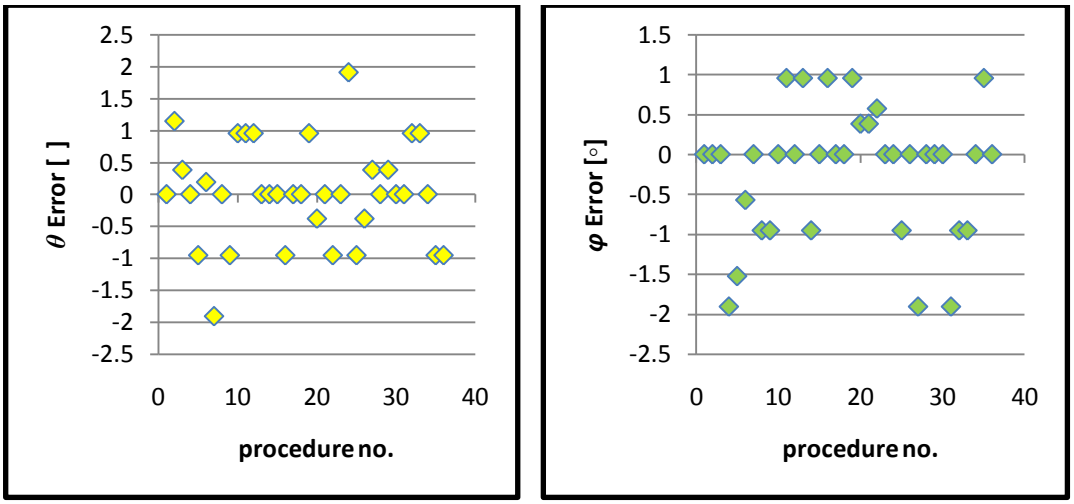

(a) θ difference (b) φ difference

Figure 7-6: Alignment accuracy data

Table 7-2: Laboratory system angular repeatability

PARAMETERS	θ (◦)	φ (◦)
Bias Error	0.0	-0.2
Standard Deviation	0.8	0.8
Range	3.8	2.9
Minimum	-1.9	-1.9
Maximum	1.9	1.0
Point Count	36	36

The range of the alignment error in the θ rotation was 3.8°, with a lower and upper limit of -1.9° and 1.9° respectively. The range of the alignment error in the φ rotation was 2.9°, with a lower and upper limit of about -1.9° and 1° respectively. The repeatability error ranged from a minimum of 0 mm to 2.5 mm with an average of 0.4 mm. The mechanical repeatability of the system was deemed acceptable for a first prototype as the functionality of the system as a whole was satisfactory.

7.1.2.3 System Accuracy

System accuracy was calculated by computing the error (i.e. the distance from the top and bottom transparency center to the target point) for each targeting procedure. Another 36 targeting routines were completed in order to obtain a sufficient sample size. Illustrated in Figure 7-7(a)-(b) are the targeting results for

the top and bottom transparency target respectively, shown in a dartboard configuration with the bull's eye (0,0) defining zero error.

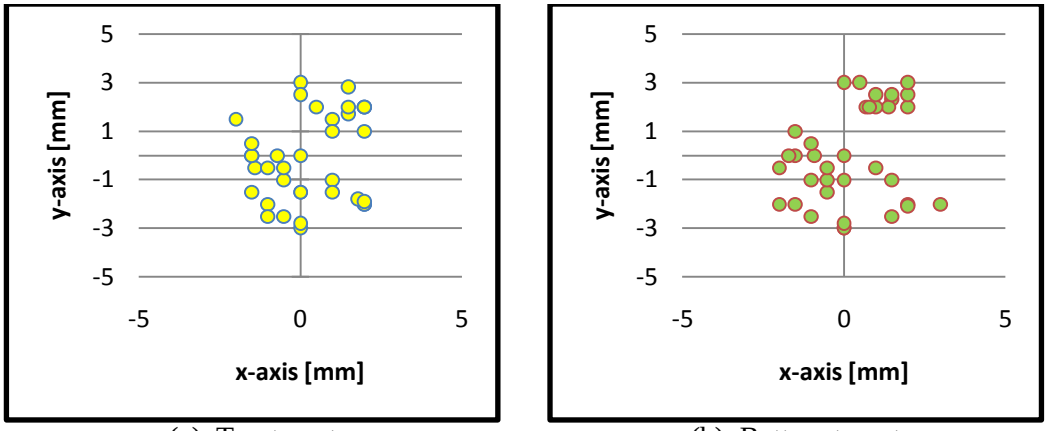

(a) Top target (b) Bottom target

Figure 7-7: Targeting accuracy data

It is clear from Figure 7-7(a)-(b) that variation is present. An average bias error of 2.1 mm with a standard deviation of 0.8 mm was obtained. The error ranged from 0 to 3.2 mm as shown in Table 7-3.

Table 7-3: Laboratory system accuracy test results

PARAMETERS	[mm]
Bias Error	2.1
Standard Deviation	0.8
Range	3.2
Minimum	0
Maximum	3.2
Point Count	36

7.1.2.4 Result Summary

An average bias calibration error of just over 0.5 mm was obtained showing good calibration and point selection accuracy. The alignment error of the needle had a range of approximately 3° in the θ and φ rotation direction respectively. This was acceptable as the whole needle was still inside the target volume. An average bias repeatability error of 0.4 mm and targeting error of 2.1 mm was acceptable for the application as the average diameter of a calyx was defined as 10 mm.

7.2 Surgery Room Testing

Testing in the *surgery room* environment was performed on two target types: (a) a target configuration similar to the one used in the *laboratory* testing procedure and (b) a porcine kidney injected with contrast medium. In contrast to

the *laboratory* testing which provided quantitative data, the *surgery room* testing consisted of "go-no-go" tests, providing only an indication to whether needle insertion was successful or not. The *surgery room* setup is shown in Figure 7-8.

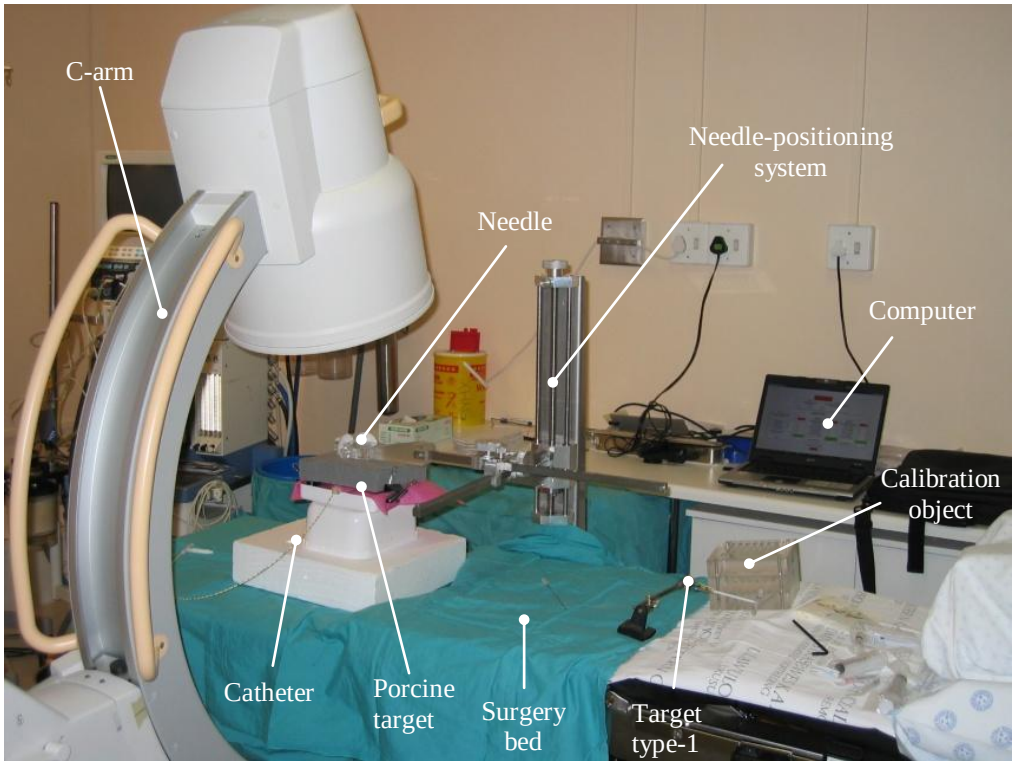

Figure 7-8: Surgery room testing setup

7.2.1 Setup and Procedure

The first target type, from now called *target type-1*, consisted of a radiolucent tube, 5 or 10 mm in diameter and 30 mm in length, with two 1 mm diameter metal spheres attached on opposite sides of each tube end. A simple clamping mechanism kept the target in position. See Figure 7-9(a). This target setup provided a good estimate of the accuracy of the system in the fluoroscopic imaging environment as the target size was known. *Target type-1* also provided a means of repeated testing of the system in the *surgery room* environment.

The second target, from now called *target type-2*, consisted of a foam-occluded contrast-filled porcine kidney, confined in a bag, and fixed in a container by means of fixing clamps. This is shown in Figure 7-9(b). The function of the foam-covering was to simulate the tissue of the back and to prevent biased needle adjustment during testing. A balloon type urethral catheter was inserted through which contrast medium could be introduced. The contrast reservoir was placed at a height creating pressure to dilate the internal structure of the kidney. This procedure corresponds closely to the normal surgery protocol used during a PCNL procedure. The two target types with their main parts are shown in Figure 7-9(a) and Figure 7-9(b).

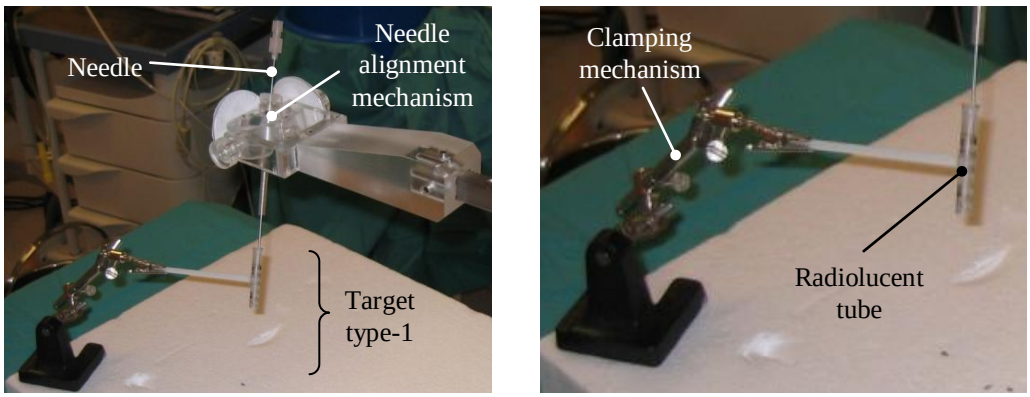

(a) Target type-1

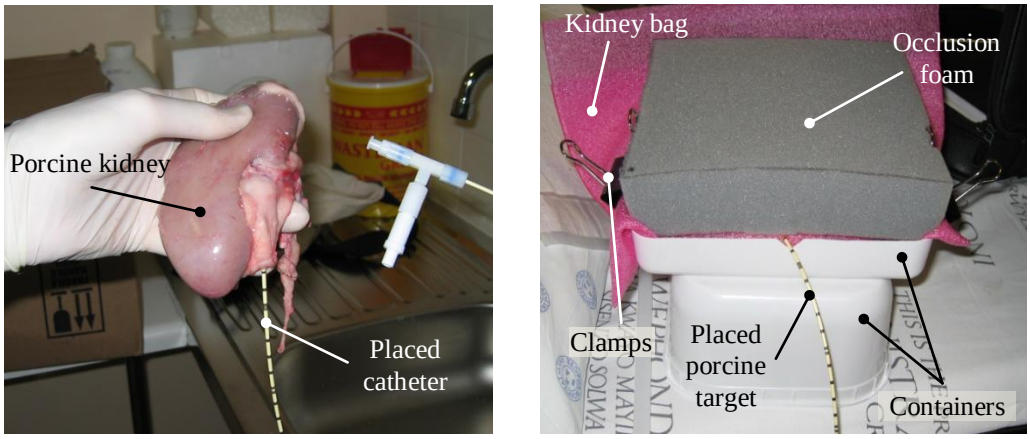

(b) Target type-2

Figure 7-9: Target types

In contrast to the laboratory setup, where the digital images were transferred directly to the computer, images acquired in the surgery room had to be transferred from the C-arm to the computer via USB-drive as direct access to the system's hard drive was not possible from the computer. Apart from the imaging system and target differences, the same procedure used during the laboratory setup was followed. Similar to the laboratory procedure the main steps were calibration, implementation of the targeting algorithm, needle alignment, and needle insertion.

7.2.1.1 Calibration

The C-arm was set to its default operating mode and moved approximately orthogonal to the bed. The II was positioned above the bed in position 1 to provide a greater imaging area. The bed was adjusted to a height allowing C-arm rotational movement between the two image acquisition positions without bed interference. With the C-arm in position, the calibration object was placed on the bed in the imaging line of the C-arm at the predetermined height of the target. Indicators on the calibration object, indicating the C-arm, surgeon, top and bottom side, showed correct object orientation. Test images were acquired to ascertain that all the markers showed in both the imaging positions. In order to prevent

errors and simplify the assignment of the known coordinates to the calibration markers by the automatic point recognition algorithm, the calibration object was rotated so the markers were presented as vertical dotted lines. Alternatively, this could be achieved by digital means using the "Image Rotate"-function on the C-arm interface. This is illustrated in Figure 7-10(a)-(b) by the yellow line fitted through one of the seven columns.

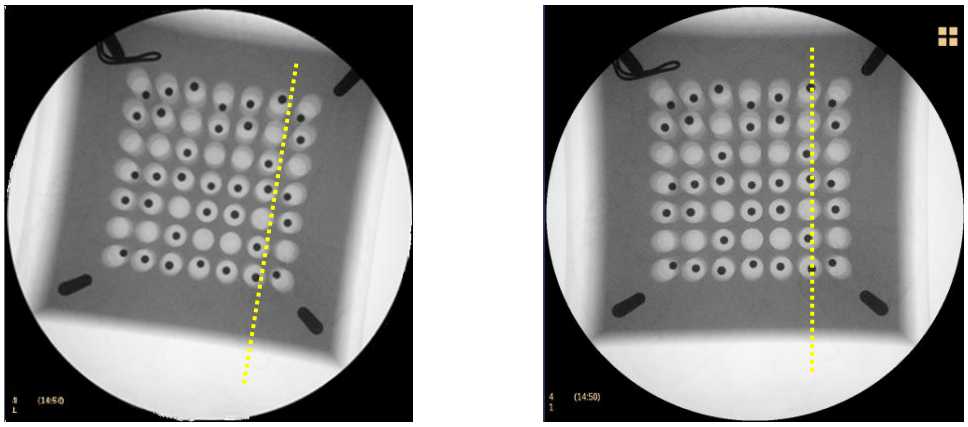

(a) Un-rotated image (b) Rotated image

Figure 7-10: Calibration image rotation

With the calibration object correctly placed and the C-arm able to rotate to position 1 and 2 unimpeded, calibration images were acquired and transferred to the computer where the calibration algorithm, described in earlier chapters, was implemented. This yielded the needed camera projection matrices as well as the distortion correction coefficients needed in the targeting procedure. The calibration process took approximately five to ten minutes to complete.

7.2.1.2 Targeting

The C-arm was moved away from the bed. *Target type-1* was placed on the bed at a random orientation. The C-arm was positioned so the target could be seen in the acquired images at position 1 and 2. The needle-positioning system was attached to the railings of the bed after which the horizontal axes of the system were adjusted so the needle holder could be seen in the same images as the target. The vertical axis was adjusted to move the needle holder as close to the target as possible, reducing the difficulty of getting the target and needle holder in the same image. With both the needle holder and the target in the same images taken at position 1 and 2, the images were transferred to the computer where the targeting algorithm was implemented. The same procedure was performed for *target type-2*.

7.2.1.3 Needle Alignment and Insertion

Needle alignment was performed as described in section 7.1.1.3. In contrast to the *laboratory* setup, where targeting accuracy could be empirically described, the setup used in the *surgery room* supplied only a "success" or "failure" result, where "failure" was defined as failure to access *target type-1* or *target type-2* and

"success" as a successful *target type-1* or *target type-2* penetration. With *target type-2* penetration, success could be validated by aspirating contrast fluid through the needle from the punctured collecting system whereas *target type-1* permitted visible confirmation. Shown in Figure 7-11(a) and Figure 7-11(b) respectively are the insertion of the needle holding device and device with inserted needle.

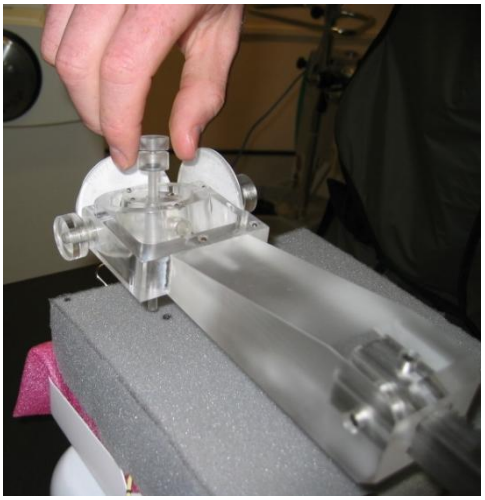

(a) Insertion of needle holder

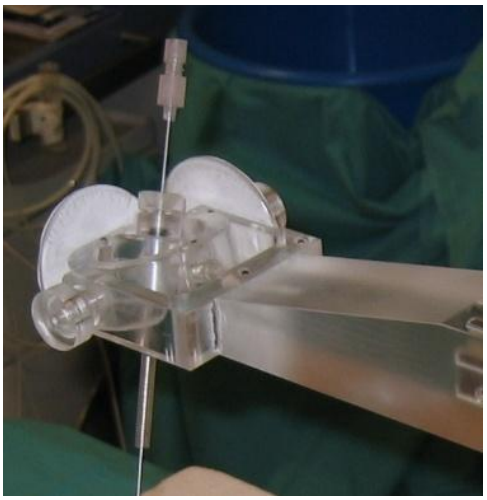

(b) Needle holder with inserted needle

Figure 7-11: Needle insertion

7.2.2 Results

7.2.2.1 Calibration Accuracy

Similar to the *laboratory* environment, calibration accuracy was estimated by reconstructing known coordinates of the calibration object not used during the calibration procedure and comparing the reconstructed with the known coordinates. The distance between the known and reconstructed marker coordinates gave the total estimated error caused by point selection and calibration.

Three calibration sets were tested with only three different markers identified and targeted per set. This left 32 markers available for calibration. The reason for selecting only three markers was the decrease in calibration accuracy as calibration points decreased. This process was repeated three times for each test set, totaling 27 targeted points. The statistical error between the known coordinates and reconstructed coordinates are shown in Table 7-4.

.

Table 7-4: Surgery room calibration accuracy results

PARAMETERS	CALIBRATION SET 1	CALIBRATION SET 2	CALIBRATION SET 3
Bias Error	0.3	0.2	0.3
Standard Deviation	0.1	0.1	0.2
Range	0.3	0.2	0.4
Minimum	0.2	0.2	0.0
Maximum	0.5	0.3	0.5
Point Count	9	9	9

An average bias error of less than 0.4 mm was achieved for the three tests. As expected, it was an improvement on the *laboratory* testing results due to the automatic calibration process implemented.

7.2.2.2 System Performance

Target Type-1

The relative positions of the reconstructed points to the calibrated volume are vitally important for accurate targeting. The calibrated volume is defined as the volume between the II and XRT occupied by the calibration object during calibration. Due to the large distortion in the x-ray images, reconstruction of points too far outside the calibrated volume resulted in large targeting errors. This was verified by targeting points outside the calibrated volume in some instances. 14 tests were completed using the 10 mm diameter *target type-1*. Targeting done within 50 mm above and 50 mm below the calibrated volume i.e. in the range -50 to 130 mm as the calibrated volume is 80 mm high, resulted in a 100% targeting success rate. One failed and no successful needle insertion attempts were completed in the range below -50 mm whereas the range above 130 mm resulted in one success and five failures. These results are summarized in Table 7-5.

Table 7-5: Surgery room performance

Coordinate Height Range					
Height < -50		**-50 < Height < 130**		**Height > 130**	
Success	**Failure**	**Success**	**Failure**	**Success**	**Failure**
0	1	7	0	1	5
0% Success rate		100% Success rate		17% Success rate	

Seven tests with the 5 mm diameter *target type-1* as target were done with the same success/failure rate. The dependency on the calibration volume emphasizes the importance of calibrating the C-arm for a specified region. It was concluded that targeting more than 50 mm below or above the calibrated volume would result in a high probability of targeting failure. The targeting procedure took approximately ten minutes to complete for each of the respective *target type-1* targets.

Target Type-2

Only two *target type-2* procedures were performed due to the restricted availability of the fluoroscopy system. Successful needle insertion was achieved in both cases i.e. a 100% success rate. As stated, successful needle insertion into the specified calyx was validated by aspiration of contrast fluid through the needle. This can be seen in Figure 7-12. Further validation was done by taking an extra image in position 1 and another from a position lateral to the surgery bed. The respective images, confirming successful needle insertion, are shown in Figure 7-13(a) and Figure 7-13(b). The targeting procedure for each of the respective *target type-2* targets took approximately 15 minutes to complete excluding the calibration process.

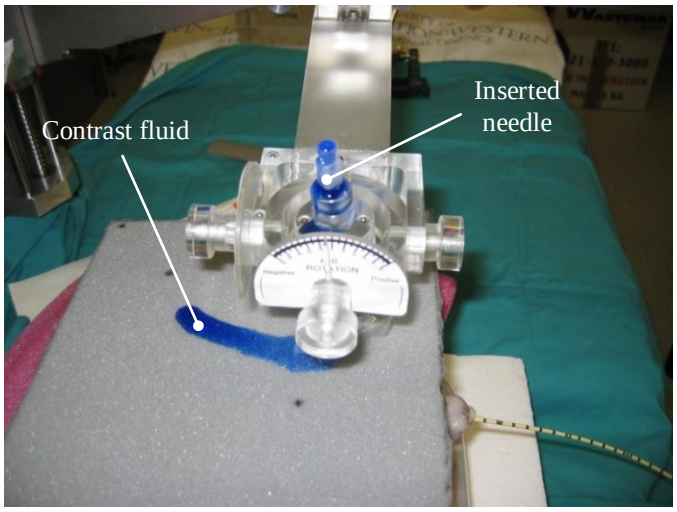

Figure 7-12: Aspiration of contrast fluid with successful needle insertion

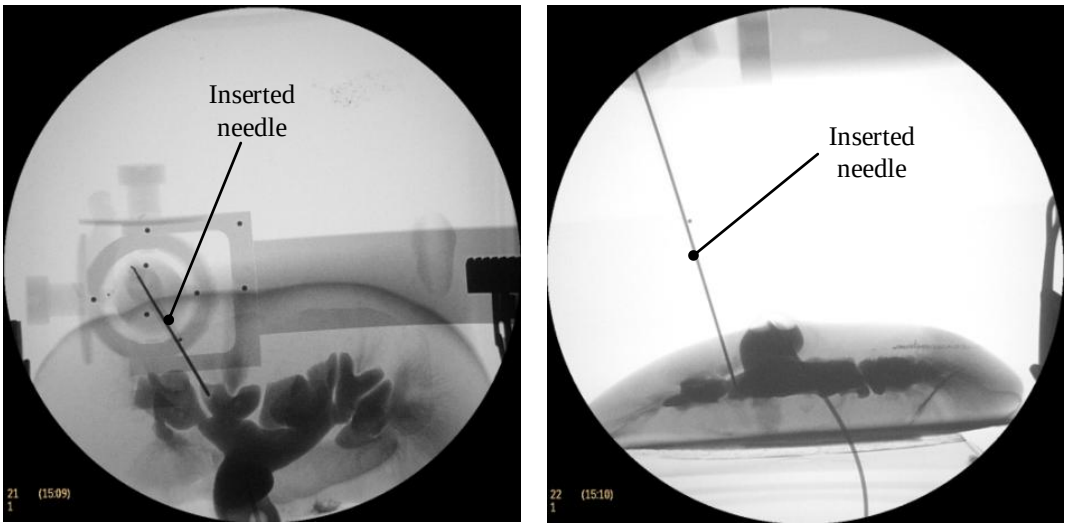

(a) Insertion verification image 1 (b) Insertion verification image 2

Figure 7-13: Insertion verification images

7.3 Error Propagation

A number of error sources exist in the designed system. These error sources include errors originating from C-arm adjustment, calibration, point selection and repeatability of the positioning system. The effect of implementing the targeting procedure outside the calibrated volume has been discussed. Despite the fact that the effect of each individual error source is impossible to describe quantitatively, a description of the possible error sources is deemed necessary for future work.

C-Arm Movement

In a normal stereo vision setup, two fixed cameras are used, implying that their relative orientation stays unchanged during the process of calibration and further image capturing. To use the C-arm as a stereo vision setup and obtain images from two camera positions, rotation of the C-arm arc was required. These orientations were readjusted as accurately as possible before each calibration or targeting image were acquired, but the propagation of errors was inevitable as the C-arm was never designed for precision rotational and translational movements.

Calibration Error

An average bias calibration error of less than 0.4 mm was attained. Even though this error is given as a quantitative result, it is dependent on the accuracy of the marker center detection algorithm, distortion correction and calibration algorithm. Calibration errors will inevitably have an effect on targeting accuracy.

User Marker and Target Selection Error

The errors incurred due to calibration and C-arm movement directly influence the accuracy of marker targeting. In the project, simplifying aids and error minimization techniques were implemented with the aim of reducing targeting errors. Despite these efforts, point selections ultimately depended (to a lesser extent) on operator skill. Targeting of the kidney calyx was the greatest challenge as corresponding points were hard to identify. The assumption that the error in point reconstruction, when choosing the intersection of the contrast and epilines, resulted in an error small enough for accurate targeting was supported by two successful porcine kidney tests. A larger sample will have to be tested for a proper validation.

Calibration Volume Selection

The decrease in targeting accuracy outside the calibration volume has been described in preceding sections. Working inside the calibration volume is crucial in avoiding large targeting errors. This implies that the height of the target volume must be identified in the pre-surgery planning stage and taken into account during the calibration and targeting stage of the procedure.

Positioning System Error

Insecure attachment of the needle-positioning system to the surgery room bed can be the cause of errors. Unexpected needle movement during the calibration and targeting procedure due to an unstable positioning system was avoided by securing the clamps to the protrusions of the bed. The mechanical repeatability with a mean of 0.4 mm in translation and less than 1° for rotation was acceptable for the first prototype. These errors were the result of a lack of resolution of the measurement apparatus. Despite the mechanical precautions implemented in the design of the needle-positioning system to restrict deflection of the axes, errors caused by deflecting axes are thought to be another source of errors.

CHAPTER 8

8. CONCLUSIONS AND RECOMMENDATIONS

8.1 Thesis Goal and Outcome

The goal of this thesis was the development of an affordable fluoroscopy guided needle-positioning system for use in PCNL procedures. Such a system would aid the surgeon in gaining kidney access quickly and effectively, reducing surgery time, surgery cost and patient-surgeon radiation exposure. Current kidney access techniques implemented in general practice rely only on surgeon experience for needle guidance and often result in sub-optimum placement of the needle inside the kidney, increased hemorrhage due to multiple unsuccessful needle punctures and in some cases, termination of the surgery due to reduced visibility and risk to the patient.

In this project, it was set out to develop an easily implementable positioning system utilizing stereo vision theory on images acquired by a fluoroscopy system. This system would be beneficial to surgeons and patients alike. The system developed obtained the specified accuracies and achieved the defined requirements.

8.2 Challenges, Future Improvements and Recommendations

Implementation of the designed system poses some challenges. One is the system's accuracy dependency on the calibrated volume between the II and XRT. As explained in the preceding chapters, this volume is restricted by the size of the fluoroscopy system's imaging area and calibration object size. A limited calibration volume makes it problematic to navigate the positioning device relative to the target while maintaining visibility of all navigation markers and needed target structures in the stereo image pair. This limitation was easily overcome in the experimental procedures as the target position could be adjusted at will. In the surgery room environment with a patient on the surgery bed, the same effect would be achieved by moving the C-arm base relative to the patient. An important factor to keep in mind while moving the C-arm would be the change in calibrated volume height if the C-arm height is adjusted.

The identification of corresponding navigation markers is not problematic as the implemented algorithms use anticipated marker shapes and configuration for identification. The identification of corresponding points on target calyces, on the other hand, still leaves room for improvement as the surgeon is still required to rely on his/her experience to choose a corresponding kidney point. The mechanisms implemented in aiding the surgeon in these choices showed promise

in the porcine kidney tests. Further research into methods of automatic point identification in stereo pairs would significantly increase accuracy and system confidence.

A number of possible design improvements were identified for future prototypes. These improvements include changes to the calibration object, needle-positioning system as well as the user interface. The calibration object used in this project was originally designed for a different model fluoroscopy system; the BV Libra, also from Philips Medical. The BV Libra system is equipped with a smaller imaging area, which resulted in the manufacture of a smaller calibration object than can be accommodated on the BV Pulsera system. Another recommended improvement entails the change of the calibration object marker-configuration. The marker-configuration used in the current object can be rearranged in future to accommodate a larger number of markers at more than three depth levels. With these improvements, calibration and targeting accuracy will improve, as a larger image area is calibrated.

A number of improvements to the current mechanical needle-positioning system are possible. One would be the replacement of the manual adjustment by an automated alternative such as the use of servo-or stepper motors. This would increase system accuracy and procedure speed, but would significantly increase system cost. If manual adjustment is retained in future prototypes, a digital LCD screen, linked to position sensors or encoders displaying axes position and needle angle, is recommended. This would increase procedure speed, accuracy and prevent user error, but would also introduce electronic components to the design.

In the current design, the needle guide extends downwards from the alignment body towards the patient. By extending the guide away from the patient, the active distance between the patient and *gyro-center* would be reduced during insertion, reducing the chances of needle deflection. With this configuration, the process of obtaining the navigation markers and target in a stereo pair will also be simplified as the needle positioner would be able to get closer to the patients skin during imaging. An improved needle depth monitoring and insertion technique is recommended in future prototypes. The method used in this project, although cumbrous in nature, is capable of positioning a needle to a depth accuracy of 0.5 to 1 mm. The automatic technique used in the PAKY system, which makes use of two rotational discs that clamp the needle by means of friction, is a concept that can be adapted for this application [35].

Recommended changes to the current user interface include improved visual aid to the operator by means of stepwise diagrammatical illustrations and fewer GUI interactions. Current procedure time can be improved considerably if direct access from the computer to the images on the fluoroscopy system can be attained. This is a crucial factor for implementation of the system and needs to be looked into.

8.3 Conclusion

The system developed in this thesis made use of a standard C-arm fluoroscopic imaging system used in a stereo vision configuration to supply the needed

navigation images. A calibration and targeting sequence operated from a PC-installed interface provided the surgeon with the needed alignment and translation information for calyx targeting. As only a stereo image pair was required for the targeting procedure, just a fraction of the radiation dose emitted during a normal PCNL was discharged during a targeting procedure. The needle-positioning system was adjusted according to the calculated values and the needle inserted to the specified depth. An average targeting accuracy of less than 2.5 mm was attained during mock-up target tests. This compares favourably with the systems described in chapter 2, despite utilizing different means of targeting and alignment. 0.5 mm, 1.5 mm, 1 to 2 mm and 3 mm accuracies were reported by Bzostek, Potamianos, Rovetta and Vaird with their respective systems [30, 28, 32, 37].

Implementation of the developed system on a porcine kidney showed promising results, achieving successful insertion in both cases. Bzostek *et al.* also implemented ex-vivo tests on porcine kidneys with a success rate of 83% [30]. This was done on a much larger sample size than the sample size used in this thesis. The average access-procedure time of 15 minutes compares favourably with access times of current manual techniques that can range between 10 and 40 minutes. Feedback by the collaborating urologist, who performed the access on the porcine kidneys, was very positive. Recommendations concerning the use of the GUI and simplification of certain elements of the procedure will be included in future prototypes. The manufacturing cost of the complete system, estimated at R35 000, is a fraction of the cost of similar systems. As the software application was developed in Python, a freeware programming platform, no additional licensing or software was purchased.

Despite various possible improvements and the identified implementation challenges of the current system, the results obtained warrants further refinement with the ultimate goal of testing the system on human subjects.

REFERENCES

[1] Kidney Stones - Guide to removing your Kidney stones, [S.a.] [Online] Available: http://www.cidpusa.org/kidney%20stones.html. [2007, September 18].

[2] Stametelou, K.K., Francis, M.E., Jones, C.A., Nyberg, L.M. & Curhan, G.C. 2003. Time Trends in Reported Prevalence of Kidney Stones in the United States: 1976–1994. Kidney International, 63:1817–1823.

[3] Kidney Health - Kidney and Urology Foundation of America, [S.a.] [Online]. Available: http://www.kidneyurology.org/Library/. [2007, September 20].

[4] LeRoy, C. Percutaneous Nephrolithotomy [Online] Available: http://www.surgeryencyclopedia.com/forum.html. [2008, February 12].

[5] Riches, E. 1968. The History of Lithotomy and Lithotrity. Annals of the Royal College of Surgeons of England, 43(4):185-199.

[6] Martini, F.H. & Bartholomew, E.F. 2003. Essentials of Anatomy and Physiology. 3rd Edition. Prentice Hall.

[7] Skolarikosa, A., Alivizatosa, G., De la Rosette J. 2005. Percutaneous Nephrolithotomy and its Legacy. European Urology, 47:22–28.

[8] Paik, M.L., & Resnick, M.I. 2000. Is There a Role for Open Stone Surgery?. Urologic Clinics of North America, 27:323-331.

[9] Buchanan, J. Kidney Stone Disease/Simptoms. [Online] Available: http://www.cornellurology.com/stones/symptoms/. [2008, February 12]

[10] Matlaga, B.R., Kim, S.C. & Lingeman, J.E. 2004. Improving Outcomes of Percutaneous Nephrolithotomy: Access. Elsevier.

[11] Wikipedia.com-Lithotripsy. [S.a.] [Online] Available: http://en.wikipedia.org/wiki/ESWL/html. [2008, May 28]

[12] Goodwin, W.E., Casey, W.C. & Woolf, W. 1955. Percutaneous Trocar (Needle) Nephrostomy in Hydronephrosis. JAMA, 157:891- 894.

[13] Fernstrom, I. & Johannson, B. 1976. Percutaneous Pyelolithotomy: A New Extraction Technique. Scandanavian Journal of Urology and Nephrolithotomy: 10 : 257.

[14] Miller, N.L., Matlaga, B.R. & Lingeman, J.E. 2007. Techniques for Fluoroscopic Percutaneous Renal Access. The Journal of Urology, 178:15-23.

[15] Ng, M.T., Sun, W.H., Cheng, C.W. & Chan, E.S.Y. 2004. Supine Position is Safe and Effective for Percutaneous Nephrolithotomy. Journal of Endourology, 18:469–478.

[16] Matlaga, B.R., Shah, O.D., Zagoria, R.J., Dyer, R.B., Streem, S.B. & Assimos, D.G. 2003. Computerized Tomography Guided Access for Percutaneous Nephrostolithotomy. Journal of Urology, 170:45-47.

[17] Marcovich, R. & Smith, A.D. 2005. Percutaneous Renal Access: Tips and Tricks. British Journal of Urology.

[18] Park, S. & Pearle, M.S. 2006. Imaging for Percutaneous Renal Access and Management of Renal Calculi. Elsevier Saunders - Urology Clinics of North America, 33:353–364.

[19] Fuchs, E.F. & Lashey, D.B. 1998. Urologist-Acquired Renal Access for Percutaneous Renal Surgery. Elsevier Science Inc, 51:927–931.

[20] El-Assmy, A.M., Shokeir, A.A., Mohsen, T., El-Tabey, N., El-Nahas, A.R., Shoma, A.M., Eraky, I., EL-Kenawy, M.R. & EL-Kappany, H.A. 2007. Renal Access by Urologist or Radiologist for Percutaneous Nephrolithotomy—Is it Still an Issue? Journal of Urology, 178:916-920.

[21] Watterson, J.D., Soon, S. & Jana, K. 2006. Access Related Problems During PCNL - Urologist or Radiologist. Journal of Urology, 176:142-145.

[22] Ramakumar, S. & Segura, J.W. 2000. Renal Calculi: Percutaneous Management. Urology Clinics of North America, 27:617 - 622.

[23] Lingeman, J.E., Matlaga, B.R. & Evan, A.P. 2007. Surgical Management of Upper Urinary Tract Calculi in Kavoussi, L.R., Novick, A.C. & Wein, A.J. Campbell-Walsh Urology. 9th Edition. Vol. 2, 44:1485 -1500.

[24] Muslumanoglu, A.Y., Tefekli, A., Karadag, M.A., Tok, A., Sari, E. & Berberoglu, Y. 2006. Impact of Percutaneous Access Point Number and Location on Complication and Success Rates on Percutaneous Nephrolithotomy. Urology International, 77:340–346.

[25] Zarrabi, A. 2007. Personal Interview. 18 August. Tygerberg Hospital, Cape Town.

[26] Su, L., Stoianovici, D., Jarret, T.W., Patriciu, A., Roberts, W.W., Cadeddu J.A., Ramakamur, S., Solomon, S.B. & Kavoussi, L.R. 2002. Robotic Percutaneous Access to the Kidney: Comparison with Standard Manual Access. Journal of Endourology, 16:471-475.

[27] Stoianovici D., Kavoussi L. & Webster R. 2002. Robotic Tools for Minimally Invasive Robotic Surgery. Complications of Urologic Laparoscopic Surgery: Recognition Management and Prevention.

[28] Potamianos, P., Davies, B.L. & Hibberd, R.D. 1994. Intra-Operative Image Guidance for Key-Hole Surgery: Methodology and Calibration. International Symposium on Medical Robotics and Computer Assisted Surgery.

[29] Cadeddu, J.A., Stoianovici, D. & Kavoussi, L.R. 1998. Robotic Surgery in Urology. Urology Clinics of North America, 25:75-85.

[30] Bzostek, A., Schreiner, S., Barnes, A.C., Cadeddu, J.A., Roberts, W.W., Anderson, J.H., Taylor, R.H. & Kavoussi, L.R. 1997. An Automated System for Precise Percutaneous Access of the Renal Collecting System. Submitted to The First Joint Conference of CVRMed and MRCAS, Grenoble. France.

[31] Cadeddu, J.A., Bzostek, A., Schreiner, S., Barnes, A.C., Roberts W.W., Anderson, J.H., Taylor, R.H. & Kavoussi, L.R. 1997. A Robotic System for Percutaneous Renal Access. American Urological Association, 158:1589-1593.

[32] Rovetta A., Sala R. & Wen, Z. 1995. Robotics and Tele-robotics Applied to a Prostate Biopsy on a Human Patient.

[33] Stoianovici, D., Cadeddu, J.A., Demaree, R.D., Basile, S.A., Taylor, R.H., Whitcomb, L.L., Sharpe, W.N. & Kavoussi, L.R. An Efficient Needle Injection Technique and Radiological Guidance Method for Percutaneous Procedures. 295-298.

[34] Radeka, E. 2005. Percutaneous Nephrostomies - Planning for an optimal access, Complications, Follow-up and Outcome. Uppsala: Uppsala University, PhD Thesis.

[35] Cadeddu, J.A., Stoianovici, D., Chen, R.N., Moore, R.G. & Kavoussi L.R. 1998. Stereotactic Mechanical Percutaneous Renal Access. Journal of Endourology, 12:121-125.

[36] Hanumara, N.C., Walsh, C.J., Slocum, A.H., Gupta, R. & Shepard, J. 2007. Human Factors Design for Intuitive Operation of a Low-Cost, Image-Guided, Tele-Robotic Biopsy Assistant. Proceedings of the 29th Annual International Conference of the IEEE EMBS, ThP2D4.7: 1257-1260.

[37] Viard, R., Betroun, N., Rousseau, J., Mordon, S., Ernst, O. & Maouche, S. 2007. Needle Positioning in Interventional MRI Procedure: Real Time Optical Localisation and Accordance with the Roadmap. Proceedings of the 29th Annual International Conference of the IEEE EMBS, FrB09.3: 2748-2751.

[38] Bascle, B., Navab, N., Loser, M., Geiger, G. & Taylor, R. 2000. Needle Placement Under X-ray Fluoroscopy Using Perspective Invariants. IEEE

[39] Geiger, B. & Navab, N. 2001. Apparatus and Method for Automatically Positioning a Biopsy Needle. Patent: 6,249,713 US.

[40] Heilbrun, M.P., McDonald, P., Wiker, J.C., Koehler, S. & Peters, W. 2000. Apparatus and Method for Photogrammetric Surgical Localization. Patent: 6,165,181 US.

[41] Regn, J. 2000. Device for Making a Guide Path for an Instrument on a Patient. Patent: 6,041,249 US.

[42] Hartley, R. & Zisserman, A. 2003. Multiple View Geometry in Computer Vision. 2nd Edition. United Kingdom, Cambridge: Cambridge University Press.

[43] Ma, Y., Soatto, S., Košecká, J. & Shankar Shastry, S., 2004. An Invitation to 3-D Vision: From Images to Geometric Models. New York: Springer-Verlag Inc.

[44] Van der Merwe, W.J. 2008. Rapid 3D Measurement Using Digital Video Cameras. Stellenbosch: University of Stellenbosch, MSc Thesis.

[45] Singels, W. 2007. An Application of Photogrammetry in the Petrochemical Industry. Stellenbosch : Stellenbosch University, MSc Thesis.

[46] Xu, G. & Zhang, Z. 1996. Epipolar Geometry in Stereo, Motion and Object Recognition: A Unified Approach. Springer.

[47] Mitschke, M. 2002. X-ray Calibration Dummy, A Method for Non-marker Based Registration for Use in Navigation-Guided Operations... Patent: 2002,004,1655, United States of America.

[48] Navab, N. 2000. C-arm Calibration Method for 3D Reconstruction. Patent: 6049582. United States of America.

[49] Forbes, A. 1991. Least-Squares Best-Fit Geometric Elements. National Physical Laboratory.

[50] Menudet, J.F., Becker, J.M., Fournel, T. & Mennessier, C. 2007, Model-Based Shape from Silhouette – A Solution Involving a Small Number of Views. VISAPP, International Conference on Computer Vision Theory and Applications, 379-386.

APPENDICES

Appendix A – Singular Value Decomposition (SVD)

The Singular Value Decomposition (SVD) is a widely used technique to decompose a matrix into several component matrices exposing many of the useful properties of the original matrix. Singels [45] explains the SVD as follows:

A problem frequently encountered is that of solving a set of equations of the form $A\boldsymbol{x} = \boldsymbol{0}$. In this project we encounter an over-determined system with noise where there are more equations than unknowns and no exact solution. From the equation it is seen that a non-zero solution for $\boldsymbol{x}$ is sought. Suppose $\boldsymbol{x}$ is a solution to the set of equations. Then $k\boldsymbol{x}$, for any scalar k, is also a solution. The solution can therefore only be determined up to a scale. In order to find this scale a constraint needs to be put on the system. A reasonable constraint commonly used would be the norm of the vector, $\|\boldsymbol{x}\| = 1$. The new problem can now be stated as finding the $\boldsymbol{x}$ that minimizes $\|Ax\|$ subject to $\|\boldsymbol{x}\| = 1$.

The SVD works as follows: let $A = UDV^T$, where U and V^T are orthogonal matrices and D is a diagonal matrix with the singular values in decreasing order on its diagonal. $\|UDV^T x\|$ needs to be minimized. Because U is orthogonal $\|UDV^T\boldsymbol{x}\| = \|DV^T\boldsymbol{x}\|$ and $\|\boldsymbol{x}\| = \|V^T\boldsymbol{x}\|$ because V^T is orthogonal. $V^T\boldsymbol{x}$ can be written as $V^T\boldsymbol{x} = \boldsymbol{y}$. The problem now changes to minimizing $\|D\boldsymbol{y}\|$ subject to $\|\boldsymbol{y}\| = 1$. The solution is thus $\boldsymbol{y} = (0, \ \ldots, \ 1)^T$. $\boldsymbol{y}$ needs to have a non-zero entry in the last position. $\boldsymbol{x} = V\boldsymbol{y}$ is thus simply the last column of V. To summarize: the sought solution $\boldsymbol{x}$ is the last column of V, where $A = UDV^T$ is the SVD of A.

Appendix B – Needle-Positioning System Assembly Drawings

Appendix C – GUI Process-Map